LA-13074-MS

C.3

CIC-14 REPORT COLLECTION
REPRODUCTION
COPY

Damage Detection Algorithms Applied to Experimental and Numerical Modal Data from the I-40 Bridge

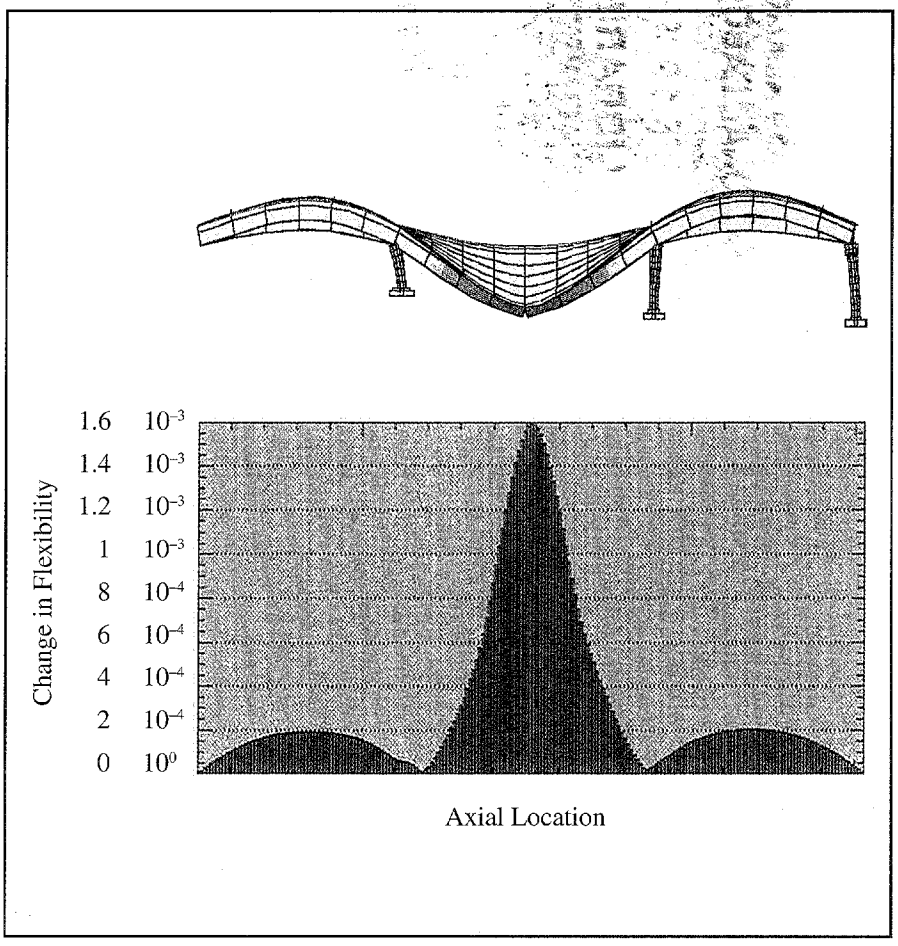

SCANNED AUG 01 1997

LOS ALAMOS NATIONAL LABORATORY
3 9338 00324 3259

Los Alamos
NATIONAL LABORATORY

Los Alamos National Laboratory is operated by the University of California for the United States Department of Energy under contract W-7405-ENG-36.

Edited by Hector Hinojosa, Group CIC-1

Cover: The top figure is a finite element model of the first bending mode calculated for the eastern three spans of the I-40 Bridge. A crack opening in the plate girder can be seen in the middle of the center span. Shown below is a plot of a damage indicator function that is based on the change in the flexibility matrix that represents the structural properties of the bridge. The flexibility matrix is approximated from measured resonant frequencies and the corresponding measured mode shapes. Six modes were used in the calculation of this damage indicator function.

An Affirmative Action/Equal Opportunity Employer

This report was prepared as an account of work sponsored by an agency of the United States Government. Neither The Regents of the University of California, the United States Government nor any agency thereof, nor any of their employees, makes any warranty, express or implied, or assumes any legal liability or responsibility for the accuracy, completeness, or usefulness of any information, apparatus, product, or process disclosed, or represents that its use would not infringe privately owned rights. Reference herein to any specific commercial product, process, or service by trade name, trademark, manufacturer, or otherwise, does not necessarily constitute or imply its endorsement, recommendation, or favoring by The Regents of the University of California, the United States Government, or any agency thereof. The views and opinions of authors expressed herein do not necessarily state or reflect those of The Regents of the University of California, the United States Government, or any agency thereof. The Los Alamos National Laboratory strongly supports academic freedom and a researcher's right to publish; therefore, the Laboratory as an institution does not endorse the viewpoint of a publication or guarantee its technical correctness.

LA-13074-MS

UC-000
Issued: January 1996

Damage Detection Algorithms Applied to Experimental and Numerical Modal Data from the I-40 Bridge

Charles Farrar
David Jauregui

SCANNED AUG 0 1 1997

LOS ALAMOS NATL. LAB. LIBS.
3 9338 00324 3259

Los Alamos
NATIONAL LABORATORY
Los Alamos, New Mexico 87545

TABLE OF CONTENTS

LIST OF FIGURES

LIST OF TABLES

DAMAGE DETECTION ALGORITHMS APPLIED TO EXPERIMENTAL AND NUMERICAL MODAL DATA FROM THE I-40 BRIDGE

by

Charles Farrar and David Jauregui

ABSTRACT

In the 1960's and 1970's numerous bridges were built in the U.S. with a design similar to those on Interstate 40 (I-40) over the Rio Grande in Albuquerque, New Mexico. These bridges were built without structural redundancy and typically have only two plate girders carrying the entire dead and live loads. Failure of either girder is assumed to produce catastrophic failure of the bridge. The Federal Highway Administration (FHWA) and the National Science Foundation (NSF) have provided funds to New Mexico State University (NMSU) through the New Mexico State Highway and Transportation Department (NMSH&TD) and The Alliance For Transportation Research (ATR) for evaluation and testing of the I-40 Bridges.

Because the I-40 Bridges over the Rio Grande were to be razed during the summer of 1993, the investigators were able to introduce damage into the structure in order to test various damage identification methods. To support this research effort, NMSU contracted Los Alamos National Laboratory (LANL) to perform experimental modal analyses, and to develop experimentally verified numerical models of the bridge. Previous reports (LA-12767-MS and LA-12979-MS) summarize the results of the experimental modal analyses and the results obtained from numerical modal analyses conducted with finite element models. This report summarizes the application of five damage identification algorithms reported in the technical literature to the previously reported experimental and numerical modal data.

Damage or fault detection, as determined by changes in the dynamic properties or response of structures, is a subject which has received considerable attention in the technical literature beginning approximately 30 years ago, and with a significant increase in reported studies appearing during the last five years. The basic idea is that modal parameters, notably frequencies, mode shapes, and modal damping, are a function of the physical properties of the structure (mass, damping, stiffness, and boundary conditions). Therefore, changes in physical properties of the structure, such as its stiffness or flexibility, will cause changes in the modal properties. Early methods for detecting damage based on changes in the structure's dynamic properties primarily examined changes in the resonant frequencies. However, this parameter has proved to be insensitive to lower levels of damage and does not provide a means to locate the damage. Current methods that have shown promise in both detecting damage at an early stage and locating the damage examine changes in the mode shapes of the structure.

The major contribution of this study is a direct comparison of five damage identification methods that were applied to the same experimental and numerical modal data. The experimental data were measured on an actual highway bridge. The numerical data was generated from finite element models of the same bridge that had been benchmarked against the measured response. With the numerical models many more damage scenarios could be investigated to further study the relative accuracy of the various damage identification methods. In all cases, the numerical studies were intended to simulate the measurement techniques that would be used if these methods were to be incorporated into an on-line monitoring system for highway bridges. This restriction implies that dynamic properties must be measured from ambient traffic-induced vibration sources.

I. INTRODUCTION

In the 1960's and 1970's numerous bridges were built in the U.S. with a design similar to those on Interstate 40 (I-40) over the Rio Grande in Albuquerque, New Mexico, Fig. 1. These bridges were built without structural redundancy and typically have only two plate girders carrying the entire dead and live loads. Failure of either girder is assumed to produce catastrophic failure of the bridge. For this reason the bridges, which have been found to exhibit fatigue cracking from out-of-plane bending of the plate girders, are referred to as fracture-critical bridges. The Federal Highway Administration (FHWA) and the National Science Foundation (NSF) have provided funds to New Mexico State University (NMSU) through the New Mexico State Highway and Transportation Department (NMSH&TD) and The Alliance For Transportation Research (ATR) for evaluation and testing of the existing fracture-critical bridges over the Rio Grande. The project is intended to develop and field test new nondestructive testing technology and to create a detailed bridge management data base for this class of bridges. The NSF is providing funds to investigate the seismic capacity of bridges such as these that were built prior to the adoption of modern seismic design standards.

Because the bridges over the Rio Grande were to be razed during the summer of 1993, the investigators were able to introduce simulated fatigue cracks, similar to those observed in the field, into the structure in order to test various damage-identification methods and to observe the changes in load paths through the structure caused by the cracking. To support this research effort, NMSU contracted Los Alamos National Laboratory (LANL) to perform experimental modal analyses, and to develop experimentally verified numerical models of the bridge. Scientists from the LANL's Condensed Matter and Thermal Physics Group (MST-10) applied state-of-the-art sensors and data acquisition software for the modal tests. Engineers from the LANL's Engineering Analysis Group (ESA-EA) conducted ambient and forced vibration tests to verify detailed and simplified finite element models of the bridge. Forced vibration testing was done in conjunction with engineers from Sandia National Laboratory (SNL) who provided and operated a hydraulic shaker.

This report is the third in a series that summarizes the work performed at LANL on the I-40 Bridge project. The first report, "*Dynamic Characterization and Damage Detection in the I-40 Bridge Over the Rio Grande*," (Farrar, et al., 1994) summarizes the experimental modal analysis test procedures and the results that were obtained from these tests. This report also contains a detailed review of the literature on bridge testing and a brief review of the literature on the application of damage identification methods to bridge structures. Results of the testing reported in this document have been forwarded to researchers at the Univ. of Houston, the Univ. of Colorado, Stanford Univ., Texas A&M Univ., SNL and NMSU. The second report, "*Finite Element Analysis of the I-40 Bridge Over the Rio Grande*," (Farrar, et al., 1996) summarizes the results of numerical models of the bridge and compares results obtained with these models to the measured dynamic properties of the bridge. The benchmarked finite element models (FEM) will now be used to make an extensive comparison of various damage-identification algorithms.

In this report five damage identification methods that have been reported in the technical literature were programmed in MATLAB (The Mathworks (1992)) and then applied to the experimental modal data measured on the I-40 Bridge. Subsequently, the same methods were applied to numerically generated modal data obtained from the finite element models previously mentioned. Once benchmarked against measured modal data from the I-40 Bridge in both its undamaged and damaged condition, the finite element models can be used to investigate a wide variety of damage scenarios.

A future goal of a comprehensive bridge management system is to have a self-monitoring bridge where sensors feed measured responses (accelerations, strains, etc.) into a local computer. This computer would, in turn, apply a damage identification algorithm to this data to determine if the bridge has significantly deteriorated to the point where user safety may be jeopardized. The local

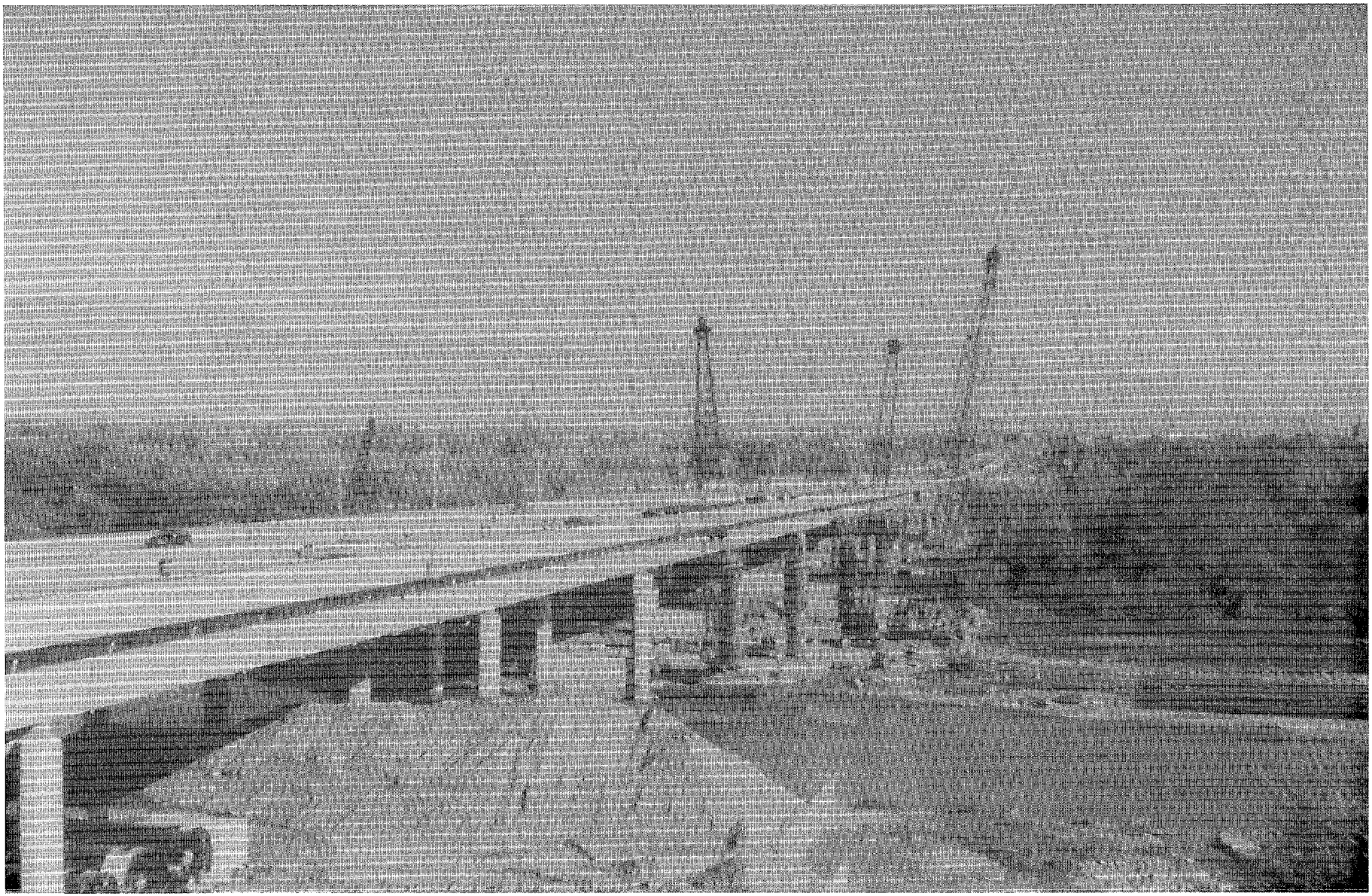

Fig. 1. I-40 Bridges over the Rio Grande in Albuquerque, New Mexico.

computer could then contact a central monitoring facility (via cellular phone) to notify the appropriate maintenance or safety officials of the bridge's current condition. If such a monitoring system is to be practical, it will have to identify the dynamic properties of the structure from ambient, traffic-induced vibration. To this end, all dynamic properties that have been identified by finite element analyses were determined without use of the measured input to the structure.

II. SUMMARY OF DAMAGE DETECTION METHODS APPLIED TO BRIDGES

An extensive, recent survey of bridge failures in the United States since 1950 is presented by Shirole and Holt (1991). These authors point out that recent responses of engineers to bridge failures have been reactive. Bridge design modifications and inspection program changes are often made in response to catastrophic failures. The collapse of the Tacoma Narrows Bridge a half century ago is, of course, classic and has led to the inspection and modification of other suspension bridges. The widespread introduction of systematic bridge inspection programs was directly attributed by Shirole and Holt to the catastrophic bridge collapse at Point Pleasant, WV, in 1967. These authors point out that there is no national data base that summarizes bridge failures. Design modifications for seismic response of bridges have been made as a direct consequence of damage sustained by highway bridges during the 1971 San Fernando Earthquake (Gates, 1976).

At present, bridges are generally rated and monitored during biennial inspections, largely using visual inspection techniques that are discussed by White, et al. (1992). There is the possibility that damage could go undetected at inspection or that growth of cracks in load-carrying members to critical levels, for instance, could occur between inspection intervals (see Biswas, et al. (1990)). Sudden damage leading to bridge collapse also occurs due to collision, as evidenced by the 1993 AMTRAK railroad bridge collapse in the Southeastern US involving collision of the supporting pier by a barge. (According to statistics presented by Shirole and Holt, more than 13% of identified failures of US bridges since 1950 are attributed to collision). Based on these findings, it appears that a quantitative, possibly continuous, mechanism of bridge damage detection is appropriate to prevent or, at least, mitigate the effects of future bridge failures. As well, use of an active damage detection system may be used to detect sudden significant damage to the bridge structure caused by collision, and trigger a system to close the bridge to traffic.

The interest in the ability to monitor a structure and detect damage at the earliest possible stage is pervasive throughout the civil, mechanical, and aerospace engineering communities. Current damage detection methods are either visual or localized experimental methods such as acoustic or ultrasonic methods, magnet field methods, radiographs, eddy-current methods and thermal field methods. All these experimental methods require that the vicinity of the damage is know *a priori* and that the portion of the structure being inspected is readily accessible. Subjected to these limitations, these experimental methods can detect damage on or near the surface of the structure. The need for more global damage detection methods that can be applied to complex structures has led to the development of damage identification methods that examine changes in the vibration characteristics of the structure.

Global damage or fault detection, as determined by changes in the dynamic properties or response of structures, is a subject which has received considerable attention in the technical literature beginning approximately 30 years ago. A significant increase in reported studies has appeared during the last five years. These damage detection methods can be classified into four levels:

1. Identify that damage has occurred,

2. Identify that damage has occurred and determine the location of damage,

3. Identify that damage has occurred, locate the damage, and estimate its severity, and

4. Identify that damage has occurred, locate the damage, estimate its severity, and determine the remaining useful life of the structure.

The basic premise of the global damage detection methods that examine changes in the dynamic properties is that modal parameters, notably frequencies, mode shapes, and modal damping, are a function of the physical properties of the structure (mass, damping, stiffness, and boundary conditions). Therefore, changes in physical properties of the structure, such as its stiffness or flexibility, will cause changes in the modal properties. Early methods for detecting damage based on changes in the structure's dynamic properties primarily examined changes in the resonant frequencies. However, this parameter has proven to be insensitive to lower levels of damage and does not provide a means to locate the damage. Current methods that have shown promise in both detecting damage at an early stage and locating the damage examine changes in the mode shapes of the structure.

The summary of the literature presented below has been limited to damage detection methods applied to bridges. These methods provide damage detection levels ranging from one to three. A more thorough summary of damage identification from changes in dynamic properties of structures can be found in Doebling, et al. (1996).

A detailed survey of the technical literature and interviews of selected experts to determine the state-of-the-art of the damage detection field (using such modal changes) as of 1979 was presented by Richardson (1980). The survey focused on structural integrity monitoring for nuclear power plants, large structures, rotating machinery and offshore platforms, with by far the largest amount of literature associated with rotating machinery. The author stated that while monitoring of overall vibration levels for rotating machinery had become commonplace, attempts at relating structural damage to measured modal changes was still in its primitive stages. While modal testing of suspension bridges is discussed, the work was for system identification (i.e., determination of mode shapes, modal damping and resonant frequencies) and not specifically directed at damage determination.

Since 1979, numerous studies involving the development and application of damage detection techniques have been reported for bridge structures. Salane, et al. (1981) examined changes in dynamic properties (damping and resonant frequencies) of a 3-span highway bridge during a fatigue test as a possible means of detecting structural deterioration caused by fatigue cracks in the bridge girders. The authors found that changes in damping were inconsistent and could not be used to detect fatigue damage in bridges. Changes in vibration signatures (mechanical impedance plots, Fourier transform of velocity response normalized by the Fourier transform of force input) were also found to be poor indicators of structural deterioration caused by fatigue. Changes in experimentally determined mode shapes were found to be more sensitive indicators of damage. For these tests sinusoidal excitation was applied with an electro-hydraulic actuator.

Kato and Shimada (1986) performed ambient vibration measurements on an existing prestressed concrete bridge during a test to failure. A reduction in natural frequencies could be detected as a statically applied load approached the ultimate load. Significant changes in resonant frequencies were associated with yielding of the prestressing tendons. However, damping values were not affected significantly. The ambient vibration method of system identification was used.

Turner and Pretlove (1988) performed a numerical analysis of the vibration response of a simple beam representation of a bridge subjected to random traffic loading. The authors suggested that measurement of the response of a bridge to traffic appeared to provide a method of determining resonant frequencies. These frequencies could then be monitored: a 5% change would indicate changes in the bridge condition beyond those that can be attributed to environmental effects. The motivation of the work was to develop a structural condition monitoring system without a measured source of vibrations.

Spyrakos, et al. (1990) performed an experimental program on test beams which were designed to respond in a dynamically similar fashion to actual bridges. Each beam was given different damage scenarios (type, location, degree), on which low-level free vibration tests were performed. The authors found a definite correlation between level of damage and dynamic characteristics of the structure. It was found that frequency change may be insufficient to be a useful indicator of structural safety (less than 5% change in frequency was associated with "critical" damage). However, the study suggests that the method of relating changes in resonant frequencies to damage level may be applicable to more severely damaged structures, and can give an indication of remaining serviceability. The authors state that mode shapes may be used to locate damage if the input to the structure is measured.

Mazurek and DeWolf (1990) again presented strong arguments for the need of a continuous automated vibration monitoring system for highway bridges, citing several unexpected collapses and near collapses of bridges (the collapse of one Rhode Island bridge was prevented when a passerby observed severe cracking of a primary girder at mid span). In their experimental study of a bridge monitoring technique, the authors performed laboratory model tests on a 2-span aluminum plate-girder bridge, with vibrations induced by vehicular excitation. The authors found that major structural degradation can cause significant changes to both resonant frequencies and mode shapes. The greatest changes in mode shapes occur in the vicinity of the structural defect (e.g., crack). Therefore, once it is determined that a structural defect is present, mode shapes could be used to locate the defect.

Biswas, et al. (1990) discussed the state of degradation of bridges in the U.S., emphasizing that the current 24-month inspection interval for highway bridges has two major drawbacks: Bridge failure could occur between inspection intervals; and incipient failures may go unnoticed during inspection. They performed modal testing on a 2-span continuous composite bridge in undamaged and "damaged" condition. "Damage" consisted of a large fatigue crack simulated by unfastening a set of bolts at a steel girder splice connection. Changes in frequency response functions (FRFs, Fourier transform of a response measurement normalized by the Fourier transform of a reference measurement) obtained by using a shaker were found to be detectable and quantifiable. Modal frequencies showed small but consistent drops caused by the presence of the simulated crack. Time histories and their corresponding Fourier spectra showed changes, but these changes were difficult to correlate with damage. Changes in mode shapes as quantified by the modal assurance criteria (see Eq. 1 in Sec. III.B.3.b) were found to be the best indicator of damage.

In related work by the same authors (Samman, et al., 1991), a plastic scale model of a typical highway bridge was used to investigate the change in FRF signals caused by the development of girder cracks. The authors used a procedure from the field of pattern recognition to accentuate the differences in the FRFs between cracked and uncracked bridges. The method also provided some crack location information.

Jain (1991), also using modal methods, investigated the performance characteristics of a continuously deteriorating railway bridge using a locomotive run at constant speed for the excitation source. Jain concluded that modal parameters, particularly frequencies and mode shapes, can furnish only general information on the damage state of the structure: deviation in these parameters indicates that damage has occurred, but not its local extent or underlying cause.

Tang and Leu (1991) performed experiments on a defective prestressed concrete girder bridge. They found that mode shape changes may be a more effective indicator for damage detection in bridges than frequency shifts. To be effective for damage detection, they state that a frequency shift on the order of 0.01 Hz must be detectable. Bridge excitation was accomplished by the step relaxation method.

Raghavendrachar and Aktan (1992) performed impact testing on a 3-span reinforced concrete bridge with a goal of detecting local or obscure damage, as opposed to severe, global damage. The authors concluded that modal parameters may not be reliable as indicators of local damage if only the first few modes are determined. For this type of damage, modal information for higher modes would be required. However, the authors examine changes in flexibility as determined from mode shapes and resonant frequencies and found that flexibility was a much more sensitive indicator of damage, particularly when only a limited number of modes are available.

Law, et al. (1992) tested a one-fifth scale model of a reinforced concrete beam-slab bridge deck. Damage was introduced by applying static loads until failure. Ambient vibration sources were used to excite the bridge during dynamic tests. Frequency response functions were calculated between various measurements locations. Sensitivity equations were developed that relate the changes in mass, stiffness, and damping to changes in the frequency response functions. Results of these analyses showed that changes in the FRFs revealed the damage that was introduced by the static loading.

An extensive survey and analysis of structural damage detection was prepared by Kim and Stubbs (1993) as part of the I-40 bridge project. The authors assessed the relative impact of model uncertainty on the accuracy of nondestructive damage detection in structures. The authors applied their damage index approach analytically to a plate-girder bridge and a 3-dimensional truss-type bridge.

Toksoy and Aktan (1994) applied a damage detection method that examines changes in flexibility to a three span concrete deck bridge. Multi-reference impact testing was used to measure the resonant frequencies and the mass-normalized mode shapes of the structure. The authors also discuss methods that use finite element analysis in the event that a baseline undamaged measurement is not available. They use the measured flexibility matrix to assign a condition index to a bridge. By comparing cross-sectional deflection profiles from the flexibility matrices, they are able to detect structural damage and anomalies. Results are presented both with and without original data. When original data is not available, the measured flexibility is compared to FEM flexibility, with anomalies in the deflection profile of the measured flexibility used to locate damage. When a baseline data set is available, the deflection profiles are compared directly. These authors point out that problems related to long term sensor and data-acquisition reliability must be overcome before it will be possible to field a continuous health-monitoring system.

Aktan, et al. (1994) discuss the application of damage detection methods based on modal testing to seven highway bridges, particularly a three-span steel-stringer bridge and a steel truss bridge. Changes in flexibility based on measured resonant frequencies and mass-normalized mode shapes were used to assess damage. Accuracies of the flexibility approximations obtained from modal properties were determined from static load testing. Multi-reference impact testing was again used to determine the resonant frequencies and the mass-normalized mode shapes. Approximately twenty mode were necessary to accurately define the bridges' flexibility matrix. They estimated that the error in measured flexibility due to modal truncation was about 2% after 18 modes had been included.

Aktan, et al. (1995) summarize a mobile field testing laboratory developed for damage detection in bridges. This laboratory will allow strain data to be collected along with multi-input/multi-output structural dynamics data.

Mayes (1995) applied the Structural Translation and Rotation Error Checking (STRECH) algorithm to modal data from the I-40 Bridge. This method examines changes in displacement after damage normalized by the before damage value for a given load, referred to as the stretch ratio, to locate areas where the stiffness of the structure has been reduced. The author applied this method to rotational displacements determined by curve-fitting the individual translational mode

shapes of the bridge, and to static flexibility shapes determined from the first six resonant frequencies and measured mass-normalized mode shapes. Damage was identified and located for the more severe cases.

Stubbs, et al. (1995) applied a damage index method to mode shape data from the I-40 Bridge tests and was able to identify and locate the defect for even the most benign damage case. The method used only the first three modes, which were determined from ambient vibration data reduction techniques, and did not require the modes to be mass normalized. This method is based on measuring changes in the strain energy stored in the beam-like structure before and after damage has occurred as determined from changes in the curvature of the mode shapes.

James, et al. (1995) present the results of two damage location techniques applied to data from the I-40 Bridge. The STRECH technique is used to locate differences in stiffness between the measurements and the FEM on a mode-by-mode basis. The MAtriX COmpletioN (MAXCON) technique is a method for completing the rank of the measured mass matrix such that the mass matrix sparsity is enforced. The measured stiffness matrix is then computed from this rank-enriched measured mass matrix. The results of this test indicate that the STRECH technique gives a better global indication of damage, but that the MAXCON technique appears to be more robust to measurement errors and more applicable to measured dynamic data.

Liang, et al. (1995) apply a damage identification method based on modal energy transfer ratio (ETR) to data obtained on the steel Peace Bridge over the Niagara River near Buffalo, NY. Because no damage could be added to the bridge, the authors used the test as an opportunity to study the repeatability of the necessary parameters, and to observe the changes in the structure caused by construction repair work. Accelerometer measurements were used in the testing, and the excitation was provided using both impact hammer and ambient signals from automobile traffic. It was demonstrated that the ETR has the highest repeatable signal-to-noise ratio of any of the damage measures considered. The impact hammer tests yielded better overall results than the ambient input tests.

Doebling (1995) presents the results of a flexibility-based damage analysis on the I-40 Bridge data. The results indicate that the flexibility coefficients computed using just the measured modes can provide an accurate indication of the location of damage. As with most other damage detection techniques based on modal vibration data, the damage location results are much more significant when the damage causes a large change in structural stiffness as compared to the results from a slight change in structural stiffness. The results are also shown to improve when the estimated residual flexibility coefficients are included in the computation of the measured flexibility.

Zhang and Aktan (1995) use changes in curvatures of the uniform load surface (the deformed shape of the structure when subjected to a uniform load), calculated using the uniform load flexibilities, to identify damage in a numerical simulation of a three-span concrete deck supported by steel stringers. Results from impact and forced vibration modal tests were used to benchmark a numerical model of the bridge. Damage was introduced in the numerical model by changing the stiffness of an element in the model. The change in curvature was shown to be a sensitive indicator of this local damage. Changes in other modal parameters (resonant frequencies and mode shapes) were shown be insensitive to the damage.

Simmermacher, et al. (1995) examine the effects of finite element mesh density on successful application of the matrix update algorithms. This study was motivated by the fact that large models are necessary to reduce discretization error in the finite element models. Matrix updating procedures inherently require model reduction and/or mode shape expansion, which destroy the load paths and therefore decreases the ability of such algorithms to locate damage at the element level. This research examined the trade-offs between large and small FEMs for application of the

minimum rank perturbation theory to the I-40 Bridge data. Small models were found to work well for damage detection if they can be adjusted to accurately predict the mode shapes of the structure.

Summarizing, it appears that over the past fifteen years there has been repeated application of the use of modal properties of bridges to the fields of damage detection and structural health monitoring, much of the work having been motivated by several catastrophic bridge failures. Earlier work utilized primarily modal frequency changes to detect damage, but others have lately shown that frequency changes are insufficient, and that changes in mode shapes are more sensitive indicators and might be useful for detection of the defect location as well. Damping changes have not been found useful for damage detection in bridges. Finally, other more sensitive methods of examining modal properties for damage are being developed. These newer methods examine changes in flexibility matrices determined from modal parameters, changes in the strain energy stored in a structure, and changes in mode shape curvature.

III. DESCRIPTION OF EXPERIMENTAL AND NUMERICAL TEST DATA

The experimental data used in this study came from tests performed on one of the I-40 Bridges over the Rio Grande in Albuquerque, NM. A summary of the test procedures and results is given below. Mode shape data obtained from these tests are summarized in Appendix A. For a more detailed summary of the tests performed on the I-40 Bridge and the results that were obtained, the reader is referred to Farrar, et al. (1994). Numerical data used in this study were generated with finite element models of the same I-40 Bridge. These models are also summarized below, and a more detailed discussion of the finite element models can be found in Farrar, et al. (1996).

III. A. I-40 Bridge Geometry

The I-40 Bridges over the Rio Grande that were tested consist of twin spans (there are separate bridges for each traffic direction) made up of a concrete deck supported by two welded-steel plate girders and three steel stringers. Loads from the stringers are transferred to the plate girders by floor beams located at 20-ft intervals. Cross-bracing is provided between the floor beams. Figure 2 shows an elevation view of the portion of the bridge that was tested. The cross-section geometry of each bridge is shown in Fig. 3, and Fig. 4 shows the actual substructure of the bridge.

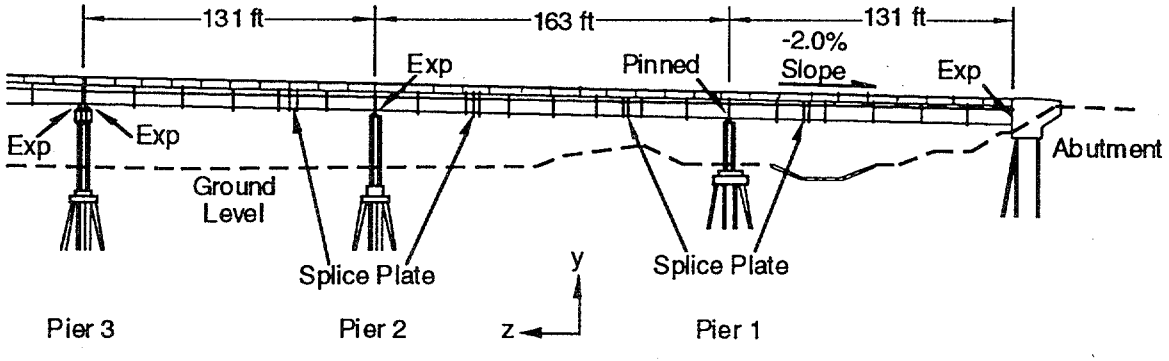

Fig.2. Elevation view of the portion of the eastbound bridge that was tested.

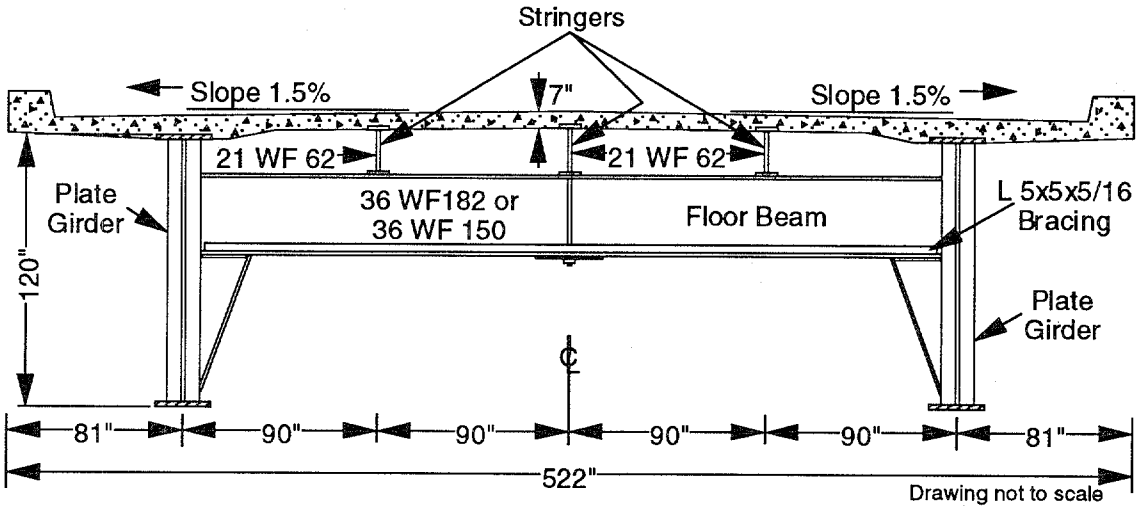

Fig. 3. Typical cross-section geometry of the bridge.

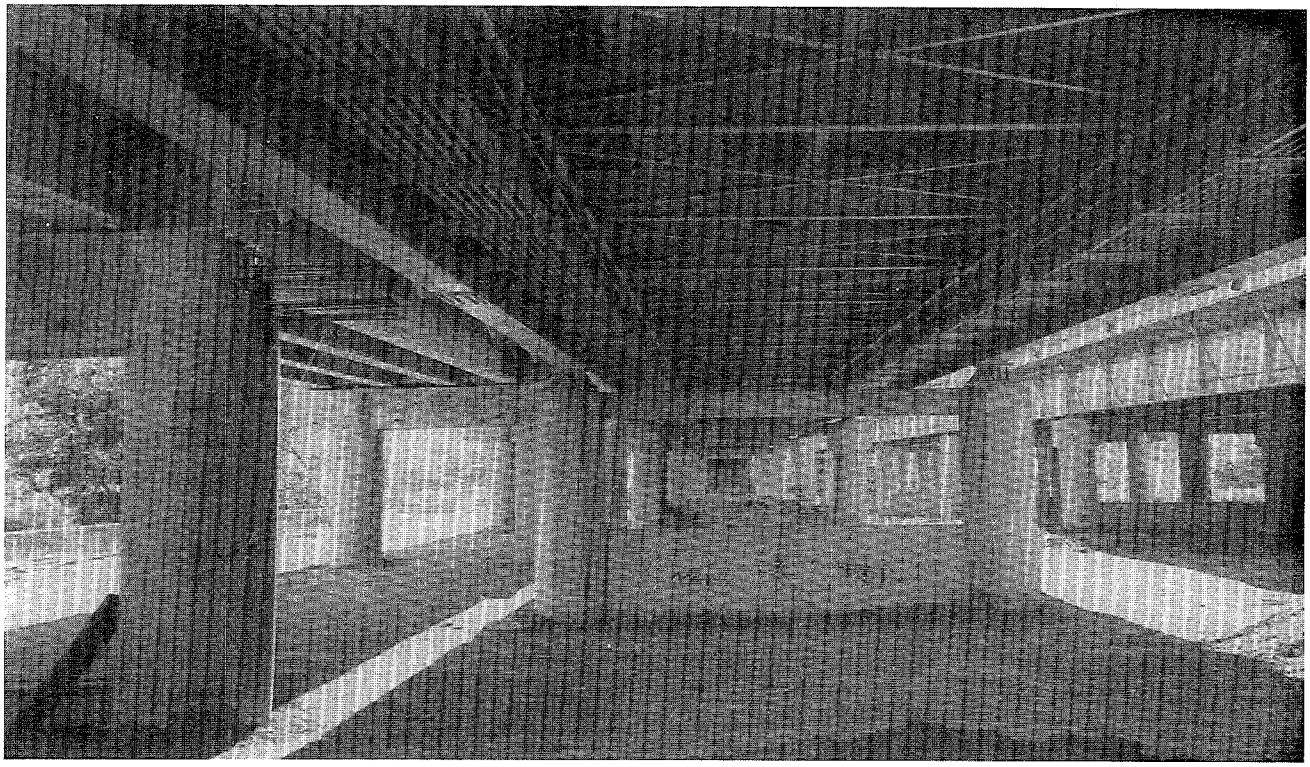

Fig. 4. Bridge substructure.

Each bridge is made up of three identical sections. Except for the common pier located at the end of each section, the sections are independent. A section has three spans; the end spans are of equal length, approximately 131 ft, and the center span is approximately 163 ft long. Five plate girders are connected with four bolted splices to form a continuous beam over the three spans. The portions of the plate girders over the piers have increased flange dimensions, compared with the midspan portions, to resist the higher bending stresses at these locations. Connections that allow for thermal expansion, Figs. 5 and 6, as well as connections that prevent longitudinal translation, Fig. 7 are located at the base of each plate girder, where the girder is supported by a concrete pier or abutment. These connections are labeled "exp" and "pinned" in Fig. 2. When the concrete deck was removed, no shear studs were found on the top flanges of the plate girders or stringers.

All subsequent discussions of the bridge will refer to the bridge carrying eastbound traffic, particularly the three eastern spans, which were the only ones tested.

III. B. I-40 Bridge Test Data

This section provides a brief summary of the experimental results that were obtained from forced vibration tests performed on the I-40 Bridge. Forced vibration tests were performed when the bridge was in an undamaged state and after each of four incremental levels of damage had been introduced.

III. B. 1. Data Acquisition

The data acquisition system used in these tests consisted of a computer workstation which controlled 29 input modules and a signal processing module. The workstation was also the platform for a commercial data-acquisition/signal-analysis/modal-analysis software package. The input modules provided power to the accelerometers and performed analog-to-digital conversion of the accelerometer voltage-time histories. The signal-processing module performed the needed fast Fourier transform calculations. A 3500-watt AC generator was used to power this system in the field.

Two sets of integrated-circuit, piezoelectric accelerometers were used for the vibration measurements. A coarse set of measurements was first made with twenty-six PCB model 336C accelerometers. These accelerometers were mounted on one-inch square aluminum mounting blocks that were dental-cemented to the inside web of the plate girder at mid-height and at the axial locations shown in Fig. 8. Within a span the three blocks were equally spaced in the axial direction. Accelerometers were mounted on the blocks with a 10-32 stud, in the global Y direction as shown in Fig. 8. These accelerometers had a nominal sensitivity of 1 V/g, a specified frequency range of 1-2000 Hz, and an amplitude range of ± 4 g's. Twelve-inch-long 50-Ohm MicroDot cables attached to two conductor, PVC-jacketed 20-gauge cables ranging from 70 ft to 291 ft connected the accelerometers to the input modules. The cables were supported by the catwalks located along each plate girder, tied off, and dropped down to the van located under the bridge that housed the data acquisition system.

Sampling parameters were specified that calculated the FRFs and cross-power spectra (CPS) from 32-s time windows discretized with 1024 samples. Therefore, the FRF and CPS were calculated for frequency ranges of 0-12.5 Hz. Thirty averages were used to calculate the FRF and CPS. A frequency resolution of 0.03125 Hz, was obtained for the FRF and CPS. Hanning windows were applied to the time signals to minimize leakage, and AC coupling was specified to minimize DC offsets.

A more refined set of measurements was made near the damage location. Eleven Endevco 7751-500 accelerometers with a nominal sensitivity of 500 mV/g, a frequency range of 0.4 to 1500 Hz ,

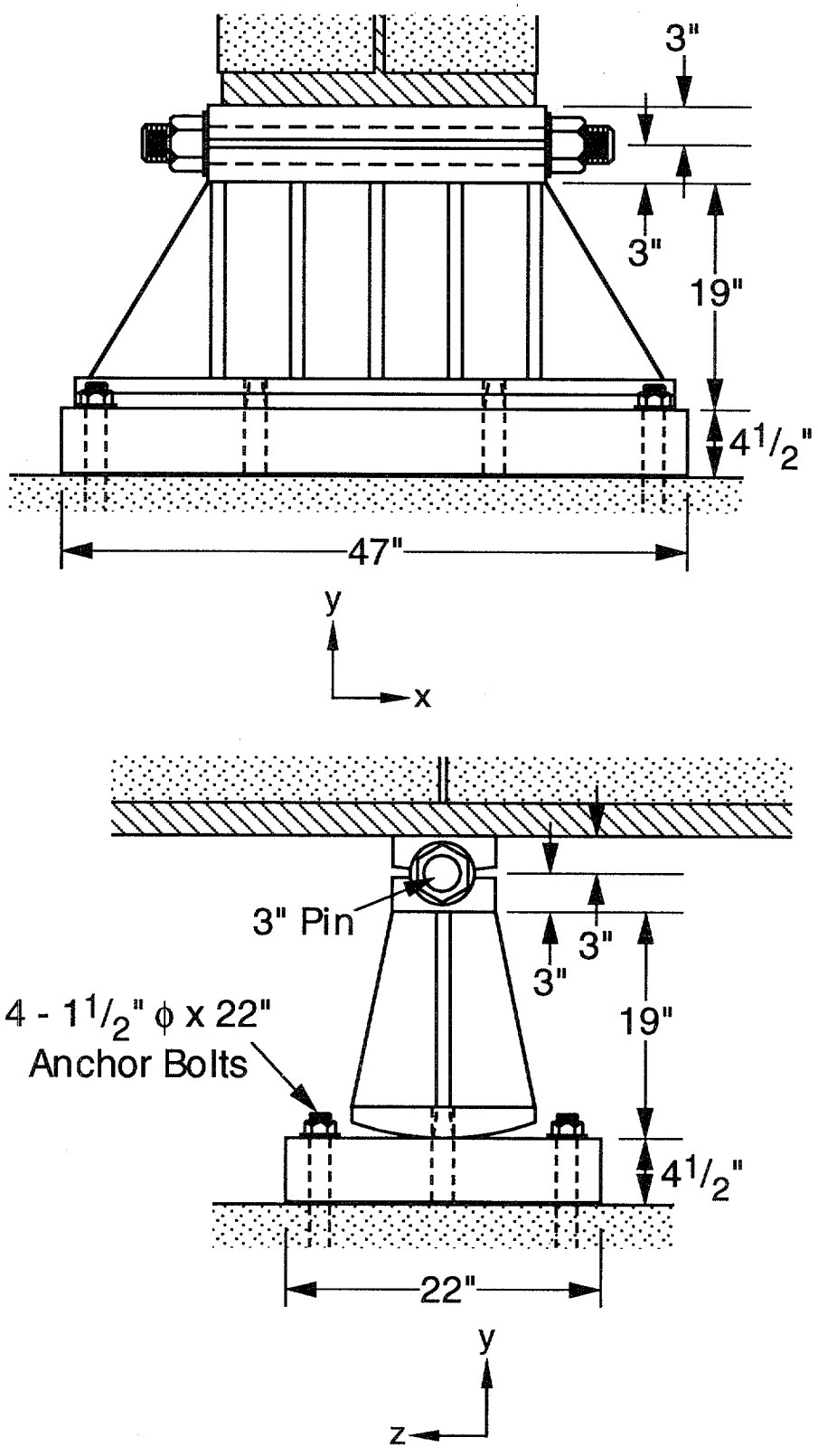

Fig. 5. Connection detail found at the abutment and Pier 3 that allows longitudinal displacement.

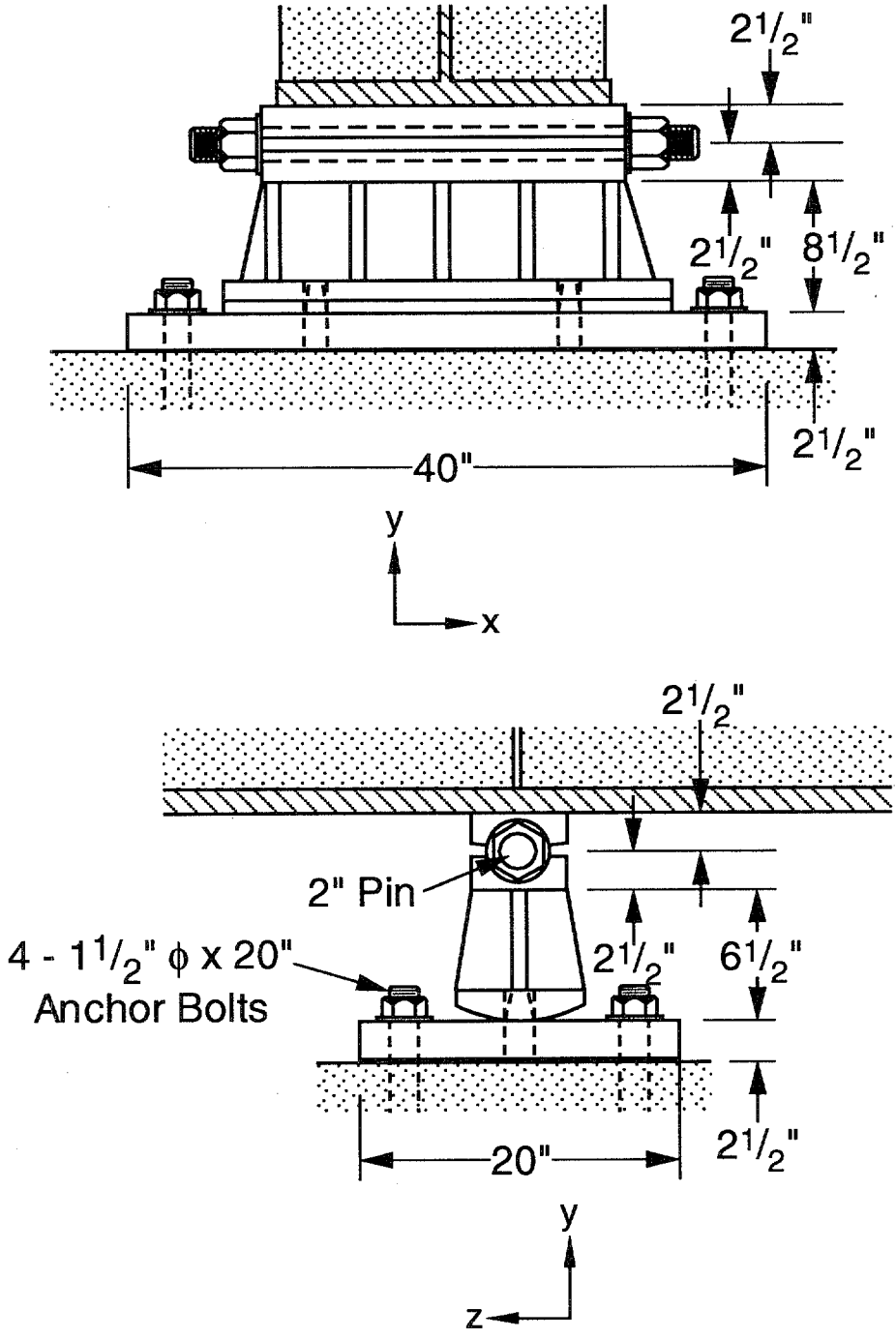

Fig. 6. Connection detail found at Pier 2 that allows longitudinal displacement.

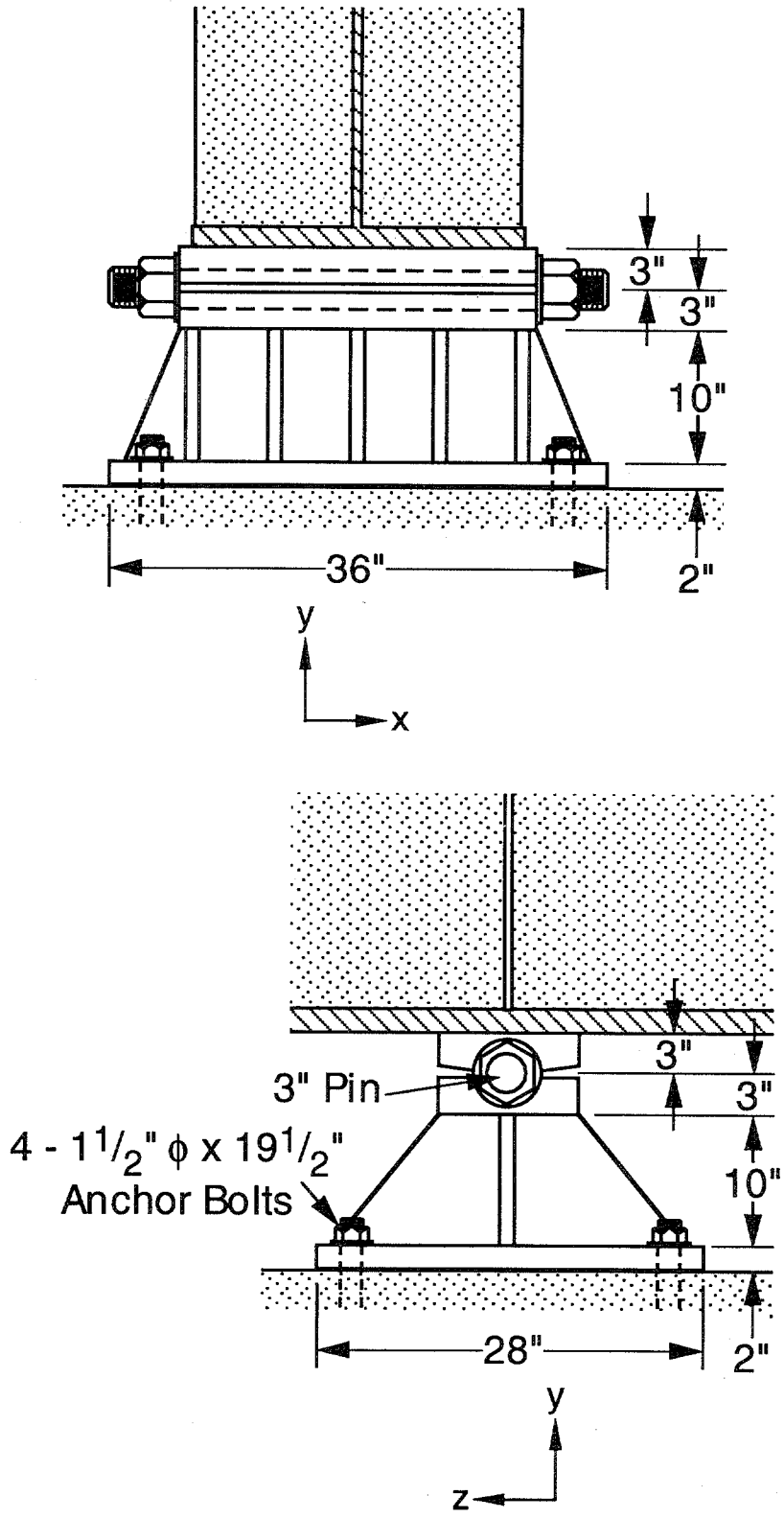

Fig. 7. Connection detail found at Pier 1 that constrains longitudinal displacement.

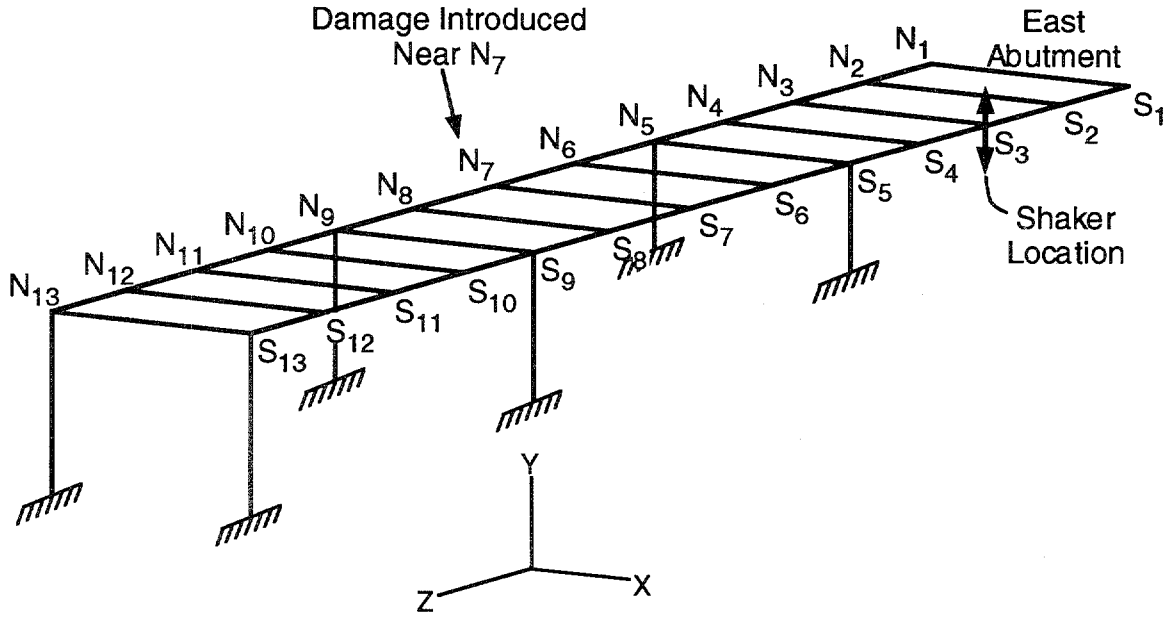

Fig. 8. Accelerometer locations.

and an amplitude range of ±10 g's were placed in the global Y direction at a nominal spacing of 16 ft along the midspan of the north plated girder. All accelerometers were located at midheight of the girder. The actual spacing of these accelerometers is shown in Fig. 9 . When the dental cement cured, some of the blocks used to mount these accelerometers were no longer vertical. X-3 was tilted 3.3 degrees to the east, X-5 was tilted 1.2 degrees to the west, X-8 was tilted 1.2 degrees to the east, and X-10 was tilted 1.8 degrees to east. The same data acquisition system, similar wiring, and identical sampling parameters as those used with the coarse accelerometer set were again used with this refined set of accelerometers.

III. B. 2. Forced Vibration Testing, Undamaged

From August 31st through September 2nd, 1993, a series of forced vibration tests were conducted on the undamaged bridge. Eastbound traffic had been transferred to a new bridge just south of the one being tested. The westbound traffic continued on the original westbound bridge. SNL provided a hydraulic shaker that generated the measured force input. Excitation from traffic on the adjacent bridges could be felt when the shaker was not running. Wind, although not measured, was not considered significant during these tests.

The Sandia shaker consists of a 21,700-lb reaction mass supported by three air springs resting on top of 55-gallon drums filled with sand. A 2200-lb hydraulic actuator bolted under the center of the mass and anchored to the top of the bridge deck provided the input force to the bridge. Figure 10 shows the shaker in place on the bridge. A random-signal generator was used to produce a uniform random signal that was band-passed between 2 Hz and 12 Hz before inputting the signal to an amplifier. The amplifier gain was controlled manually to provide an approximately 2000-lb peak, random force input. An accelerometer mounted on the reaction mass was used to measure the force input to the bridge. This indirect force measurement gives the total force transferred to the bridge through the 55-gallon drums as well as the actuator. The shaker was located over the south plate girder directly above point S-3 in Fig. 8. The accelerometer used to measure force was

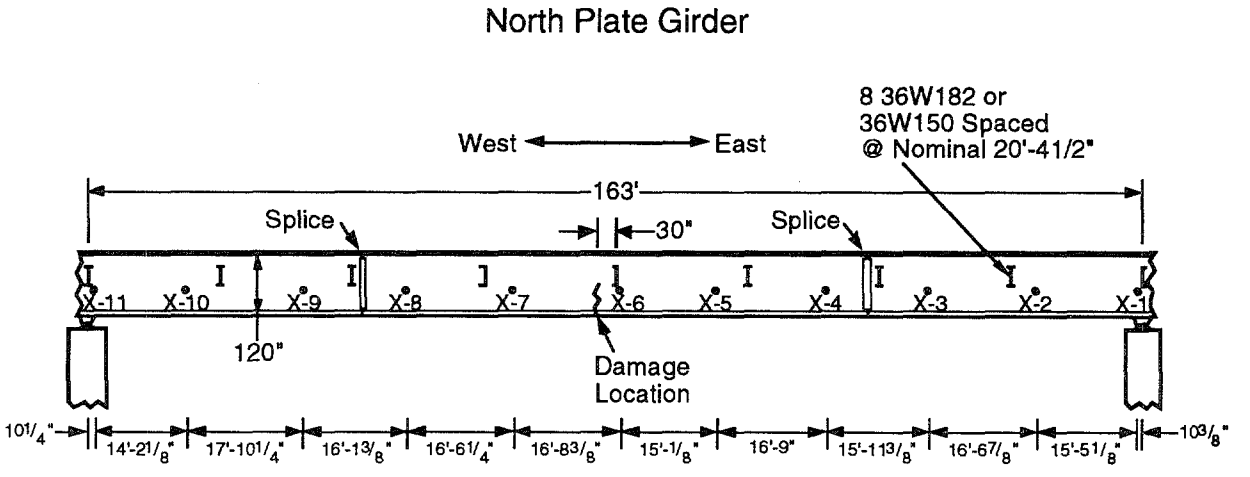

Fig. 9. Locations of the refined set of accelerometers.

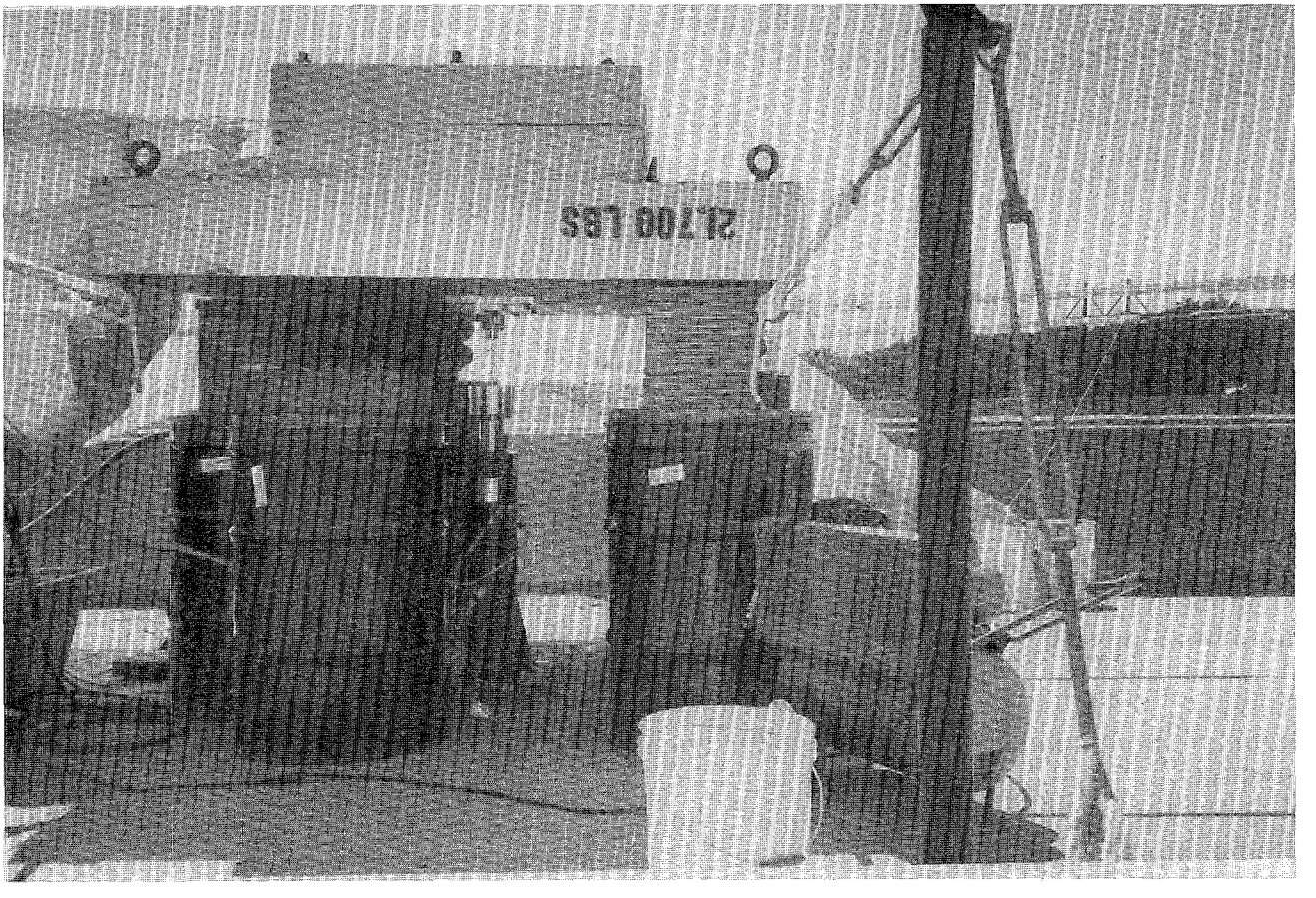

Fig. 10. The Sandia shaker in place on the I-40 Bridge.

oriented such that a positive force corresponded to the positive global Y direction shown in Fig. 8. A more detailed summary of the Sandia shaker can be found in Mayes and Nusser (1994).

Forced vibration tests using the coarse set of accelerometers were conducted with a random input so that ESA-EA personnel could perform experimental modal analyses of the bridge. In this context experimental modal analysis refers to the procedure whereby a measured excitation (random, sine, or impact force) is applied to a structure, and the structure's response (acceleration, velocity, or displacement) is measured at discrete locations that are representative of the structure's motion. Both the excitation and the response time histories are transformed into the frequency domain in the form of FRF (the Fourier transform of the response normalized by the Fourier transform of the input). Modal parameters (resonant frequencies, mode shapes, modal damping) can be determined by curve-fitting a Laplace domain representation of the equations of motion to the measured frequency domain data (Ewins, 1985).

A rational-fraction polynomial, global, curve-fitting algorithm in a commercial modal analysis software package (Structural Measurements Systems, 1987) was used to fit the analytical models to the measured FRF data and to extract resonant frequencies, mode shapes, and modal damping values. Figures 11 through 16 show the first six modes of the undamaged bridge identified from these data. Mode shape amplitudes and phases along with resonant frequencies and modal damping values, corresponding to the mode shown in Figs. 11 through 16, are summarized in Appendix A, Table A-6.

Immediately after the forced vibration tests with the coarse accelerometers were complete, the random excitation tests were repeated using the refined set of accelerometers. For these tests the input was not monitored and mode shapes were determined from amplitude and phase information contained in CPS of the various accelerometer readings relative to the accelerometer X-3 shown in Fig. 9. Determining mode shapes in this manner, as discussed by Bendat and Piersol (1980), simulates the methods that would have to be employed when the response to ambient excitations are measured. The amplitude of a mode corresponding to location X-3 was obtained from the power spectrum of the signal measured at this location. The mode shape data obtained from this set of accelerometers for the first three modes of the bridge in the undamaged state are tabulated in Appendix A, Table A-1.

III. B. 3. Forced Vibration Testing, Damaged

From September 3rd through 11th, 1993, four different levels of damage were introduced into the middle span of the north plate girder. Forced vibration tests, with the coarse and refined sets of accelerometers, similar to those done on the undamaged structure were repeated after each level of damage had been introduced. Weather conditions during these tests were similar to those reported for the forced vibration tests. Background sources of vibration were also similar.

III. B. 3. a. Damage Description

The damage that was introduced was intended to simulate fatigue cracking that has been observed in plate-girder bridges. This type of cracking results from out-of-plane bending of the web and usually begins at welded attachments to the web such as the seats supporting the floor beams. Four levels of damage were introduced to the middle span of the north plate girder close to the seat supporting the floor beam at midspan. Damage was introduced by making various torch cuts in the web and flange of the girder. The first level of damage consisted of a two-foot-long, 3/8-in-wide cut through the web centered at midheight of the web. Next, this cut was continued to the bottom of the web . During this cut the web, on either side of the cut, bent out of plane approximately 1 in. The flange was then cut halfway in from either side directly below the cut in the web. Finally, the flange was cut completely through leaving the top 4 ft of the web and the top flange to carry the load at this location. The various levels of damage are shown in Figs. 17 through 20.

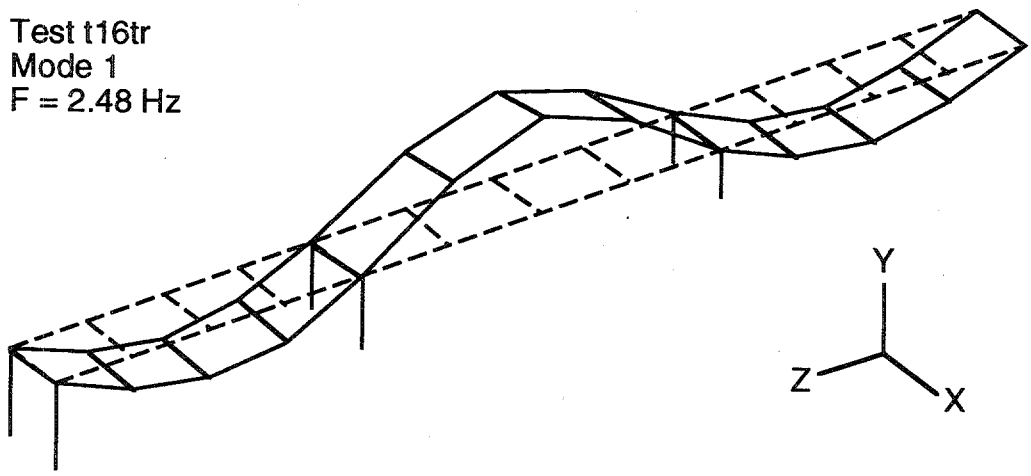

Fig. 11. First flexural mode identified from undamaged forced vibration data, test t16tr.

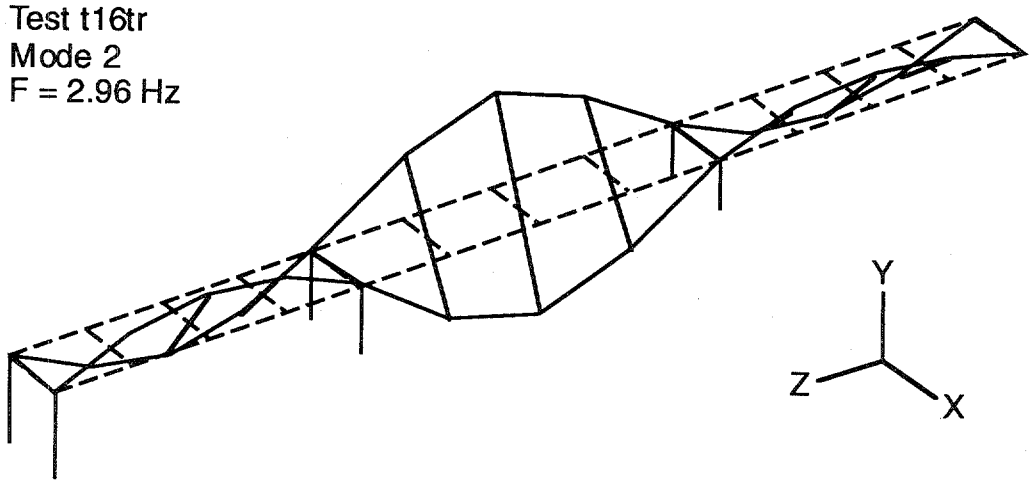

Fig. 12. First torsional mode identified from undamaged forced vibration data, test t16tr.

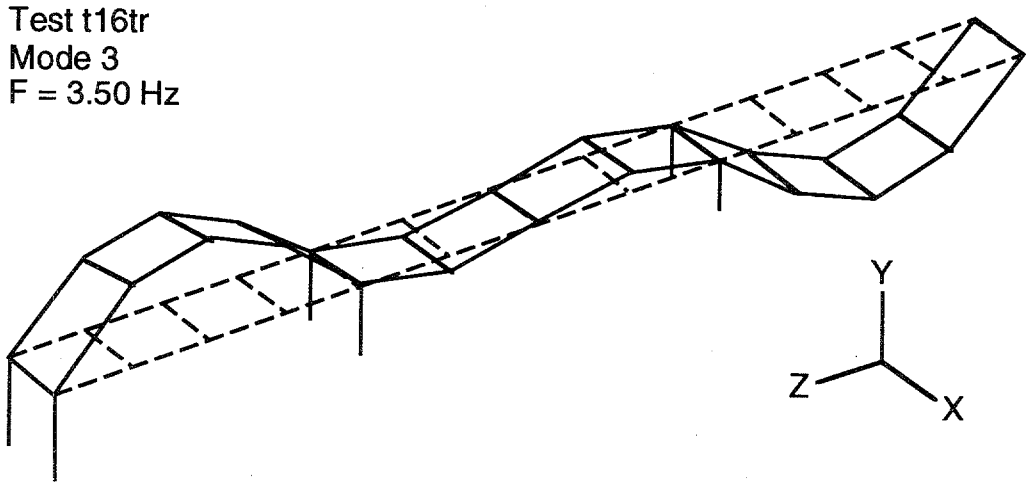

Fig. 13. Second flexural mode identified from undamaged forced vibration data, test t16tr.

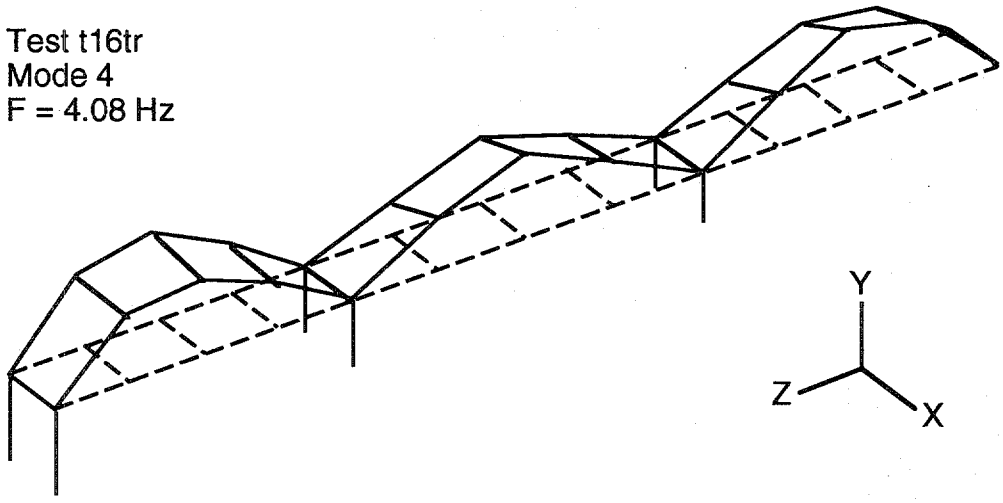

Fig. 14. Third flexural mode identified from undamaged forced vibration data, test t16tr.

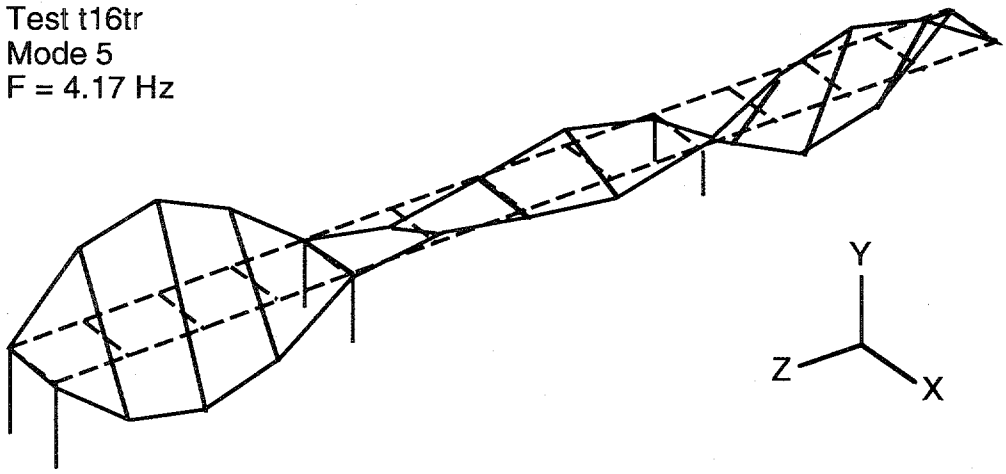

Fig. 15. Second torsional mode identified from undamaged forced vibration data, test t16tr.

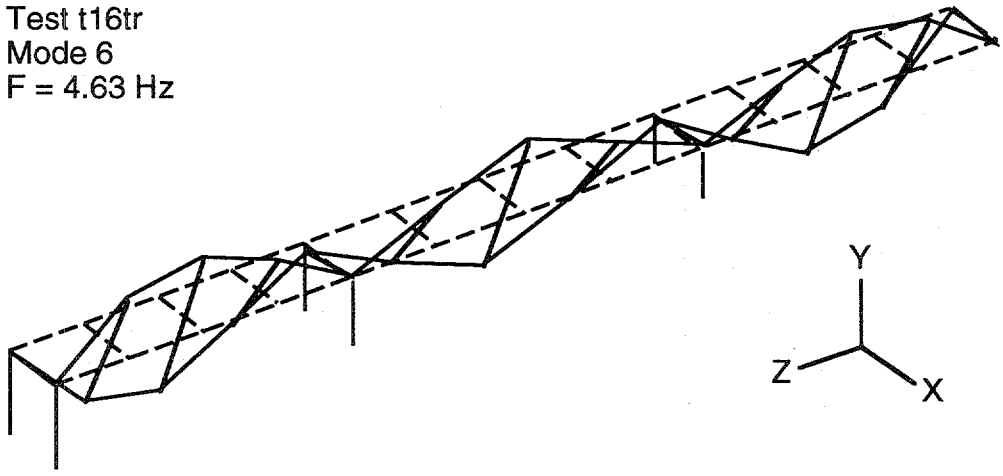

Fig. 16. Third torsional mode identified from undamaged forced vibration data, test t16tr.

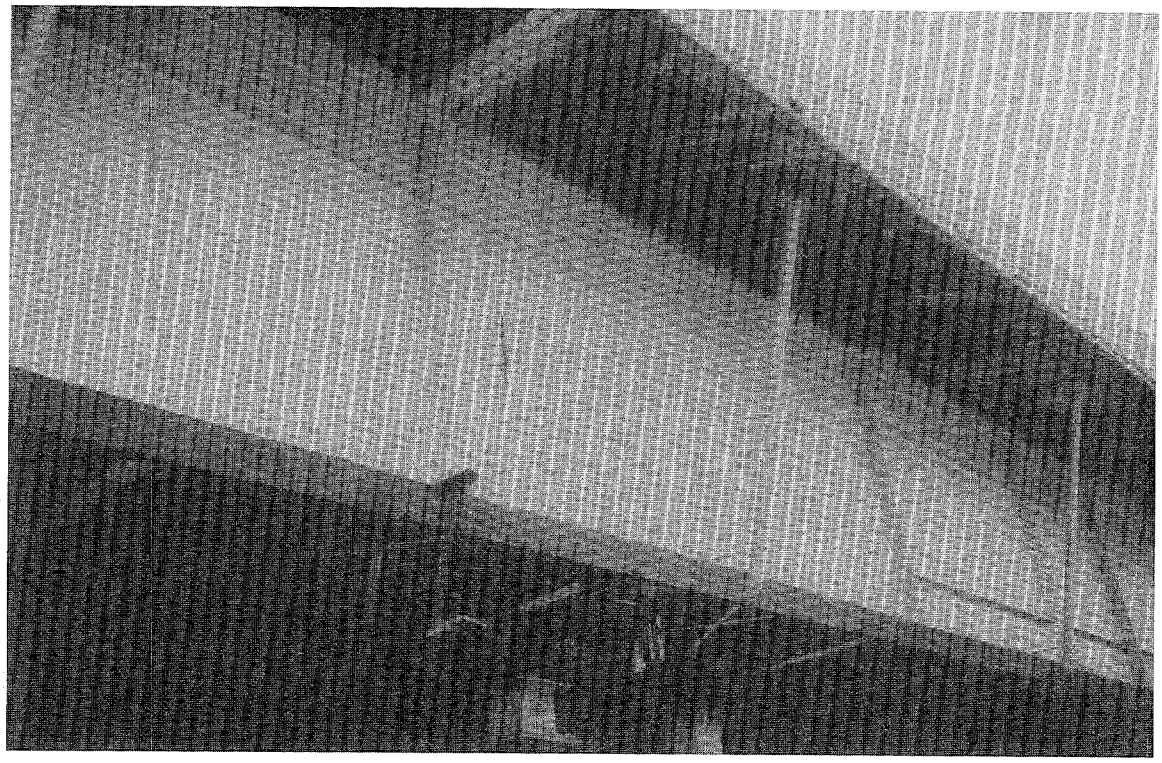

Fig. 17. First stage of damage: two-foot cut at the center of the web.

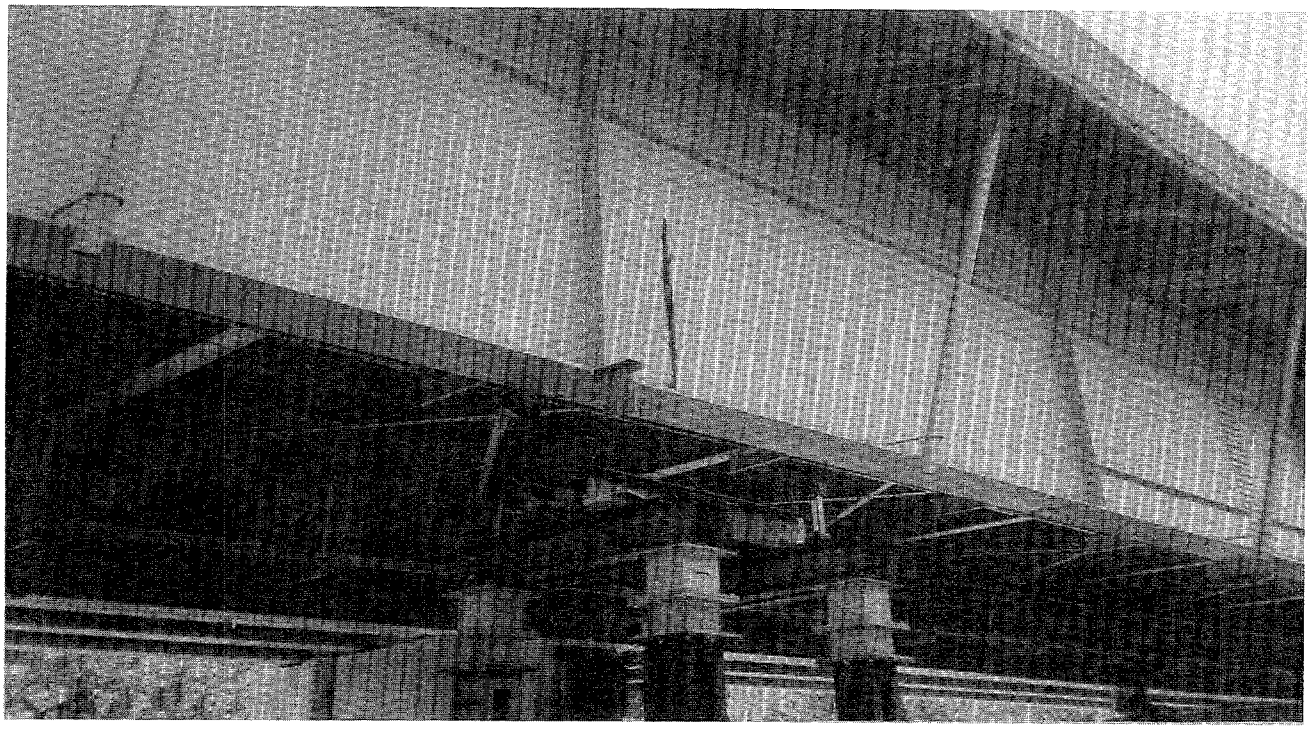

Fig. 18. Second stage of damage: six-footcut from the center of the web to the bottom flange.

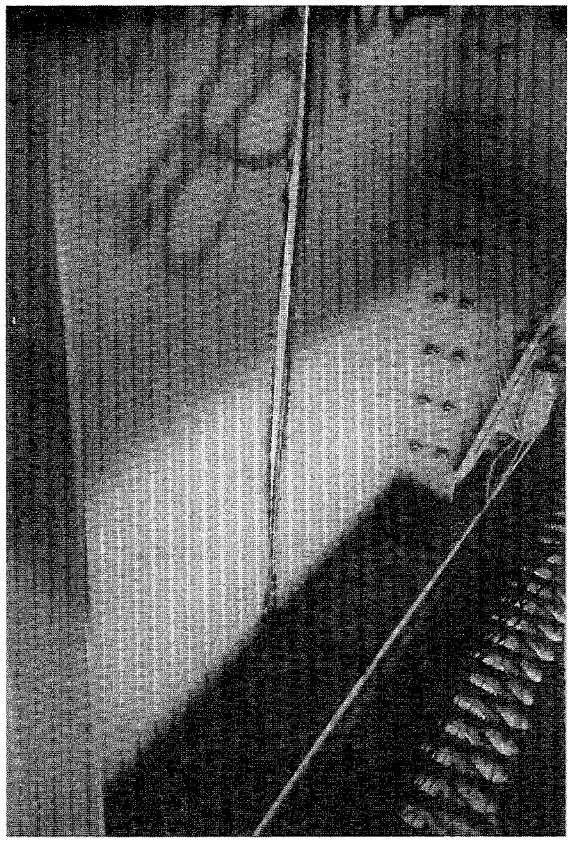

Fig. 19. Third stage of damage: six-foot cut in the web and cuts through half the bottom flange on either side of the web.

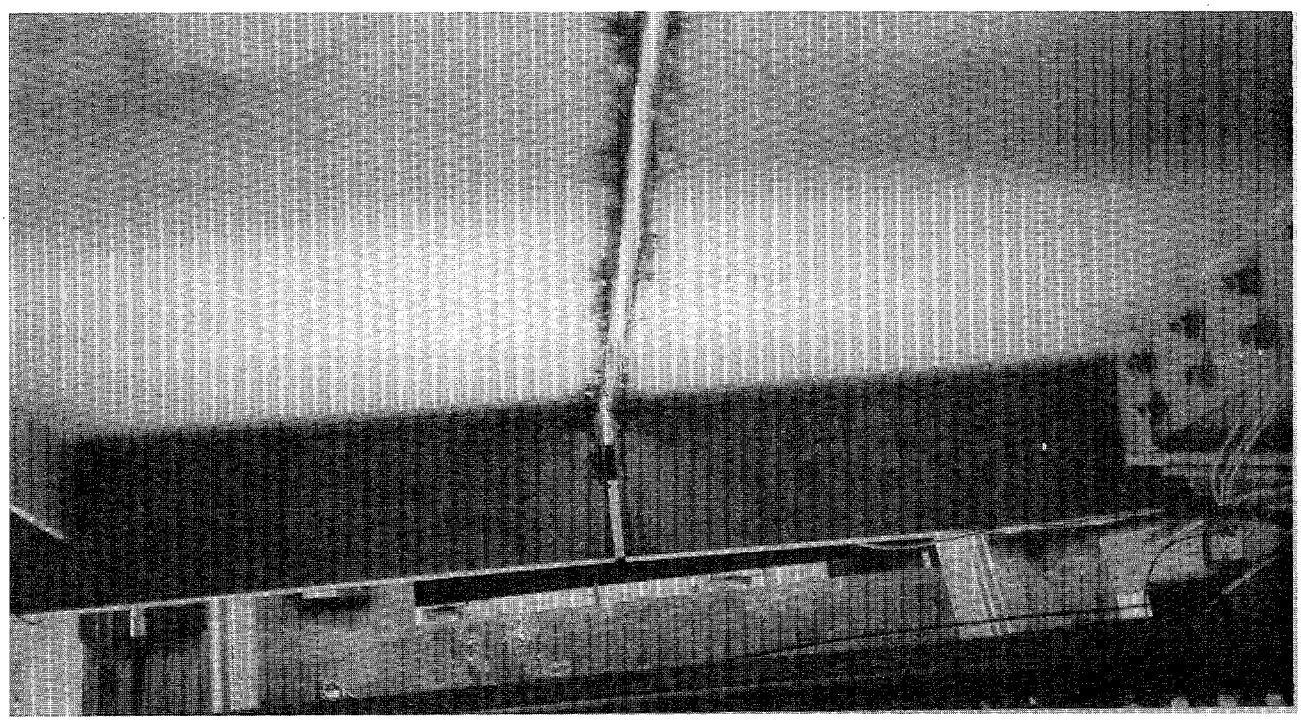

Fig. 20. Fourth stage of damage: six-foot cut in the web and cut through the entire bottom flange.

III. B. 3. b. Results

Experimental modal analyses using both the coarse and refined sets of accelerometers were repeated after each level of damage had been introduced. The experimental procedures and data acquisition equipment used were identical to those used for the undamaged forced vibration tests summarized in Section III. B. 2. Table I summarizes the coarse accelerometer, forced-vibration tests that were performed.

FRF magnitudes for locations S-3 and N-7 are plotted for each level of damaged and compared to the similar FRFs measured on the undamaged structure in Figures 21 and 22, respectively. The figures show that little change in the resonant frequencies and widths of the resonance (damping) occur until the final stage of damage is introduced.

Table II summarizes the resonant frequency and modal damping data obtained during each modal test of the damaged bridge using the coarse set of accelerometers. Also shown in Table II are similar results from the undamaged forced vibration test. No change in the dynamic properties can be observed until the final level of damage is introduced. At the final level, test t22tr, the resonant frequencies for the first two modes have dropped to values 7.6 and 4.4 percent less, respectively, than those measured during the undamaged tests. For modes where the damage was introduced near a node for that mode (Modes 3 and 5) no significant changes in resonant frequencies can be observed.

Mode shape data from the coarse set of accelerometers, corresponding to each level of damage, are summarized in Appendix A, Tables A-7 through A-10. A modal assurance criterion (MAC), sometimes referred to as a modal correlation coefficient (Ewins, 1985) was calculated to quantify the correlation between mode shapes measured during different tests. The MAC makes use of the

TABLE I

Summary of Forced Vibration Tests (Coarse Set of Accelerometers)

Test Designation	Frequency Range (Hz)	No. of Averages	Date/Time	Dynamic Range Accelerometers/ Force Transducer	Damage Description
t16tr	0-12.5	30	Sept. 2, 11:08-11:33 AM	1 Vp, 3.16 Vp	undamaged
t17tr	0-12.5	30	Sept. 2, 2:25-2:40 PM	1 Vp, 3.16 Vp	2-ft cut at the center of the web
t18tr	0-12.5	30	Sept. 3, 12:00-12:46 PM	2 Vp, 6.31 Vp	6-ft cut in the web to the bottom flange
t19tr	0-12.5	30	Sept. 7, 9:32-9:55 AM	2 Vp, 6.31 Vp	bottom 6 ft of the web and half of the flange cut
t22tr	0-12.5	30	Sept. 8, 9:52-10:17 AM	3.98 Vp, 6.31 Vp	bottom 6 ft of the web and entire flange cut

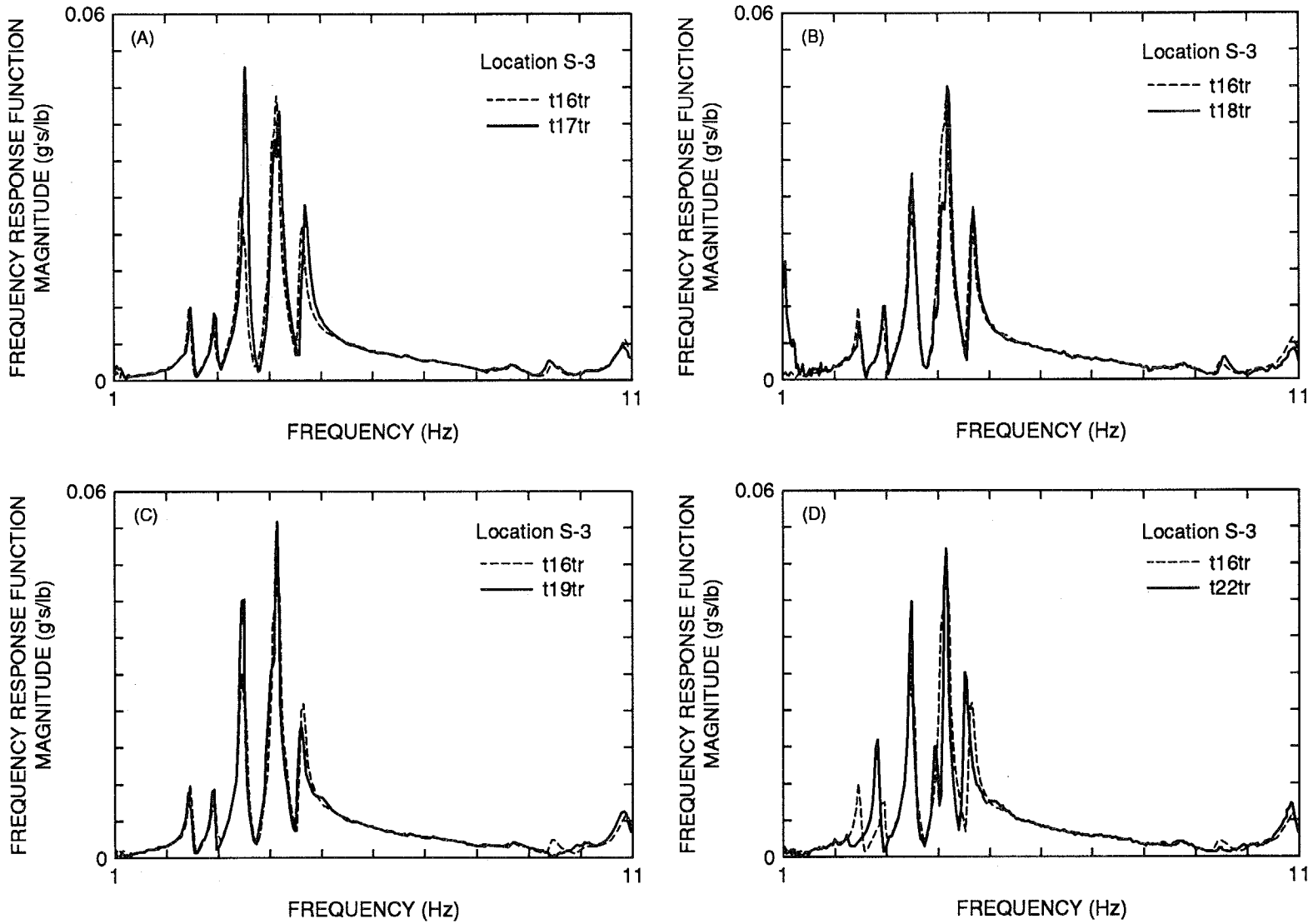

Fig. 21. FRF magnitude measured at location S-3 during each of the damaged forced vibration tests compared with the FRF measured at location S-3 during the undamaged forced vibration test (test t16tr).

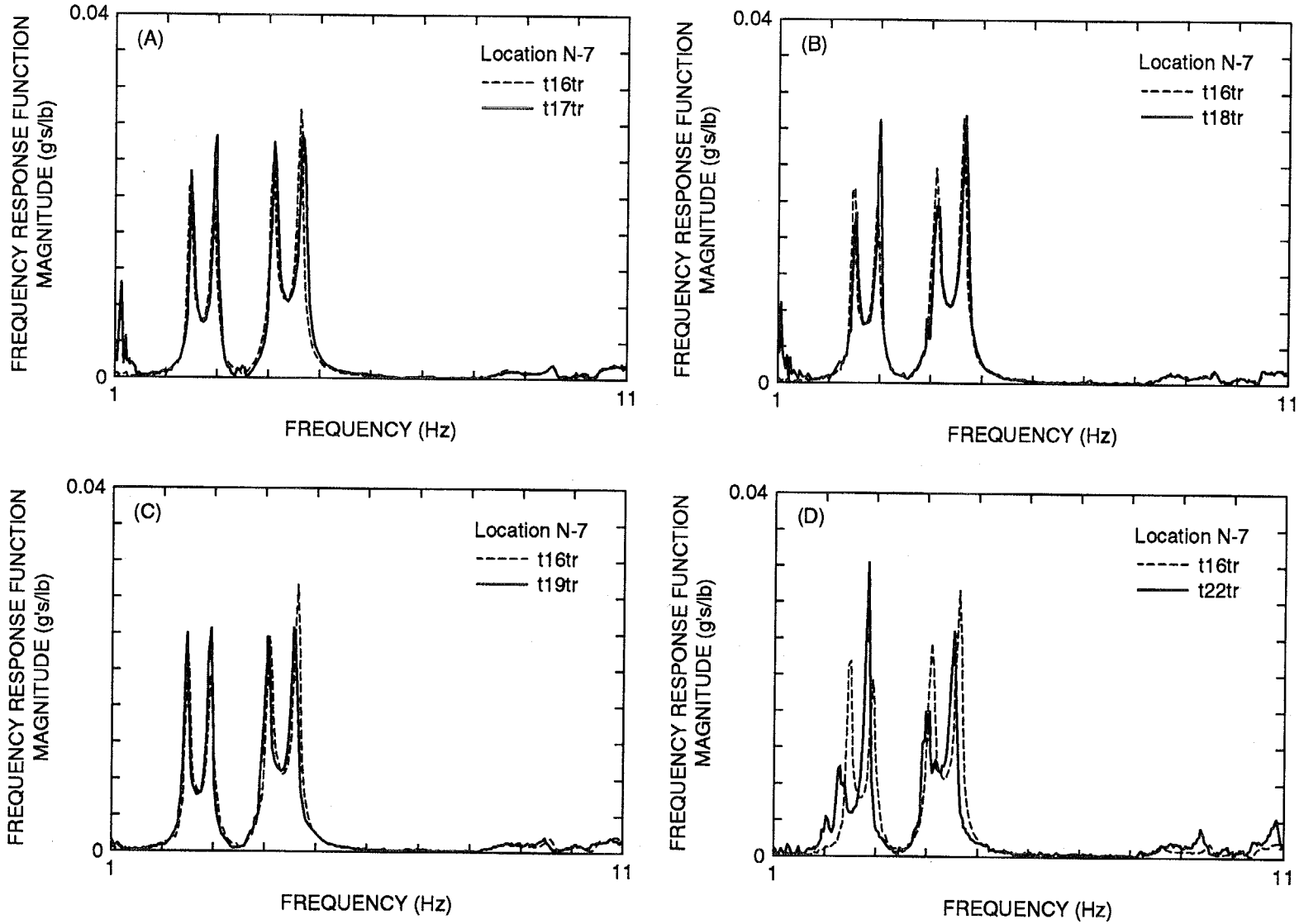

Fig. 22. FRF magnitude measured at location N-7 during each of the damaged forced vibration tests compared with the FRF measured at location N-7 during the undamaged forced vibration test (test t16tr).

TABLE II

Resonant Frequencies and Modal Damping Values Identified from Undamaged and Damaged Forced Vibration Tests Using the Coarse Set of Accelerometers

	Mode 1	Mode 2	Mode 3	Mode 4	Mode 5	Mode 6
Test	Freq. (Hz)/ Damp. (%)	Freq. (Hz)/ Damp. (%)	Freq. (Hz)/ Damp. (%)	Freq. (Hz)/ Damp. (%)	Freq. (Hz)/ Damp. (%)	Freq. (Hz)/ Damp. (%)
t16tr (forced, undamaged)	2.48/ 1.06	2.96/ 1.29	3.50/ 1.52	4.08/ 1.10	4.17/ 0.86	4.63/ 0.92
t17tr (forced, after 1st cut)	2.52/ 1.20	3.00/ 0.80	3.57/ 0.87	4.12/ 1.00	4.21/ 1.04	4.69/ 0.90
t18tr (forced, after 2nd cut)	2.52/ 1.33	2.99/ 0.82	3.52/ 0.95	4.09/ 0.85	4.19/ 0.65	4.66/ 0.84
t19tr (forced, after 3rd cut)	2.46/ 0.82	2.95/ 0.89	3.48/ 0.92	4.04/ 0.81	4.14/ 0.62	4.58/ 1.06
t22tr (forced, after final cut)	2.30/ 1.60	2.84/ 0.66	3.49/ 0.80	3.99/ 0.80	4.15/ 0.71	4.52/ 1.06

orthogonality properties of the mode shapes to compare either two modes from the same test or two modes from different tests. If the modes are identical, a scalar value of one is calculated by the MAC. If the modes are orthogonal and dissimilar, a value of zero is calculated. The MAC that compares mode i and j has the form

$$MAC(i,j) = \frac{\left|\sum_{k=1}^{n}(\phi_j)_k(\phi_i)_k^*\right|^2}{\left(\sum_{k=1}^{n}(\phi_j)_k(\phi_j)_k^*\right)\left(\sum_{k=1}^{n}(\phi_i)_k(\phi_i)_k^*\right)}, \quad (1)$$

where $(\phi)_k$ is an element of the mode-shape vector and the asterisk denotes complex conjugate. The value of the MAC does not actually quantify the correlation between modes. Ewins points out that, in practice, correlated modes will yield a value greater than 0.9, and uncorrelated modes will yield a value less than 0.05. The MAC is not affected by a scalar multiple.

Table III shows the MAC values that are calculated when mode shapes from tests t17tr, t18tr, t19tr, and t22tr are compared to the modes calculated from the undamaged forced vibration test, t16tr. The MAC values show no change in the mode shapes for the first three stages of damage. When the final level of damage is introduced, significant drops in the MAC values for modes 1 and 2 are noticed. These two modes are shown in Figs. 23 and 24 and can be compared to similar modes identified for the undamaged bridge in Figs. 11 and 12. When the modes have a node near the damage location (Modes 3 and 5), no significant reduction in the MAC values are observed, even for the final stage of damage, and a plot of this mode shape from test t22tr, Fig. 25, shows no change from the corresponding undamaged mode, Fig. 13. Examination of mode shapes from tests t17tr, t18tr, and t19tr reveal no change from the undamaged mode shapes shown in Figs. 11 through 16, as would be indicated from the MAC values shown in Table III.

TABLE III

Modal Assurance Criteria: Undamaged and Damaged Forced Vibration Tests (Coarse Set of Accelerometers)

Modal Assurance Criteria		t16tr X t17tr				
Mode	1	2	3	4	5	6
1	0.996	0.006	0.000	0.003	0.001	0.003
2	0.000	0.997	0.000	0.005	0.004	0.003
3	0.000	0.000	0.997	0.003	0.008	0.001
4	0.004	0.003	0.006	0.984	0.026	0.011
5	0.001	0.008	0.003	0.048	0.991	0.001
6	0.001	0.006	0.000	0.005	0.005	0.996

Modal Assurance Criteria		t16tr X t18tr				
Mode	1	2	3	4	5	6
1	0.995	0.004	0.000	0.004	0.001	0.002
2	0.000	0.996	0.000	0.003	0.002	0.002
3	0.000	0.000	0.999	0.006	0.004	0.000
4	0.003	0.006	0.005	0.992	0.032	0.011
5	0.001	0.006	0.008	0.061	0.997	0.004
6	0.002	0.004	0.000	0.005	0.005	0.997

Modal Assurance Criteria		t16tr X t19tr				
Mode	1	2	3	4	5	6
1	0.997	0.002	0.000	0.005	0.001	0.001
2	0.000	0.996	0.001	0.003	0.002	0.002
3	0.000	0.000	0.999	0.006	0.006	0.000
4	0.003	0.005	0.004	0.981	0.032	0.011
5	0.001	0.006	0.004	0.064	0.995	0.003
6	0.002	0.002	0.000	0.004	0.009	0.995

Modal Assurance Criteria		t16tr X t22tr				
Mode	1	2	3	4	5	6
1	0.821	0.168	0.002	0.001	0.000	0.001
2	0.083	0.884	0.001	0.004	0.001	0.002
3	0.000	0.000	0.997	0.005	0.007	0.001
4	0.011	0.022	0.006	0.917	0.010	0.048
5	0.001	0.006	0.003	0.046	0.988	0.002
6	0.005	0.005	0.000	0.004	0.009	0.965

Data from the refined set of accelerometers, similar to that acquired during the undamaged forced vibration tests, were again acquired after each level of damage had been introduced into the plate girder. The resonant frequencies and complex mode shape data corresponding to the different levels of damage obtained with this set of accelerometers are summarized in Appendix A, Tables A-2 through A-5.

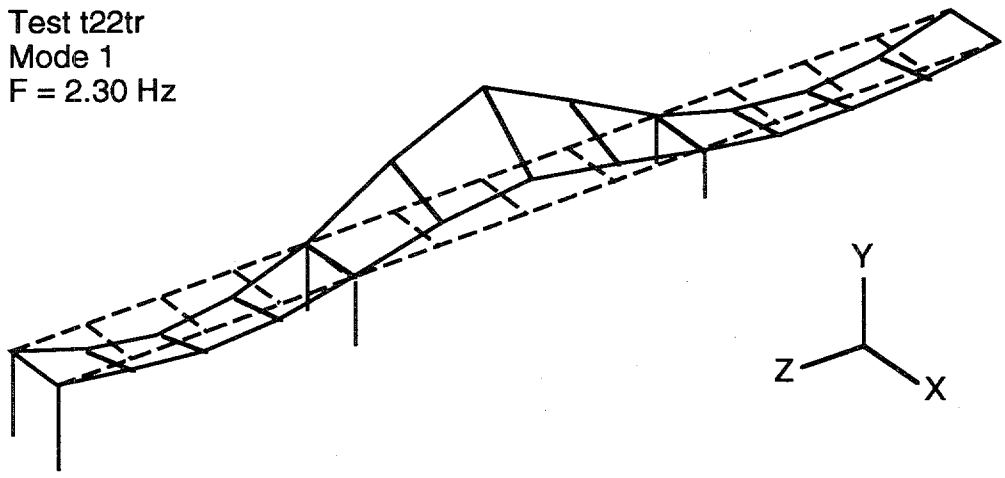

Fig. 23. The first flexural mode measured after the final damage stage, test t22tr.

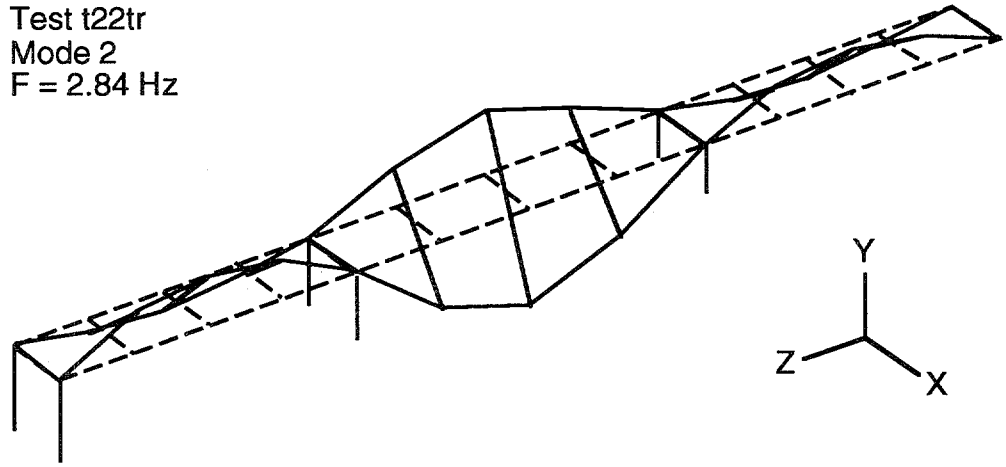

Fig. 24. The first torsional mode measured after the final damage stage, test t22tr.

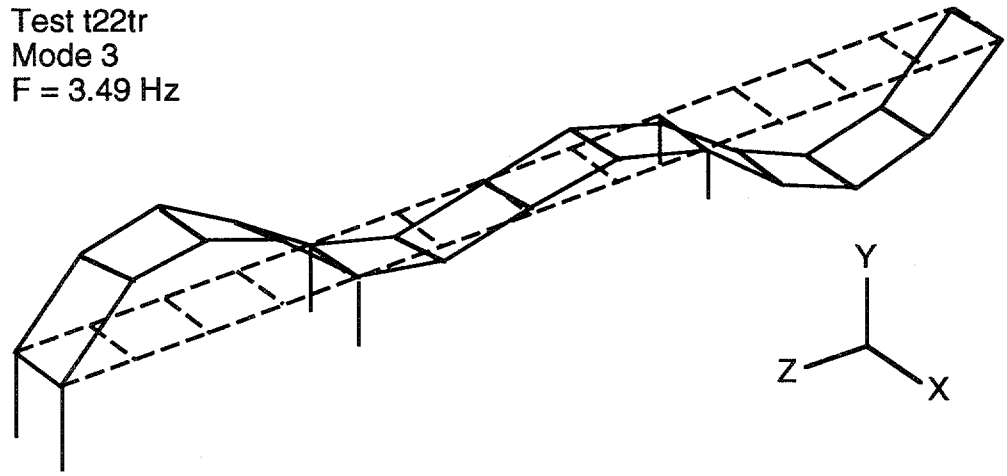

Fig. 25. The second flexural mode measured after the final damage stage, test t22tr.

These test results show that changes in resonant frequencies or mode shapes are not sensitive enough to be a reliable indicator of damage in a bridge structure. It was only after the final level of damage that significant changes in these modal parameters could be observed. From a practical standpoint this would be considered too late for a reliable damage indicator. Even after the final level of damage, modes that have a node close to damage location show almost no change from their corresponding undamaged mode. These results motivate the need for more robust damage indication algorithms.

III. C. Numerically Generated I-40 Bridge Data

Using benchmarked finite element models, forced vibration tests similar to the ones conducted on the I-40 Bridge were simulated numerically. All dynamic analysis calculations were performed with the ABAQUS standard finite element code (ABAQUS/Standard User's Manual (1994)) on a CRAY Y-MP computer. Results of the analyses were post-processed using ABAQUS Post (ABAQUS/Post Manual (1994)), also on the CRAY. Mesh generation was done with PATRAN (P3/PATRAN User Manual (1992)) on a Silicon Graphics workstation. Results from these analyses (node point accelerations) were then analyzed using similar signal processing techniques as those applied to the refined set of accelerometer data. Signal processing tasks were performed using MATLAB standard (MATLAB User's Guide and Reference Guide (1992)) and the signal processing toolbox (MATLAB Signal Processing Toolbox (1992)).

III. C. 1. Finite Element Modeling of the I-40 Bridge

The finite element model of the bridge superstructure included a total of 1235 nodes and 548 elements (see Fig. 26). With this mesh configuration the bridge model had 7032 degrees of freedom. Eight-node shell elements were chosen to model the web of the two girders and the bridge deck. Three-node beam elements were used to model the girder flanges, the floor beams, and the stringers. Detailing of the bridge model at the abutment end is also shown on Fig. 26. Horizontal and vertical stiffeners on the plate girder, the diagonal bracing, and the concrete reinforcement were not included in this model. Previous studies (Farrar, et al. 1996) where the individual stiffeners were modeled (35,160 DOF model) showed no significant variation in the global dynamic properties from the model used in this study. Table IV compares the resonant frequencies and modal mass of the two models.

Generic material properties for steel were specified as

$E_{steel} = 29{,}000{,}000$ psi,

$\nu_{steel} = 0.3$, and

$\mu_{steel} = 0.284$ lbm / in^3.

Generic concrete properties were specified as

$E_{concrete} = 57000\sqrt{f_c'} = 3{,}600{,}000$ psi where $f_c' = 4000$ psi,

$\nu_{concrete} = 0.2$, and

$\mu_{concrete} = 145$ lbm / ft^3.

For both the shell and beam elements, all six degrees of freedom are active which allows a complete three-dimensional representation of the bridge. Boundary conditions are enforced at the support locations shown on Fig. 26 where the bridge is supported by the concrete piers. Note that when defining the boundary conditions, no attempt was made to model the piers. Instead, at all support locations, translation in the three global directions X, Y, and Z is constrained. Although

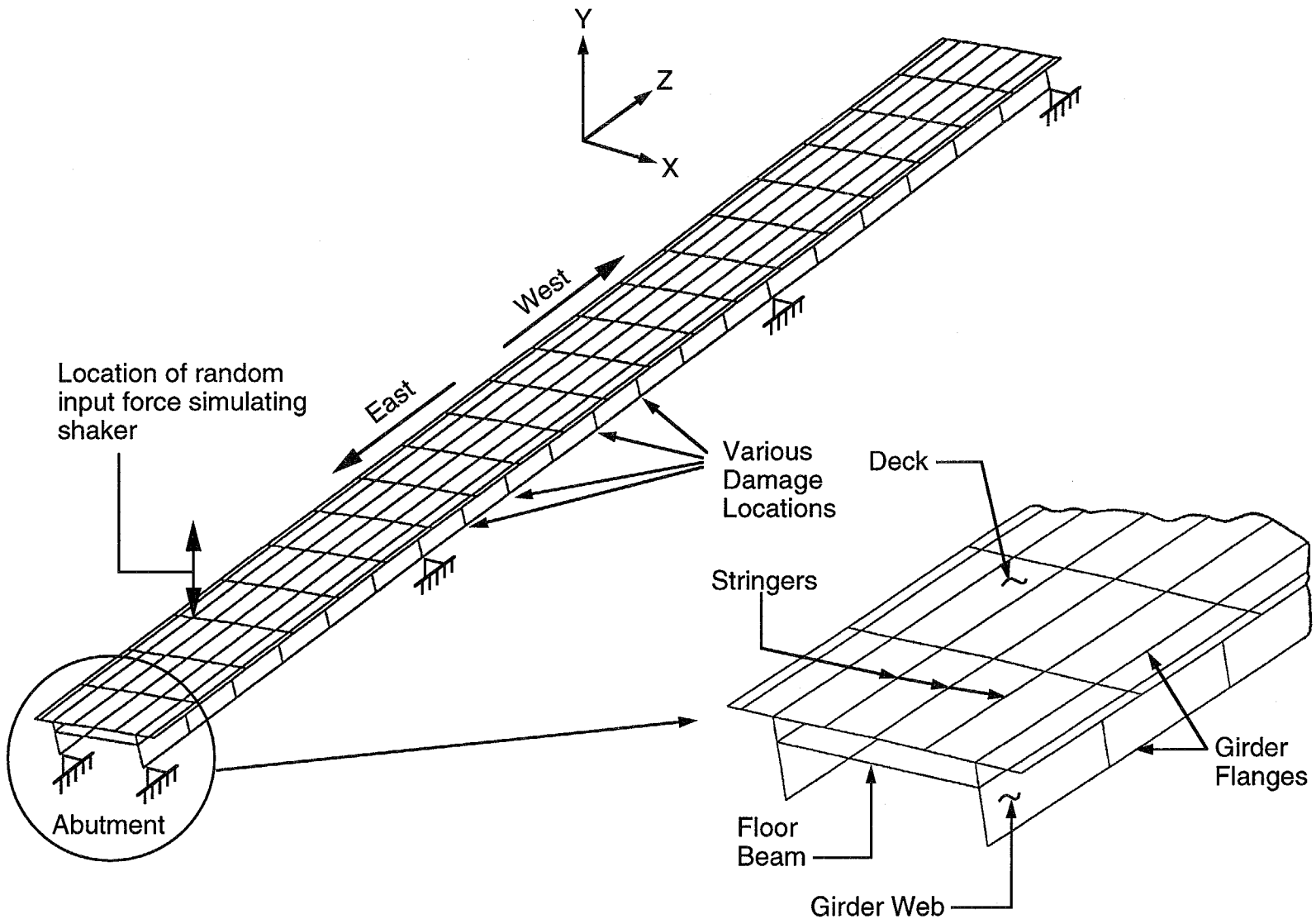

Fig. 26. Finite element discretization of the three-span unit of the I-40 Bridge, neglecting the piers.

TABLE IV

Comparison of Dynamic Properties Identified by the 7,032 DOF Model with the Dynamic Properties Identified by the 35,160 DOF Model

Mode	35,160 DOF Model		7,032 DOF Model	
	Frequency (Hz)	Generalized Mass	Frequency (Hz)	Generalized Mass
1	2.82	1828	2.81	1784
2	3.77	1277	3.78	1225
3	3.81	988.2	3.79	963.7
4	3.88	584.4	3.87	562.0
5	5.11	1578	5.09	1484
6	5.23	1551	5.20	1473
7	5.48	756.4	5.39	738.6

the piers must be modeled to accurately simulate the dynamic response of the I-40 Bridge, for the purpose of comparing different damage identification methods, they can be neglected, thus reducing the required computational time. To further simulate the actual support at the base of the plate girders above the piers, the out-of-plane rotations (about the Y and Z axes shown in Fig. 26) are also constrained at these locations.

For the I-40 Bridge tests, a 2000 lb peak amplitude random excitation was applied by the Sandia shaker. Using an "in-house" FORTRAN program, a random signal was generated to simulate the input force applied by the Sandia shaker during the actual experimental modal testing of the I-40 Bridge. The signal was specified so that it would have a uniform power spectral density (PSD) in the range of 2 to 12 Hz and a peak amplitude of 2000 lb. The random signal defined by 1024 data points at 0.025-s increments. Plots of the generated random signal along with its PSD are provided in Figs. 27 and 28, respectively.

As shown in Figs. 27 and 28, the duration of load is 25.6 seconds. The Nyquist frequency for the signal is 20 Hz. This generated random force is applied to the model as a time-varying concentrated vertical load at a nodal point that approximates the position of the Sandia shaker during the forced vibration tests. The random force was applied on the concrete deck directly above the south girder at the midpoint of the east span as shown in Fig. 26.

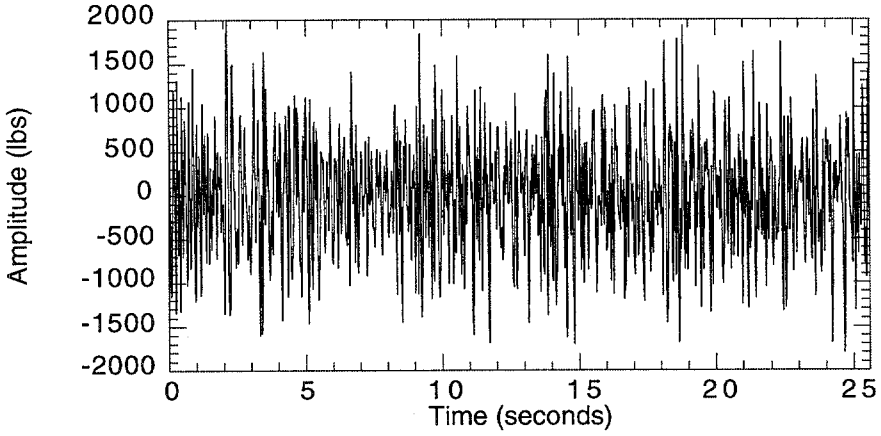

Fig. 27. Generated random signal representing the input force applied by the Sandia shaker.

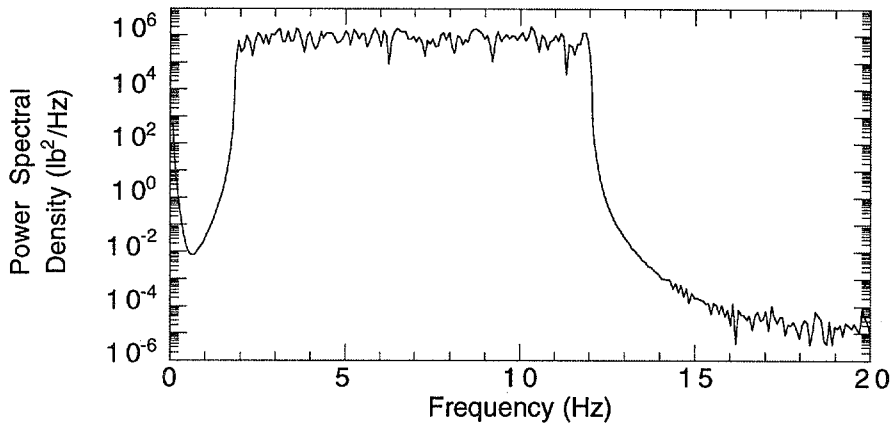

Fig. 28. Power spectral density of the random input force in the frequency range of 0 to 20 Hz.

The discretization used in the finite element model did not have node points corresponding to the actual 11 measurement locations associated with the refined set of accelerometers (Fig. 9). Instead, nine equally spaced nodal points were monitored to simulate the accelerometer locations. Figure 29 shows an enlarged view of the bridge central span highlighting these locations. The accelerometers are spaced longitudinally at equal distances of approximately 20 feet, which, incidentally, are locations where the floor beams frame into the main girder. In the vertical direction, the monitored nodes are located approximately one-third the girder height above the bottom flange.

III. C. 2. Simulation of Damage to the I-40 Bridge

As shown in Fig. 30, three levels of damage similar to the final three girder cuts imposed during the I-40 Bridge tests were simulated by creating additional nodes at the vicinity of the crack and redefining the finite element discretization of the plate girder web and bottom flange in this region.

The second level of damage was simulated by disconnecting the shell elements representing the lower one-third of the web and allowing the bottom flange to remain connected using a new beam element. For the third phase of damage, the new beam element directly below the termination of the web cut is altered to one-half its original cross-sectional area. Finally, the new bottom flange element connecting the two damaged portions of the girder is removed to simulate the final damage condition. This method of modeling the damage changes the geometry only, and does not introduce nonlinearities into the model. Therefore, a linear modal analysis can be performed to ascertain the effects of this damage on the dynamic properties of the structure. A summary of the simulated damage conditions at the bridge midspan is provided in Table V.

As a supplement to the damage simulation at the girder midspan, other damage scenarios were modeled to evaluate the dynamic response of the bridge with damage at different locations. These analyses along with those conducted with damage at midspan would provide a data base of results for the damage detection routines. Five damage scenarios were modeled at different locations on the north girder in the central span.

1. One main girder cut simulating the final level of damage positioned halfway between midspan and the east interior support.
2. One main girder cut simulating the final level of damage positioned one floor-beam-panel away from the east interior support.

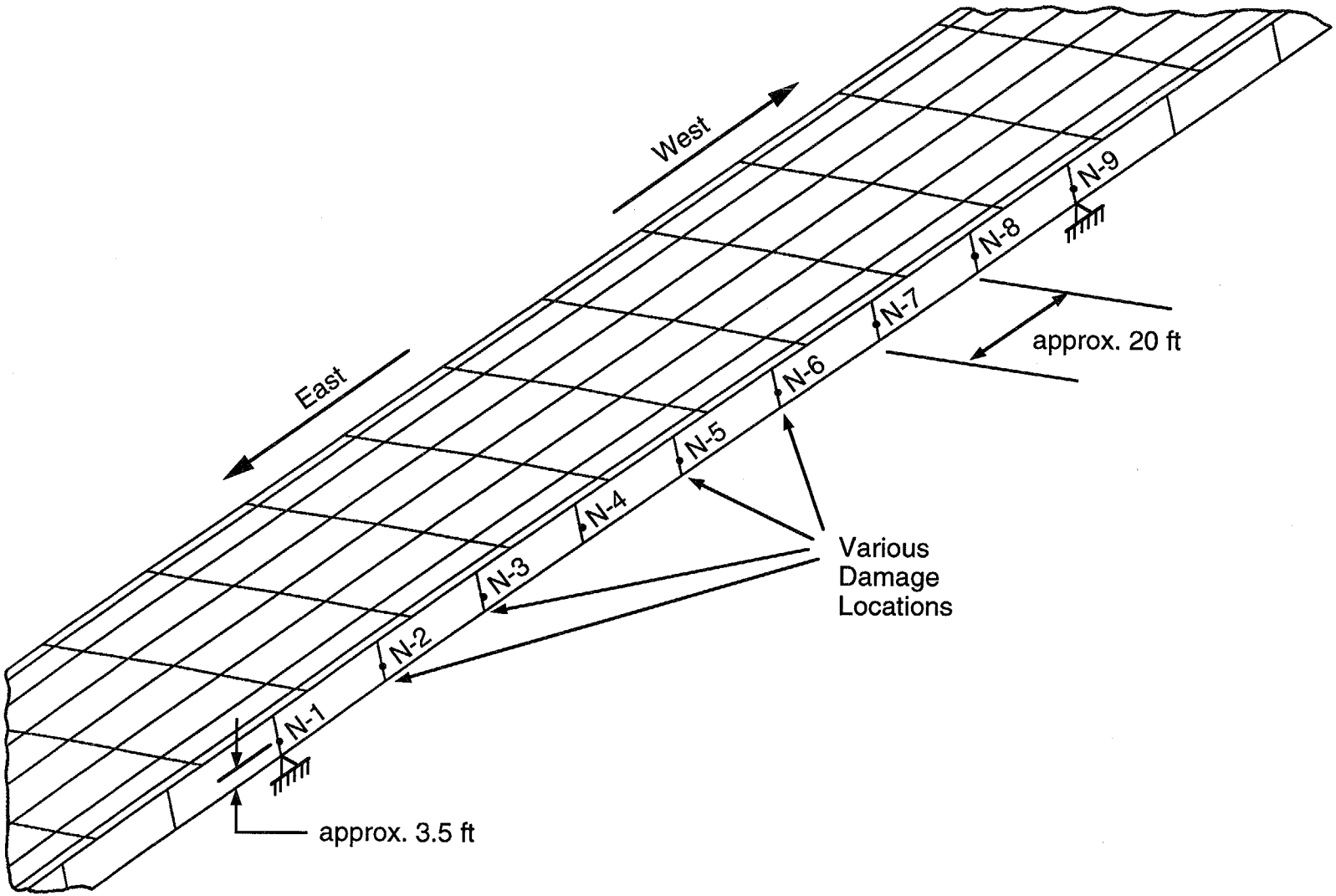

Fig. 29. Enlarged view of the central span of the I-40 Bridge showing the simulated accelerometer locations N-1 through N-9.

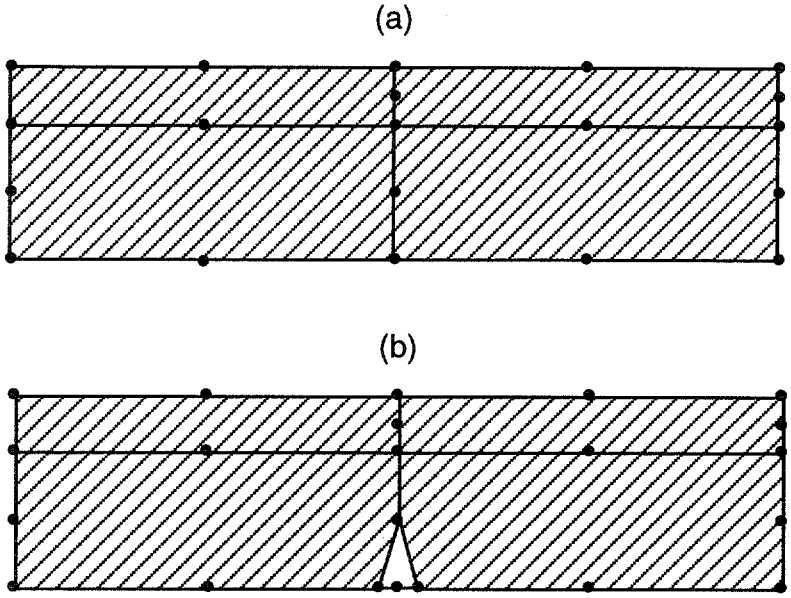

Fig. 30. Finite element modeling of the main girder (a) before damage and (b) after damage.

3. Two main girder cuts, each simulating the final level of damage, positioned two floor-beam-panels away from the east interior support and three floor-beam-panels away from the west interior support.
4. One main girder cut simulating the second level of damage positioned halfway between midspan and the east interior support.
5. One main girder cut simulating the second level of damage positioned one floor-beam-panel away from the east interior support.

Damage cases A-4 through A-8 correspond to the damage scenarios 1 through 5, respectively, listed above. A summary of the additional damage cases is provided in Table VI.

The final case (A-9) did not involve altering the finite element model. Instead, the original forcing function is replaced with a different time-history that had the same peak amplitude and the same frequency content. Plots of the force time history and the PSD of the alternate random force, respectively, are given in Figs. 31 and 32.

Note that although the force time histories differ between the alternate and original random force, their frequency contents remain similar. This case was included in the investigation to test that the damage identification routines do not identify damage when two different undamaged responses are analyzed, that is, give a "false-positive" reading.

TABLE V

Summary of Damage Cases A-1 through A-3

Damage Case	Location of Damage	Damage Description
A-1	midspan	lower one-third portion of web cut
A-2	midspan	lower one-third portion of web plus half of bottom flange cut
A-3	midspan	lower one-third portion of web plus entire bottom flange cut

TABLE VI Summary of Damage Cases A-4 through A-8		
Damage Case	Location of Damage on Damaged Span	Damage Description
A-4	one location: halfway between midspan and east support	lower one-third portion of web plus entire bottom flange cut
A-5	one location: one floor-beam-panel away from east support	lower one-third portion of web plus entire bottom flange cut
A-6	two locations: halfway between midspan and east support; one floor-beam-panel west of midspan	lower one-third portion of web plus entire bottom flange cut
A-7	one location: halfway between midspan and east support	lower one-third portion of web cut
A-8	one location: one floor-beam-panel away from east support	lower one-third portion of web cut

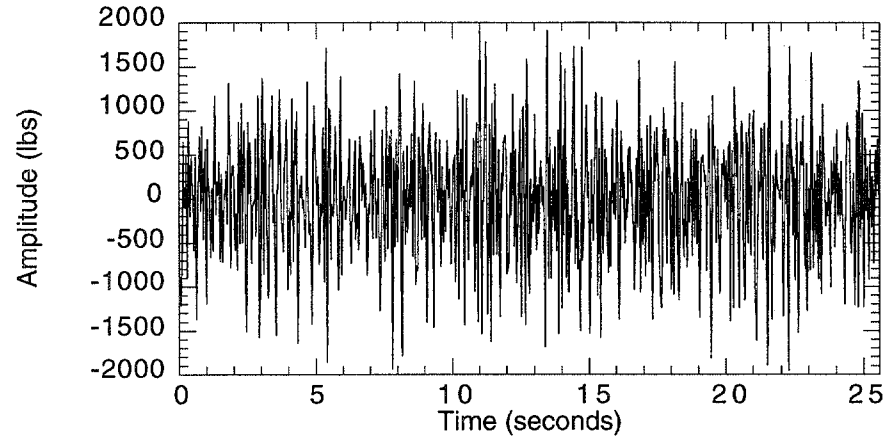

Fig. 31. Generated random signal representing the alternate input force.

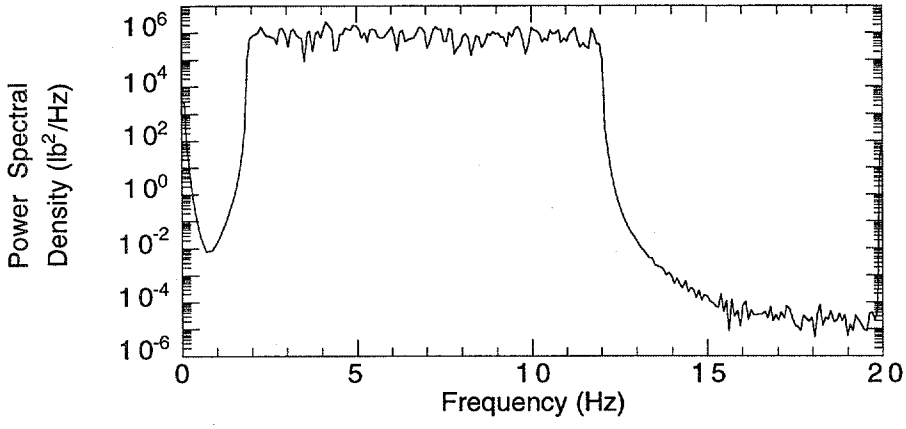

Fig. 32. Power spectral density of the alternate input force in the frequency range of 0 to 20 Hz.

III. C. 3. Eigenvalue and Forced Vibration Analyses

Before conducting the forced vibration dynamic analyses of the I-40 Bridge, eigenvalue analyses were performed to identify the resonant frequencies of the three modes of the bridge. An analysis was first conducted with the bridge in an undamaged condition and then repeated for each state of damage (cases A-1 through A-8) to determine the changes, if any, in the resonant frequencies that resulted from the damage.

Figure 33 shows the first bending, first torsion, and second bending modes identified from the eigenvalue analysis of the undamaged bridge. The same three modes identified for damage case A-3 are shown in Fig. 34. When this level of damage is introduced, there is a decrease in the resonant frequency of the first mode (approximately 4.2%) along with a 0.78% reduction for the second mode frequency. No changes were detected in the third mode frequency after damage case A-3 was introduced. This response was expected because one of the nodes for the third mode coincided with the damage location. Table VII summarizes the changes in resonant frequencies for the first three modes that resulted from the various damage scenarios.

The mode shapes and resonant frequencies of the bridge for damage cases A-4 through A-6 are shown in Figs. 35 through 37. No significant changes were observed for damage scenario A-4. The bridge behavior for the A-5 and A-6 damage conditions followed a similar trend to that shown when the damage was located at midspan (case A-3). For the first mode, the resonant frequency decreased by 4.2% and 2.6% for damage scenarios A-5 and A-6, respectively. No significant changes in the frequencies were detected for the first torsional and second bending modes.

Using the random force input shown in Fig. 27, a dynamic time history analysis was conducted using modal superposition and the responses (i.e., vertical acceleration-time histories) at the nine monitored nodal points are recorded. A typical response at locations N-1 and N-5, identified in Fig. 29, are shown in Figs. 38 and 39, respectively.

TABLE VII

Resonant Frequencies Calculated by Finite Element Analyses of the Various Damage Scenarios

Damage Case	First Bending Mode Freq. (Hz)[1]	First Torsional Mode Freq. (Hz)[1]	Second Bending Mode Freq. (Hz)[1]
Undamaged	3.79	3.87	5.09
A-1	3.79 (0.0%)	3.87 (0.0%)	5.09 (0.0%)
A-2	3.79 (0.0%)	3.87 (0.0%)	5.09 (0.0%)
A-3	3.63 (4.2%)	3.84 (0.8%)	5.09 (0.0%)
A-4	3.79 (0.0%)	3.87 (0.0%)	5.07 (0.4%)
A-5	3.63 (4.2%)	3.85 (0.5%)	5.07 (0.4%)
A-6	3.69 (2.6%)	3.85 (0.5%)	5.07 (0.4%)
A-7	3.79 (0.0%)	3.87 (0.0%)	5.09 (0.0%)
A-8	3.79 (0.0%)	3.87 (0.0%)	5.09 (0.0%)

[1]Values in parentheses are the percent change from the undamaged case

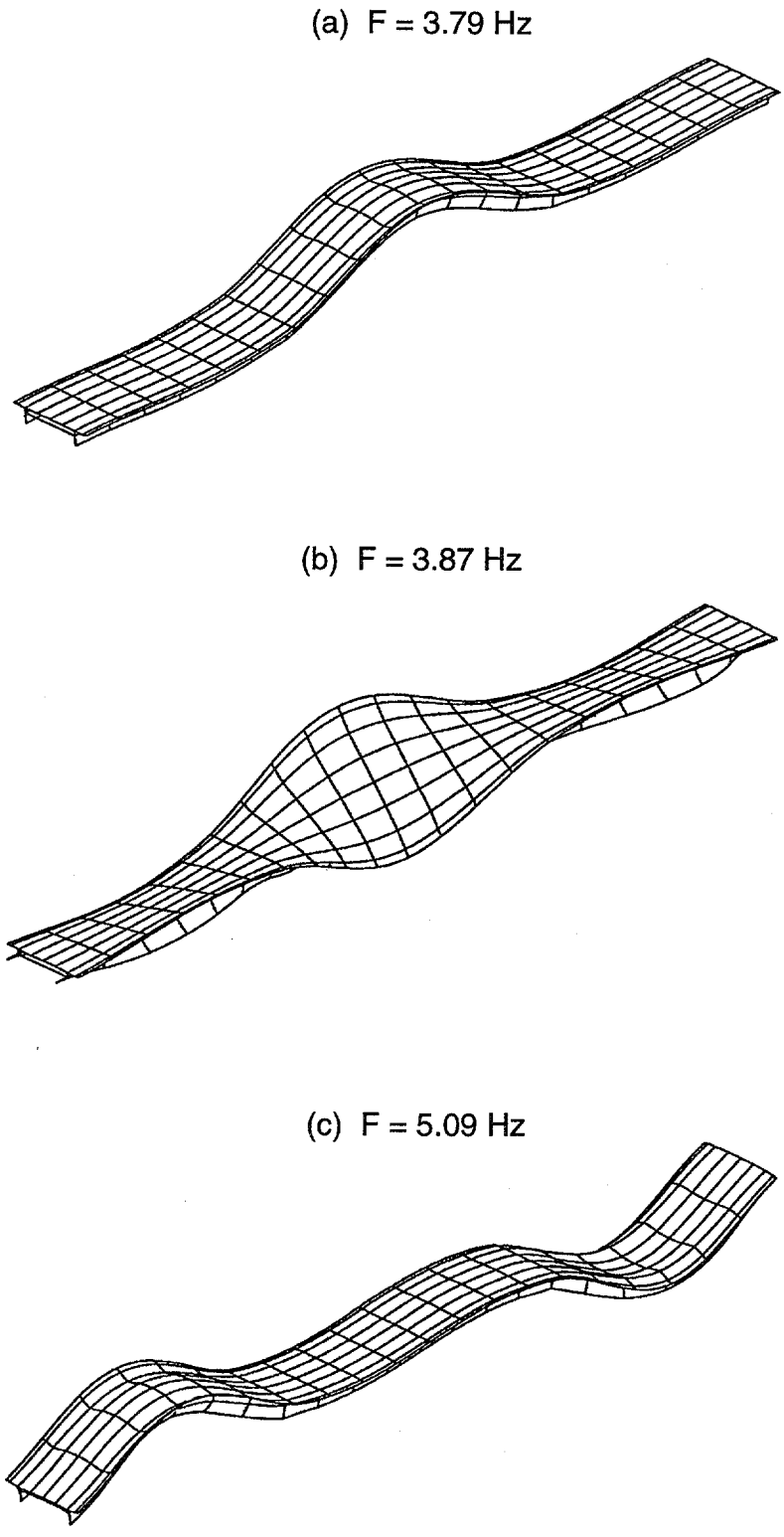

Fig. 33. Modes and resonant frequencies identified from eigenvalue analysis of the undamaged bridge: (a) first bending mode, (b) first torsional mode, and (c) second bending mode.

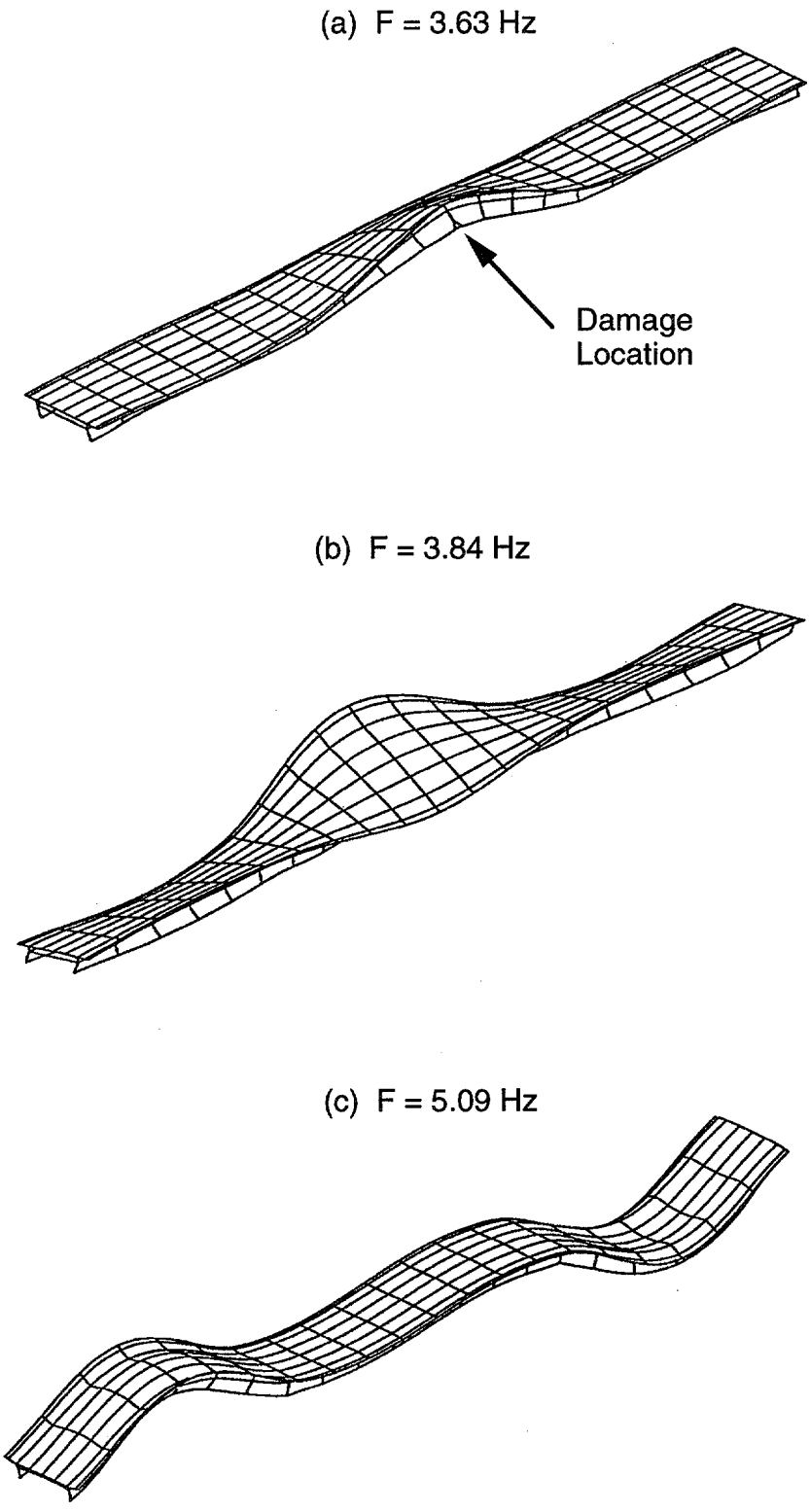

Fig. 34. Modes and resonant frequencies identified from eigenvalue analysis of the damaged bridge, case A-3: (a) first bending mode, (b) first torsional mode, and (c) second bending mode.

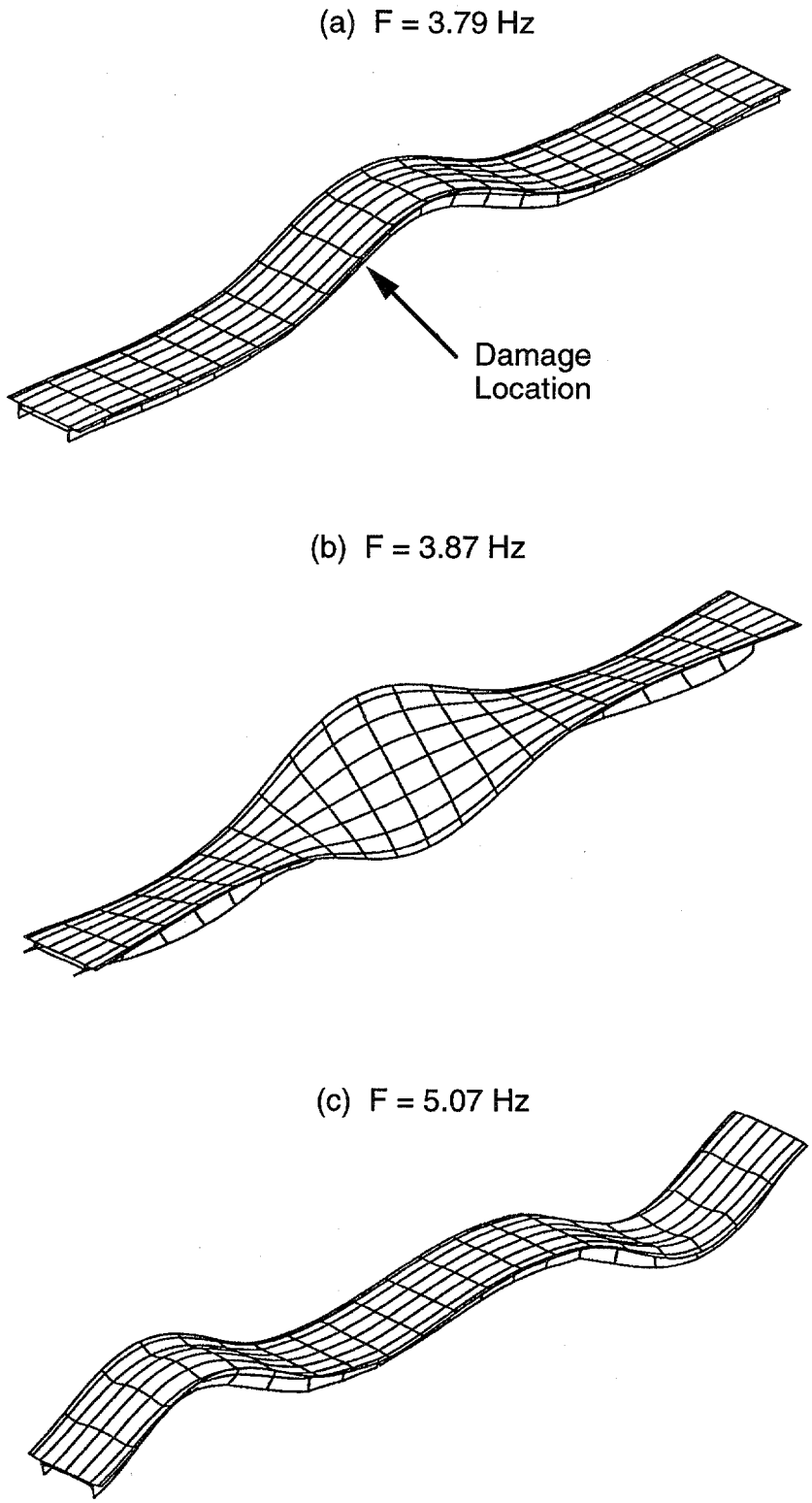

Fig. 35. Modes and resonant frequencies identified from eigenvalue analysis of the damaged bridge, case A-4: (a) first bending mode, (b) first torsional mode, and (c) second bending mode.

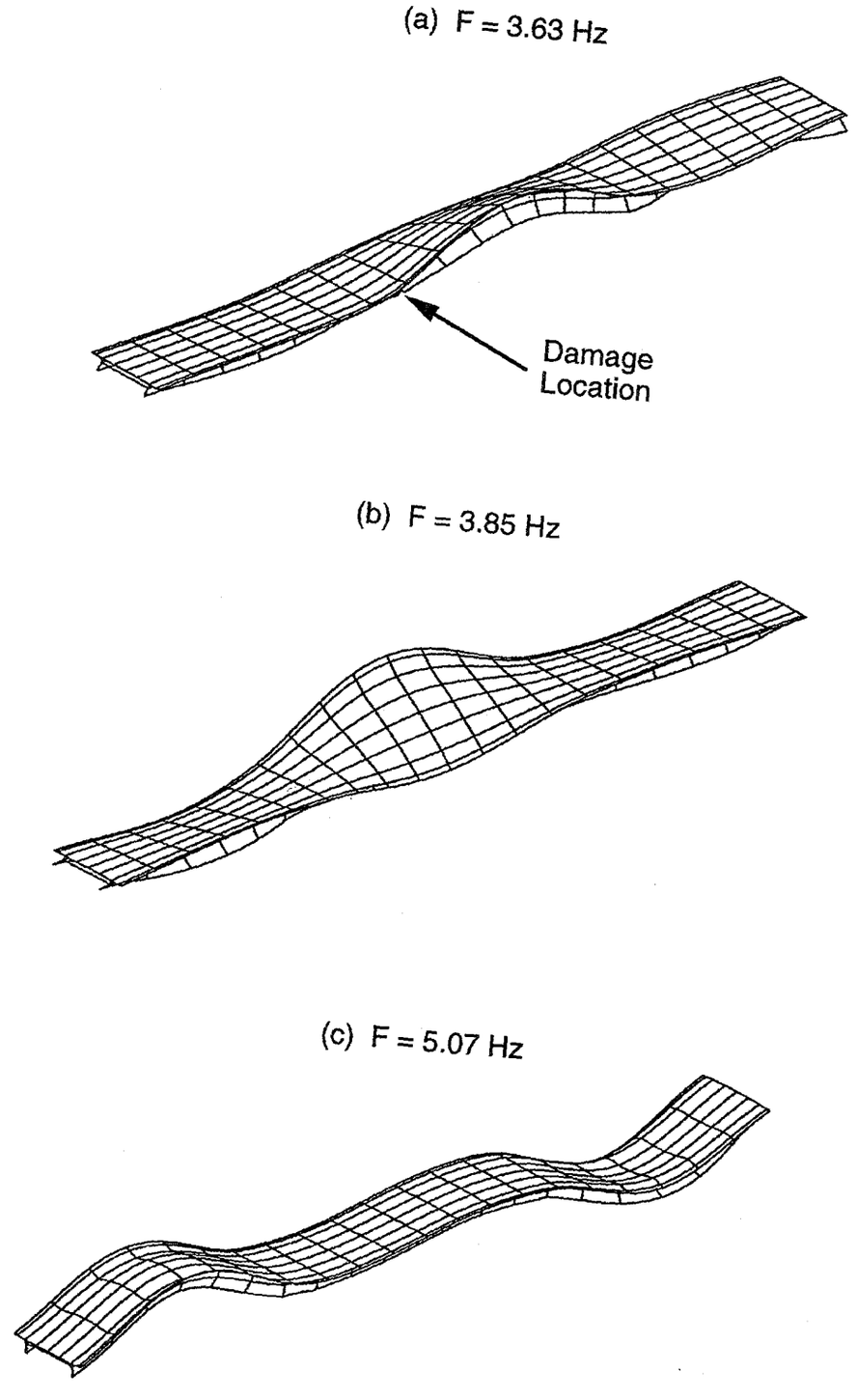

Fig. 36. Modes and resonant frequencies identified from eigenvalue analysis of the damaged bridge, case A-5: (a) first bending mode, (b) first torsional mode, and (c) second bending mode.

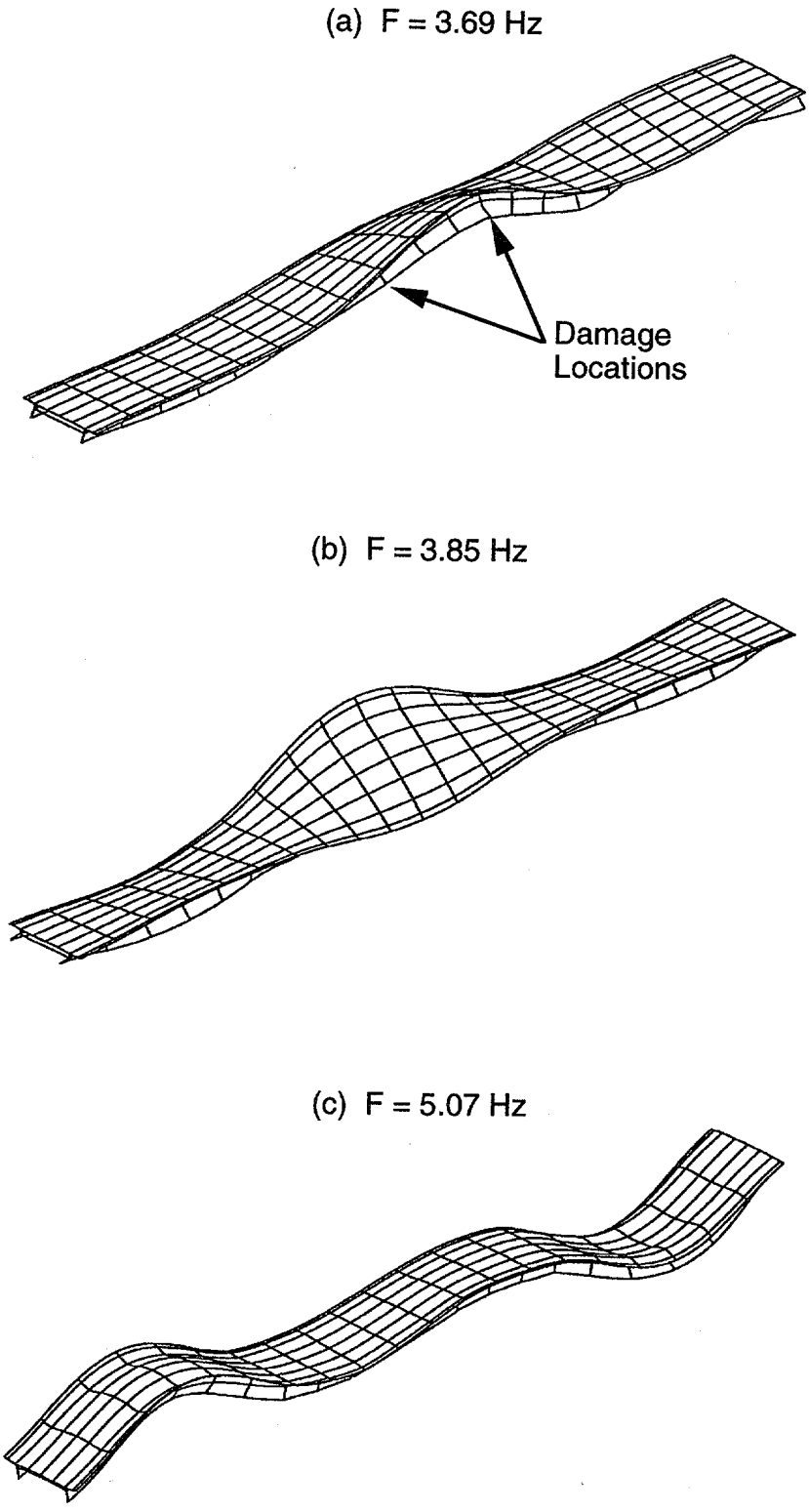

Fig. 37. Modes and resonant frequencies identified from eigenvalue analysis of the damaged bridge, case A-6: (a) first bending mode, (b) first torsional mode, and (c) second bending mode.

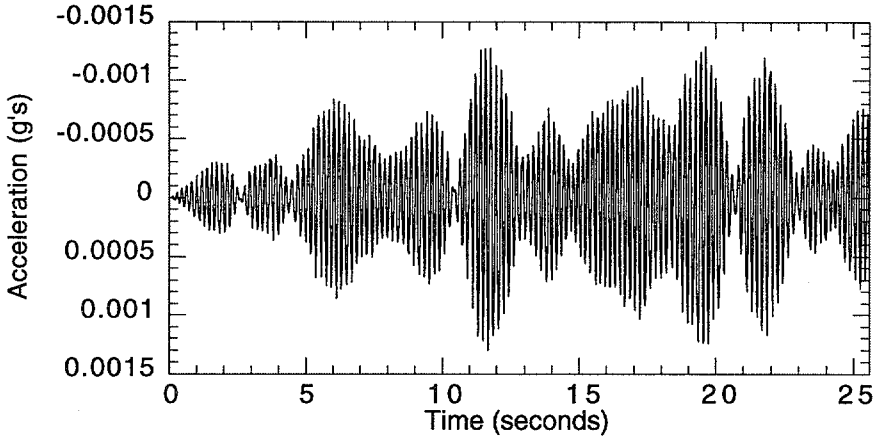

Fig. 38. Typical acceleration time history response at location N-1 for the undamaged bridge.

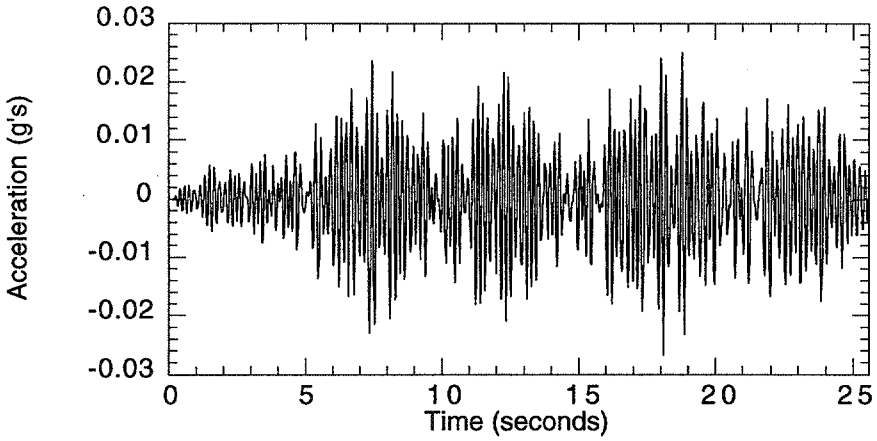

Fig. 39. Typical acceleration time history response at location N-5 for the undamaged bridge.

The modal superposition method provides an efficient way for conducting a time history dynamic analysis with ABAQUS. When implementing this technique it is assumed that the structure is linear and that a sufficient number of modes have been extracted to accurately model the structure's dynamic response. The first ten modes were used in this analysis.

A forced vibration dynamic analysis was initially done with the bridge in its undamaged state and then repeated for each damaged case A-1 through A-8 and the second undamaged case, case A-9. Results from these analyses (i.e., monitored acceleration responses) were then imported to MATLAB for further investigation as discussed in the next section.

III. C. 4. Modal Data from Finite Element Models

Following the eigenvalue and forced vibration dynamic analyses, a spectral analysis was conducted using the nine measured responses shown in Fig. 29. MATLAB performs spectral analysis on time series employing the Welch method of power spectrum estimation. Given two arbitrary 1024 point sequences, MATLAB first divides each sequence into N segments of n samples each, where n must be a power of 2. Two segments of 512 samples were considered sufficient for obtaining accurate results. After the sequence is divided, a Hanning window is applied to each 512-point data segment and the segment is transformed into the frequency domain with a 512-point fast-Fourier transform. The results are then averaged and used to compute individual PSDs and the

cross-power spectral densities (CPSD) between the two series. Processing the calculated response time histories in this manner simulates the signal processing approach that would be employed to compute modal properties from ambient vibration data.

Sampling parameters were specified that calculated the CPSD from 25.6-s time windows discretized with 1024 samples. With a resolution of 0.0391 Hz, the CPSD was calculated for a frequency range of 0 - 20 Hz. Complex mode shapes are determined from the magnitude and phase of the CPS between the nine channels, N-1 through N-9, relative to the reference response N-3 (see Fig. 29). The amplitude of a mode shape is determined from the magnitude of the CPSD at the mode's associated resonant frequency. Note that the modal amplitude for a particular mode at the reference location N-3 is obtained from its PSD. Because no damping was specified in these analyses, phase angles at resonance are either 0 or 180 degrees and the phase information has been incorporated by specifying each amplitude as either a positive or negative value. Figure 40 shows a typical CPSD between channel N-5 relative to channel N-3. The PSD at channel N-3 for the undamaged structure is given in Fig. 41.

The resonant frequencies and mode shape data obtained from the set of monitored responses for the first bending, first torsion, and second bending modes of the undamaged bridge are tabulated in Appendix B. Modal data corresponding to damage cases A-1 through A-9 are also tabulated in the Appendix B.

Before analyzing the modal data with the various damage identification routines, the mode shape data corresponding to the refined set of accelerometers (either experimental or analytical), which are summarized in Appendices A and B, were first normalized assuming an identity mass matrix. There are several approaches in which to normalize the mode shape data. For this problem, the approach taken was to normalize the modal amplitudes to satisfy the condition

$$\{\phi_n\}^T[m]\{\phi_n\} = 1, \tag{2}$$

where $\{\phi_n\}$ = the normalized modal vectors, and
[m] = the mass matrix = diag (1).

Letting ψ_n represent the original modal amplitudes gathered experimentally or analytically, the normalized magnitudes are computed using the equation

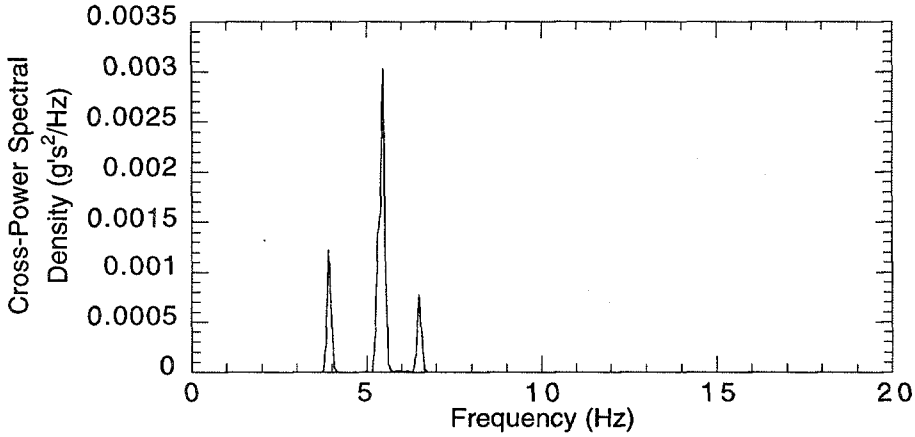

Fig. 40. Cross power spectral density between channels N-5 and N-3 with the bridge undamaged.

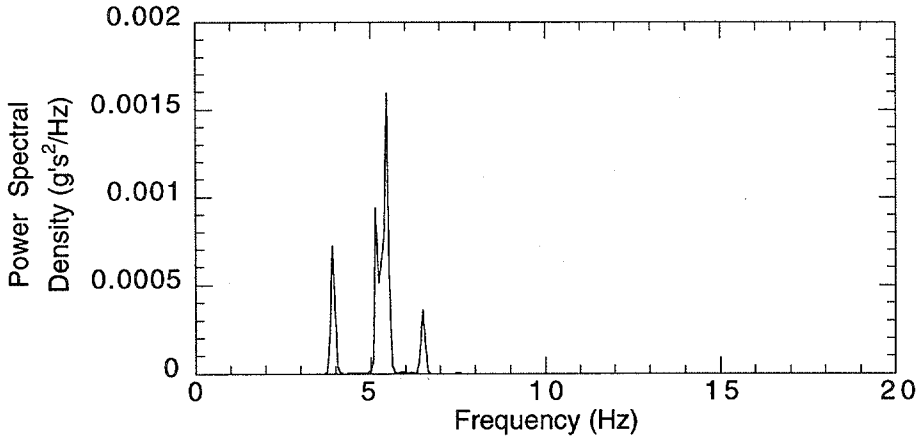

Fig. 41. Power spectral density at reference channel N-3 with the bridge in its undamaged state.

$$\{\phi_n\} = \frac{1}{\sqrt{M_n}}\{\psi_n\}, \tag{3}$$

$$\text{where } M_n = \sum_{i=1}^{p} \psi_{in}^2 m_i. \tag{4}$$

In the latter equation, p = the number of measured points, n = the mode shape number.

IV. DESCRIPTION OF DAMAGE IDENTIFICATION METHODS

In this section the damage identification methods that were compared are described. In the form reported herein these methods provide a Level two assessment of damage, that is, they identify that the structures are damaged and they estimate the location of damage. A more detailed description of these damage identification methods can be found in the cited references for each method.

IV. A. Damage Index Method

This section presents the damage identification method developed by Stubbs and Kim that locates damage in structures given their characteristic mode shapes measured before and after damage. One of the benefits of this technique is that only a few modes are required to obtain reliable results. From a practical point of view, this is important because during a field test the number of measured modes is limited. Limitations found in the Stubbs' Sensitivity Method and the Modified Cawley's Method (Kim and Stubbs, 1993) led to the development of this technique.

Consider a linearly elastic beam structure composed of NE elements and N nodes along its length. Letting $\psi_i(x)$ and EI(x) represent the ith mode shape vector and the beam's bending stiffness, respectively, the ith modal stiffness, K_i, of the beam is formulated as

$$K_i = \int_0^L EI(x)[\psi_i''(x)]^2 dx, \tag{5}$$

where L represents the total length of the beam (Stubbs, et al., 1995). The jth member contribution of the ith modal stiffness, K_{ij}, is given by

$$K_{ij} = EI_j \int_a^b [\psi_i''(x)]^2 dx, \tag{6}$$

where EI_j is the jth member stiffness and [a,b] represent the limits of member j. This formulation assumes that EI is constant over the interval [a,b].

For the ith mode, the fraction of modal stiffness in the jth member, which is equivalent to the modal strain energy contained in the jth member divided by the modal strain energy contained in the entire beam, is given by

$$F_{ij} = K_{ij}/K_i . \tag{7}$$

For the damaged structure, the ith-mode modal strain energy fraction concentrated in the jth member for the damaged structure is given by

$$F_{ij}^* = K_{ij}^*/K_i^* = F_{ij}(1 + \sum_{j=1}^{NE} A_{ij}\alpha_j + \text{H.O.T.}), \tag{8}$$

where

$$K_i^* = \int_0^L EI^*(x)[\psi_i^{*}''(x)]^2 dx, \tag{9}$$

and

$$K_{ij}^* = EI_j^* \int_a^b [\psi_i^{*}''(x)]^2 dx, \tag{10}$$

and the asterisks denote quantities associated with the damage structure. Again, Eq. 10 assumes that EI is constant in the damaged structure over the range [a,b].

In Eq. 8, the terms A_{ij} represent the sensitivity of the ratio F_{ij}^*/F_{ij} to the fractional decrease in flexural rigidity, α_j. The decrease in flexural rigidity for element j is given as $\alpha_j = (EI_j^* - EI_j)/EI_j$. H.O.T. represent higher order terms. For a given mode i, the terms F_{ij} and F_{ij}^* have the following properties

$$\sum_{j=1}^{NE} F_{ij} = \sum_{j=1}^{NE} F_{ij}^* = 1; \text{ and } F_{ij} << 1,\ F_{ij}^* << 1, \tag{11}$$

which can be used to formulate an approximate relationship between the pre- and post-damage behavior of the structure. The criteria that $F_{ij} << 1$ and $F_{ij}^* << 1$ are based on the assumption that the beam has been discretized into a sufficient number of small elements relative to the total length of the beam. A key assumption is now made that for the ith mode, the fractional strain energy in the jth element is approximately the same before and after damage, yielding the following relation

$$F_{ij} \cong F^*_{ij}. \tag{12}$$

Now, substituting Eqs. 7 and 8 into Eq. 12 gives

$$1 = \frac{F^*_{ij}}{F_{ij}} = \frac{(K^*_{ij} / K^*_i)}{(K_{ij} / K_i)}. \tag{13}$$

Replacing the stiffness terms of Eq. 13 with Eqs. 5, 6, 9 and 10, and assuming the EI is constant over the entire length of the beam for both the damaged and undamaged beam yields

$$1 = \frac{EI^*_j}{EI_j} \frac{\left(\int_a^b [\psi^*_i"(x)]^2 dx \ / EI^* \int_0^L [\psi^*_i"(x)]^2 dx \right)}{\left(\int_a^b [\psi_i"(x)]^2 dx \ / EI \int_0^L [\psi_i"(x)]^2 dx \right)}. \tag{14}$$

Implicit in the assumption that EI is constant over the length of beam, both before and after damage, is another assumption that damage will be located in a small number of elements, and will therefore not significantly affect the average value of EI over the entire beam. With the approximation $EI \cong EI^*$ over the entire length of the beam, Eq. 14 becomes

$$\frac{EI_j}{EI^*_j} = \frac{\left(\int_a^b [\psi^*_i"(x)]^2 dx \ / \int_0^L [\psi^*_i"(x)]^2 dx \right)}{\left(\int_a^b [\psi_i"(x)]^2 dx \ / \int_0^L [\psi_i"(x)]^2 dx \right)}. \tag{15}$$

To avoid potential numerical problems resulting from division by very small numbers, the damage index, β_{ij}, which for mode i is related to the change in the modal strain energy stored in member j, is defined as

$$\beta_{ij} = \frac{\left(\int_a^b [\psi^*_i"(x)]^2 dx \ / \int_0^L [\psi^*_i"(x)]^2 dx \right) + 1}{\left(\int_a^b [\psi_i"(x)]^2 dx \ / \int_0^L [\psi_i"(x)]^2 dx \right) + 1}. \tag{16}$$

In order to account for all n measured modes, the following formulation of the damage index equation is required

$$\beta_j = \left(\sum_{i=1}^{n} f^*_{ij} \right) \Big/ \left(\sum_{i=1}^{n} f_{ij} \right), \tag{17}$$

where

$$f_{ij} = \left(\int_a^b [\psi_i"(x)]^2 dx + \int_0^L [\psi_i"(x)]^2 dx \right) \Big/ \int_0^L [\psi_i"(x)]^2 dx, \tag{18}$$

and an analogous term f^*_{ij} can be defined using the damaged mode shapes.

Assuming that the collection of the damage indices, β_j, represents a sample population of a normally distributed random variable, a normalized damage localization indicator is obtained as follows

$$Z_j = \frac{\beta_j - \overline{\beta_j}}{\sigma_j}, \tag{19}$$

where $\overline{\beta_j}$ and σ_j represent the mean and standard deviation of the damage indices, respectively.

A statistical decision making procedure is employed to determine if the normalized damage index, Z_j, is associated with a damage location. Values two standard deviations from the mean are assumed to be associated with damage locations.

IV. B. Mode Shape Curvature Method

Damage in a structure is typically associated with a stiffness reduction (located at the vicinity of damage) and increased structural damping. These characteristics of damage, in turn, alter the vibrational characteristics of the structure such as resonant frequencies and mode shapes. A considerable amount of effort has been put into using changes in resonant frequencies and mode shapes for detecting and locating damage. In this section, the use of mode shape curvatures for identifying and locating damage in a structure is summarized. In formulating the eigenvalue problem, Pandey, Biswas, and Samman (1991) assume that structural damage only affects the stiffness matrix and not the mass matrix. For the undamaged condition the eigenvalue problem is given as

$$([K] - \lambda_i[M])\{x_i\} = \{0\}, \tag{20}$$

where $[K]$ = the stiffness matrix,
λ_i = the ith eigenvalue,
$[M]$ = the mass matrix, and
$\{x_i\}$ = the ith displacement eigenvector.

Similarly, the eigenvalue problem for the damaged condition is

$$\left([K^* - \lambda_i^*[M]]\right)\{x_i^*\} = \{0\}, \tag{21}$$

where the asterisks signify the stiffness matrix, the ith eigenvalue, and the ith eigenvector of the damaged structure. The pre- and post-damage eigenvectors are the basis for damage detection. Mode shapes curvature for the beam in undamaged and damaged condition can then be estimated numerically from the displacement mode shapes with a central difference approximation or by differentiating a function fit to the data.

Given the undamaged and damaged mode shapes, consider a beam cross section at location x subjected to a bending moment M(x). The curvature at location x, $v''(x)$, is given by

$$v''(x) = M(x)/(EI), \tag{22}$$

where E = the modulus of elasticity and
I = the moment of inertia of the section.

From this equation, it is evident that the curvature is directly proportional to the inverse of the flexural stiffness, EI. Thus, for a given moment applied to the damaged and undamaged structure, a reduction of stiffness associated with a damage incident will, in turn, lead to an increase in curvature. Furthermore, an estimation of the extent of damage at a cracked section can be obtained by measuring the amount of change in the mode shape curvatures. The larger the reduction in the flexural stiffness (i.e., higher level of damage), the larger the change in the mode shape curvatures from an undamaged to damaged condition. Differences in the pre- and post-damage mode shapes curvatures are shown to be located in the cracked region.

This method can be used with mode shapes that have been normalized arbitrarily, but consistently. Pandey, et al., do not present a means to quantify when changes in curvature are indicative of damage, hence, some engineering judgment is required when examining plots of the change of curvature as a function of position. For multiple modes, the absolute values of change in curvature associated with each mode can be summed to yield a damage parameter for a particular location.

IV. C. Change in Flexibility Method

As an alternative to using changes in the modal parameters of a structure (i.e., resonant frequencies, mode shapes, and modal damping values) for detecting damage, researchers at Duke University (Pandey and Biswas, 1994) have proposed a method which takes into account the flexibility of the structure before and after damage has occurred. The method does not require an analytical model of the structure. Resonant frequencies and mode shapes for only a few of the lower modes of vibration are needed.

For the undamaged structure, the flexibility matrix, [F], is derived from the modal data as follows

$$[F] \approx [\Phi][\Omega]^{-1}[\Phi]^T \approx \sum_{i=1}^{n} \frac{1}{\omega_i^2}\{\phi_i\}\{\phi_i\}^T, \tag{23}$$

where $\{\phi_i\}$ = the ith mass-normalized mode shape,

$[\Phi]$ = the mode shape matrix = $[\phi_1, \phi_2, \ldots, \phi_n]$,

ω_i = the ith modal frequency,

$[\Omega]$ = the modal stiffness matrix = $\mathrm{diag}\left(\omega_i^2\right)$, and

n = the number of measured or calculated modes.

The approximation in Eq. 23 comes from the fact that typically the number of modes identified is less than the number of degrees of freedom needed to accurately represent the motion of the structure.

Similarly, for the damaged structure

$$\left[F^*\right] \approx \left[\Phi^*\right]\left[\Omega^*\right]^{-1}\left[\Phi^*\right]^T \approx \sum_{i=1}^{n} \frac{1}{\left(\omega_i^*\right)^2}\left\{\phi_i^*\right\}\left\{\phi_i^*\right\}^T, \tag{24}$$

where the asterisks signify properties of the damaged structure. From the pre- and post-damage flexibility matrices, a measure of the flexibility change caused by the damage can be obtained from the difference of the respective matrices, i.e.,

$$[\Delta F] = [F] - [F^*], \tag{25}$$

where ΔF represents the change in flexibility matrix. Now, for each column of matrix ΔF let $\bar{\delta}_j$ be the absolute maximum value of the elements in the jth column. Hence,

$$\bar{\delta}_j = \max|\delta_{ij}|, \quad i = 1,\ldots n, \tag{26}$$

where δ_{ij} are elements of matrix ΔF and is taken to be a measure of the flexibility change at each measurement location. The column of the flexibility matrix corresponding to the largest $\bar{\delta}_j$ is indicative of the degree of freedom where damage is located. Interpolation between measured mode amplitudes can be used to generate additional degrees of freedom. Again, Pandey and Biswas do not present a means to quantify which values of $\bar{\delta}_j$ are indicative of damage. Also, the need for unit mass normalized modes presents a problem when this method is applied to modes obtained from ambient data.

IV. D. Change in Uniform Flexibility Shape Curvature Method

By combining certain aspects of the Mode Shape Curvature Method and the Change in Flexibility Method, Zhang and Aktan (1995) developed an alternative damage detection scheme. Similarly to the Mode Shape Curvature Method, the basic concept is that a localized loss of stiffness will produce a curvature increase at the same location. However, the change in curvature is obtained from the uniform flexibility shape instead of the mode shapes.

Recall that the flexibility matrices, before and after damage, can be approximated by the modal parameters:

$$[F] = [F_1, F_2, \ldots F_n] \approx [\Phi][\Omega]^{-1}[\Phi]^T, \tag{27}$$

and

$$[F^*] = [F_1^*, F_2^*, \ldots F_n^*] \approx [\Phi^*][\Omega^*]^{-1}[\Phi^*]^T, \tag{28}$$

where the asterisks designate the damaged structure. The quantities F_1 through F_n (with and without the asterisk) correspond to columns of the flexibility matrix. The coefficients of the ith column represent the deflected shape assumed by the structure with a unit load applied at the ith degree of freedom. For example, the third column of the flexibility matrix would correspond to the structure's deflection profile when a unit load is applied at degree of freedom three.

Zhang and Aktan use the change in curvature of the uniform load flexibility to determine the location of damage. The uniform load flexibility represents the deflected shape assumed by the structure when all degrees of freedom are loaded with a unit load. Thus, the uniform load flexibility corresponds to the sum of the unit load flexibilities. In terms of the unit load flexibilities, the curvature change is evaluated as follows

$$\{\Delta\} = \left| \sum_{i=1}^{n} \left\{ F_i^{*''} \right\} - \left\{ F_i'' \right\} \right|, \tag{29}$$

where $\{\Delta\}$ and n represent the absolute curvature change and the number of degrees of freedom, respectively. Curvature associated with each unit load flexibility can be obtained by applying a central difference operator to measured modal amplitudes, or as was done in the study reported herein, a polynomial can be fit to the modal amplitudes and then subsequently differentiated to obtain the curvature values. Interpolation procedures can again be used to generate additional degrees of freedom at locations between sensors. This method requires mass-normalized mode shapes. Zhang and Aktan do not present a method to quantify when a change in the curvature of the uniform flexibility surface corresponds to damage.

In this study, a minor adjustment was made in the sequence in which the absolute value and summation tasks were performed, that is,

$$\{\Delta\} = \sum_{i=1}^{n} \left| \left\{ F_i^{*''} \right\} - \left\{ F_i'' \right\} \right|. \tag{30}$$

Note that the absolute change in curvature is first evaluated for each unit load flexibility shape and then accumulated.

IV. E. Change in Stiffness Method

Investigation of the eigenvalue problem of a structure before and after the onset of damage has been used to develop a method for detecting damage (Zimmerman and Kaouk, 1994) . The eigenvalue problem of an undamaged, undamped structure is given as

$$(-[\Omega][M] + [K])[\Phi] = [0], \tag{31}$$

where [M] = the mass matrix of the undamaged structure,
[K] = the stiffness matrix of the undamaged structure,
$[\Phi]$ = the mode shape matrix of the pre-damaged structure = $[\phi_1, \phi_2, \ldots, \phi_n]$,
ϕ_i = the ith pre-damaged mode shape,
$[\Omega]$ = the modal stiffness matrix of the damaged structure = diag(ω_i^2), and
ω_i = the ith pre-damaged modal frequency.

The eigenvalue problem of the damaged structure is formulated by (1) replacing the pre-damaged eigenvectors and eigenvalues with a set of post-damaged modal parameters and (2) subtracting the perturbations in the mass and stiffness matrices from the original matrices. Letting $[\Delta M_d]$ and $[\Delta K_d]$ represent the perturbations to the original mass and stiffness matrices, the eigenvalue equation expands to

$$\left[-\left[\Omega^*\right]\left([M]-[\Delta M_d]\right) + \left([K]-[\Delta K_d]\right)\right]\left[\Phi^*\right] = [0], \tag{32}$$

where the asterisk denotes modal quantities associated with the damaged structure.

Two forms of a damage vector {D} are then obtained by separating the terms containing the original matrices from those containing the perturbation matrices, hence,

$$\{D_i\} = \left[-\omega_i^{*2}[M] + [K]\right]\{\phi_i^*\} = \left[-\omega_i^{*2}[\Delta M] + [\Delta K]\right]\{\phi_i^*\}. \tag{33}$$

To simplify the investigation, damage is usually considered to affect only the stiffness of a structure because substantial damage must occur to disrupt the mass. Therefore, assuming that the effect of damage on the mass matrix is negligible, the damage vector reduces to

$$\{D_i\} = [\Delta K]\{\phi_i^*\}. \tag{34}$$

The stiffness matrices of the structure, before and after damage, can be approximated from the modal parameters by

$$[K] \approx [\Phi][\Omega][\Phi]^T \approx \sum_{i=1}^{n} (\omega_i)^2 \{\phi_i\}\{\phi_i\}^T, \text{ and} \tag{35}$$

$$[K^*] \approx [\Phi^*][\Omega^*][\Phi^*]^T \approx \sum_{i=1}^{n} (\omega_i^*)^2 \{\phi_i^*\}\{\phi_i^*\}^T. \tag{36}$$

The approximation is the result of typically only having a limited number of modes available with which to form the stiffness matrix. The pre- and post-damage stiffness matrices are subtracted, the difference is multiplied by the damaged mode shape vector to obtain the damage vector.

Interpolation between measured mode amplitudes can be used to generate additional degrees of freedom. Again, Zimmerman and Kaouk do not present a means to quantify which values of the damage vector are indicative of damage. Also, the need for mass-normalized modes presents a problem when this method is applied to modes obtained from ambient data.

Stiff regions of the structure can cause problems in locating damage because noise in the measurements can cause a stiffness variation larger than one caused by damage in a less stiff area (Simmermacher, et. al. 1995). Because of this concern, some form of scaling is required in order to minimize the effect of noise at highly stiff regions. In this study, the scaling used is defined as

$$\{D_{si}\} = [W]\{D_i\}, \tag{37}$$

where

$$[W] = \text{diag}\left(\frac{1}{\|z^1\|}, \frac{1}{\|z^2\|}, \frac{1}{\|z^3\|}, \ldots, \frac{1}{\|z^n\|}\right), \text{ and} \tag{38}$$

$$[Z] = \begin{bmatrix} z^1 \\ z^2 \\ z^3 \\ \vdots \\ z^n \end{bmatrix} = [\Delta K]. \tag{39}$$

A normalized, scaled damage matrix, $[D_s]$, is then formed from the normalized, scaled damage vectors such that $[D_s] = [D_{s1}, D_{s2}, D_{s3},...D_{sn}]$. Simmermacher states that the first left singular vector resulting from a singular value decomposition of the normalized damage matrix (Eq. 37) contains the most relevant information regarding damage. Regions adjacent to the interior supports of the bridge represent areas of large stiffness. Thus, the scaling was performed so that damage would not be falsely detected at the pier locations.

V. APPLICATION OF DAMAGE IDENTIFICATION METHODS TO EXPERIMENTAL AND NUMERICAL DATA

In this section, the linear damage identification methods are exercised using experimental and numerical modal data for the I-40 Bridge. As discussed earlier, the data used for the damage diagnosis consist of resonant frequencies and mode shapes corresponding to bending and torsional modes of the bridge. Lateral response data were not obtained experimentally, and, hence, were not extracted from the analytical data. The three sets of modal data used to test the damage identification routines are as follows:

(1) SET1 - experimental modal data obtained via CPS from refined sensor measurements (see Fig. 9)
(2) SET2 - experimental modal data obtained via global polynomial curve fit of coarse sensor measurements (see Fig. 8). Note the mode shape vectors from this set of data are mass normalized.
(3) SET3 - numerical modal data obtained via CPSD from refined sensor measurements (see Fig. 29)

The SET1 data is tabulated in the first five tables of Appendix A. Table A-1 represents the undamaged modal data whereas Tables A-2 through A-5 contain modal data for the four damage conditions, cases E-1 through E-4, respectively. The latter five tables, A-6 through A-10, summarize the SET2 modal data. Table A-6 corresponds to the undamaged modal data and Tables A-7 through A-10 are associated with damage cases E-1 through E-4, respectively. The numerically generated set of modal data (SET3) is tabulated in Tables B-1 through B-10 of Appendix B. Table B-1 contains the undamaged modal data, Tables B-2 through B-9 contain the damaged modal data for damage cases A-1 through A-8, and Table B-10 contains the modal data for the alternate undamaged case A-9.

Two of the damage detection methods require only normalized mode shapes, namely the Damage Index Method and the Mode Shape Curvature Method. The Change in Flexibility Method, the Change in Uniform Flexibility Shape Curvature Method, and the Change in Stiffness Method require the resonant frequency for each mode and mass-normalized mode shape vectors.

In accordance with Stubbs, et al. (1995), an Euler-Bernoulli beam was selected to model the north damaged girder of the I-40 Bridge for two reasons: (1) the fundamental behavior of a bridge resembles that of a composite (concrete and steel) beam and (2) only vertical accelerations were measured which can be simulated with a one-dimensional beam. Because of the contrast in the layout scheme between the coarse and refined set of accelerometers, it was necessary to create two damage detection models (DDM); one representing the entire north girder and one representing only the damaged span of the north girder. Figure 42 shows the coarse set of accelerometer locations with respect to the DDM of the entire north girder. The DDM of the full length girder was a 420-ft beam discretized with 210 two-foot elements and 211 equally spaced nodes. Discontinuities in the flange dimensions occur at elements 62, 80, 140 and 158 in this DDM. Splice plates, which also cause local stiffness discontinuities, are located at elements 47, 89, 122, and 163. Plots (a) and (b) of Fig. 43 show the positions of the refined set of accelerometers corresponding to the experimental setup and the numerical model, respectively . Figure 43(c) shows the DDM of the 160-ft damaged span modeled with 160 one-foot elements and 161 nodes.

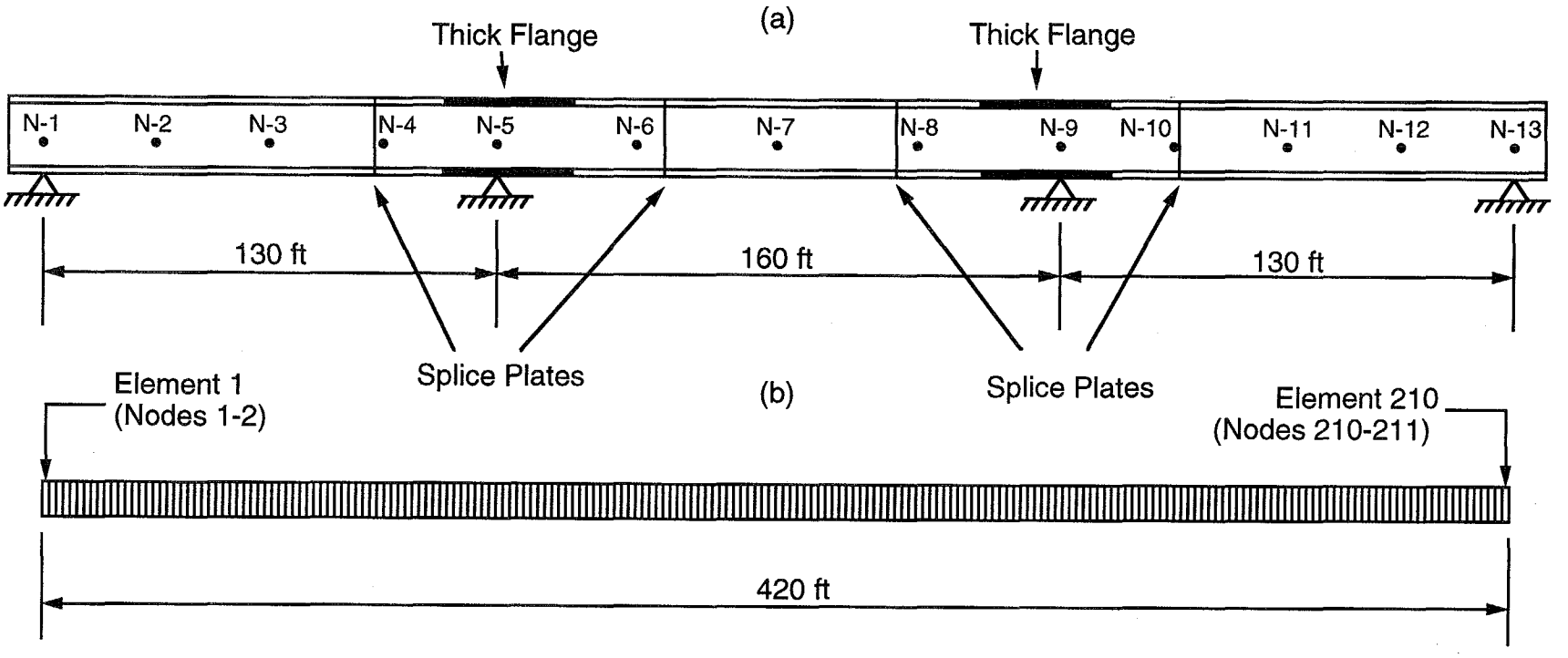

Fig. 42. (a) Coarse set of accelerometer locations in experimental setup and (b) damage detection model of north damaged girder.

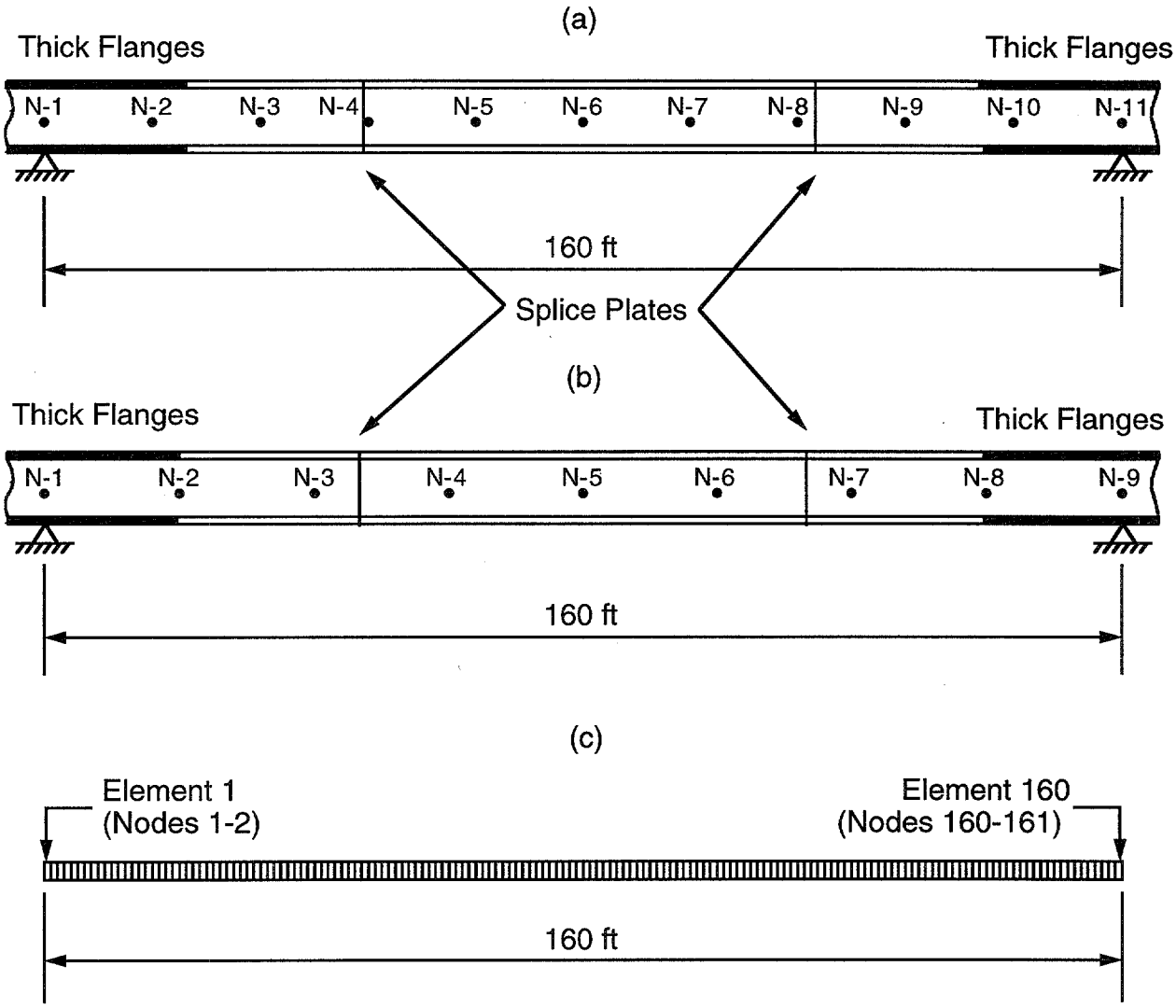

Fig. 43. (a) Refined set of accelerometer locations in experimental setup, (b) refined set of accelerometer locations in numerical setup, and (c) damage detection model of damaged span.

For this DDM discontinuities associated with the change in flange dimension occur at elements 20 and 140. Discontinuities associated with the splice plates occur at elements 46 and 113. Note that the splice plates were not modeled in the FEM.

Although the damage models can be refined by varying the element length, the selected element size was considered sufficient for determining the damage location. If damage can be located to within one or two feet of its actual location, a Level II damage diagnosis was considered successful. Note that the damage detection models were created simply to partition the north girder in order to monitor damage at discrete locations and should not be confused with nodes and elements in the finite element sense.

With respect to the DDM, the magnitudes of the mode shapes are known only at a few nodal locations. For example, the locations of the refined set of accelerometers in the experimental layout

(see Fig. 43(a)) correspond to nodes 1 through 161 in increments of 16 (i.e., 1, 17, 33, etc.) of the DDM of the damaged span (see Fig. 43(c)). Determining the location of damage based solely on the limited number of mode shape values would require that damage occur in the vicinity of one of the sensors. In the event that damage should occur at a location between two neighboring sensors no information is available in that region to locate the damage. Thus, in order to improve the sophistication of the damage detection routines, the magnitudes of the mode shapes at intermediate nodal locations of the damage detection models must first be estimated by some form of interpolation. By interpolating between the known mode shape values, intermediate values are generated making it possible to locate damage between adjacent sensors. Two forms of interpolation were used in this study, a cubic spline interpolation scheme and a cubic polynomial interpolation scheme.

A common characteristic that all damage detection methods strive for is that their associated algorithms should produce unambiguous signs of damage at the location where damage occurred. Thus, the nodes and elements of the damage detection models which are expected to be affected by damage cases E-1 through E-4 and A-1 through A-8 are summarized in Table VIII.

V. A. Damage Index Method

Using the experimental modal data summarized in Tables A-1 through A-5 of Appendix A, the damage index technique was shown to be able to locate and estimate the severity of damage in the I-40 Bridge (Stubbs and Kim, 1994). The authors point out several important features of the technique (Stubbs et al., 1995) which include: (1) the analysis calls for mode shapes only, (2) a few low frequency modes are sufficient for detecting damage, (3) resonant frequencies and damping information are not required, and (4) damage can be located in a structure consisting of many elements. The basic idea is that the distribution of strain energy originally stored in the structure will decrease in damaged areas. Once a structural member experiences a reduction of stiffness it can no longer absorb the same amount of energy as it did when undamaged thus causing a deviation from the original strain energy distribution of the undamaged structure. Thus, changes in the strain energy distributions of the undamaged and damaged structures can first be used to detect and locate damage.

TABLE VIII

Nodes and Elements of Damage Detection Models Corresponding to the Locations of Damage for Cases E-1 through E-4 and A-1 through A-8

Damage Case	Affected Nodes of DDM	Affected Element(s) of DDM
E-1 through E-4 *	82, 83	82
E-1 through E-4 **	106, 107	106
A-1 through A-3	80, 81	80
A-4	40, 41	40
A-5	20, 21	20
A-6 ***	40,41 100,101	40 100
A-7	40, 41	40
A-8	20, 21	20

* SET1 modal data
** SET2 modal data
*** Two locations of damage

The distributions of strain energy in the structure, before and after damage, are calculated from the associated mode shapes and subsequently used to compute the damage localization indicator (DLI). Equation 17 is used to calculate the damage localization indicator. Stubbs et al. (1995) associate damage locations with statistical outliers of the damage localization indicator. A normal distribution is fit to the damage localization indicators and values more than two standard deviations from the mean are assumed to correspond to damage locations.

Before investigations were conducted using the numerically generated modal data, a MATLAB version of the Damage Index Method was first shown to be able to reproduce the results documented in Stubbs and Kim (1994). This verification was done to gain familiarity with the algorithms in order to apply them properly to the remaining sets of modal data.

V. A. 1. Damage Index Method Applied to Experimental Data

The resulting damage localization indicator for the four levels of actual damage, damage cases E-1 through E-4, determined using the SET1 modal data are plotted in Figs. 44 and 45. The DLI values plotted in Fig. 44 were obtained using a cubic spline whereas the magnitudes presented in Fig. 45 were determined using a cubic polynomial interpolation function. These figures are almost identical to the ones given in the TAMU report (Stubbs and Kim, 1994). The figures indicate that no damage exists other than at the damage locations summarized in Table IX. Included in this table are the number and range of elements which exceeded the damage criteria for the four damage cases.

According to Table IX, the number and range of elements affected by damage depends on how the mode shapes are interpolated. For damage cases E-1 through E-3, the cubic spline interpolator resulted in a larger amount of predicted damage locations. Furthermore, the range of elements affected by damage differed between the two interpolation schemes. No discrepancy was discovered in either the number or range of affected elements for damage case E-4.

Figure 46 shows the DLI for damage cases E-1 through E-4 computed by means of the SET2 modal data. The mode shapes were interpolated using only the cubic polynomial function. Note that the elements span along the entire length of the north girder and that element 106 corresponds to the location of damage. Two sets of DLI data are plotted; one plot includes the influence of all six modes on the DLI and the other includes only the affect of the first bending and first torsional modes. This comparison illustrates that modes not directly affected by damage may disrupt the performance of the damage localization indicator. For damage cases E-1 through E-3, plots (a) through (c) show that a better indication of the actual location of damage was achieved with only two modes. By including the four higher frequency modes, erroneous indications of damage were produced. For damage case E-4, there is essentially no difference between the DLI calculated using six modes or two modes. Table X summarizes the predicted locations for damage cases E-1 through E-4 using the SET2 modal data.

TABLE IX

Summary of Predicted Damage Locations for Damage Cases E-1 through E-4 using SET1 Modal Data

	Cubic Spline Interpolation		Cubic Polynomial Interpolation	
Damage Case	# of Elements with DLI ≥ 2.0	Range of Elements	# of Elements with DLI ≥ 2.0	Range of Elements
E-1	10	75 - 84	9	77 - 85
E-2	10	74 - 83	6	79 - 84
E-3	9	74 - 82	5	80 - 84
E-4	10	76 - 85	10	76 - 85

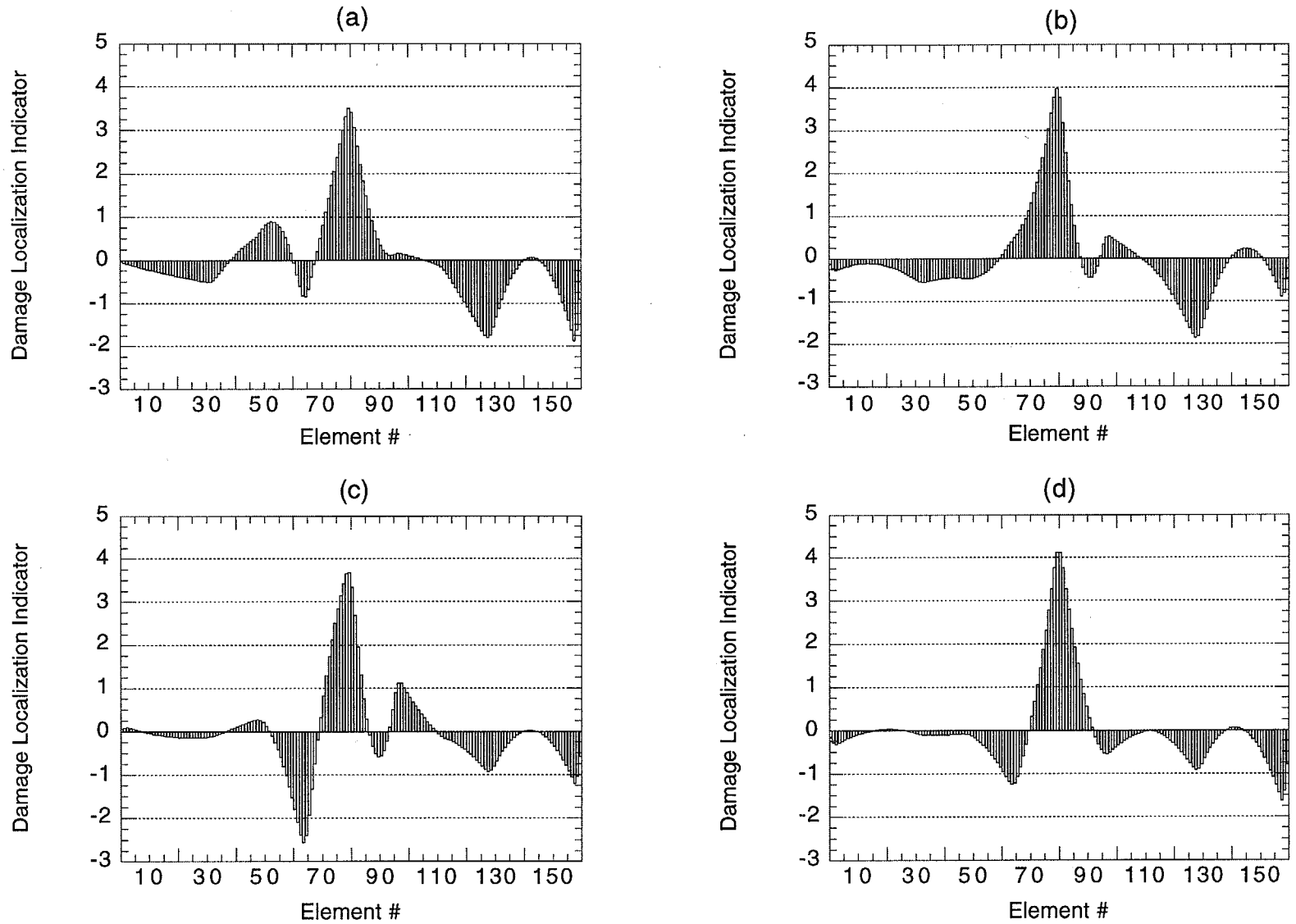

Fig. 44. Damage localization indicator for damage case (a) E-1, (b) E-2, (c) E-3, and (d) E-4 computed using the SET1 modal data and a cubic spline interpolation scheme.

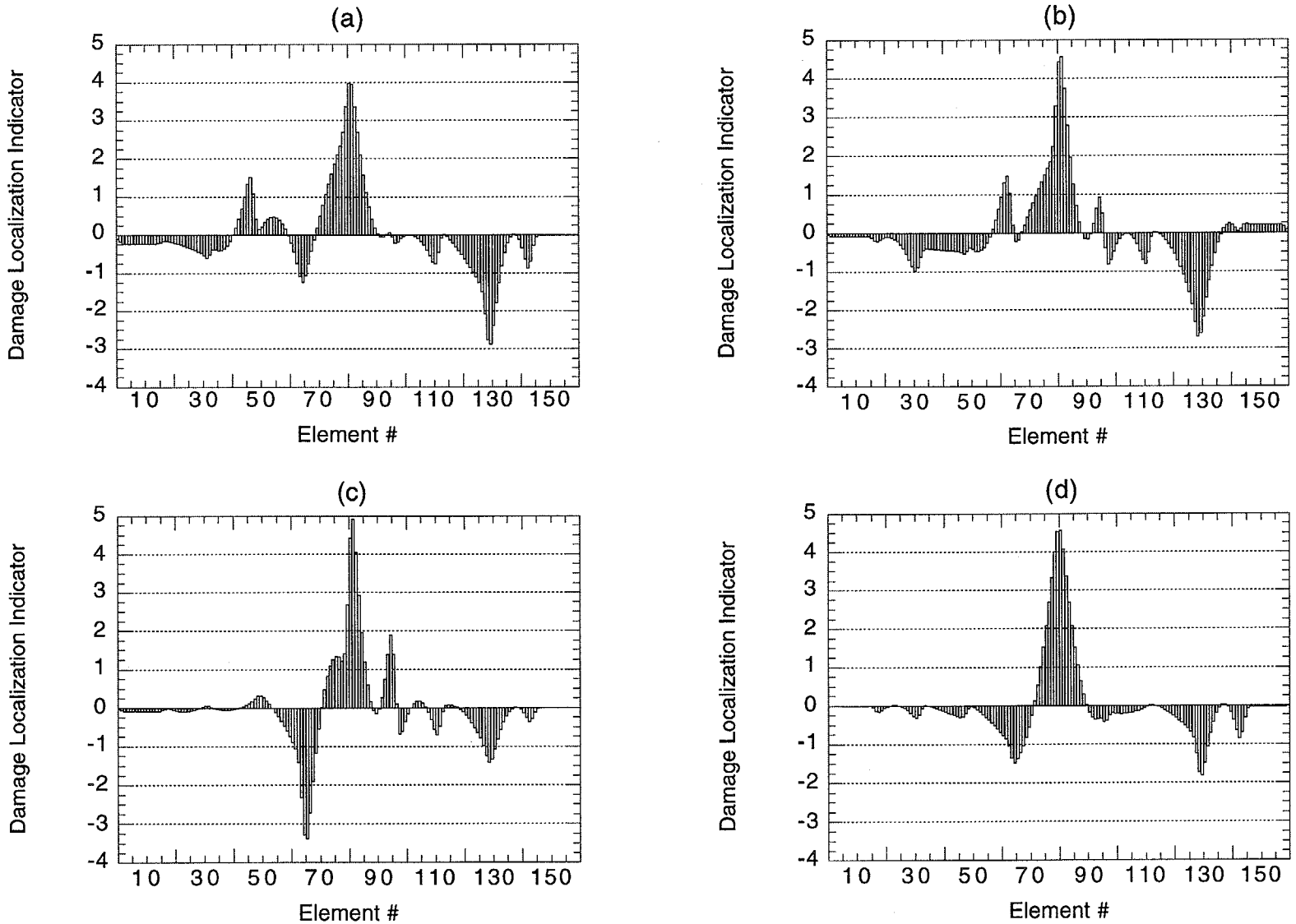

Fig. 45. Damage localization indicator for damage case (a) E-1, (b) E-2, (c) E-3, and (d) E-4 computed using the SET1 modal data and a cubic polynomial interpolation scheme.

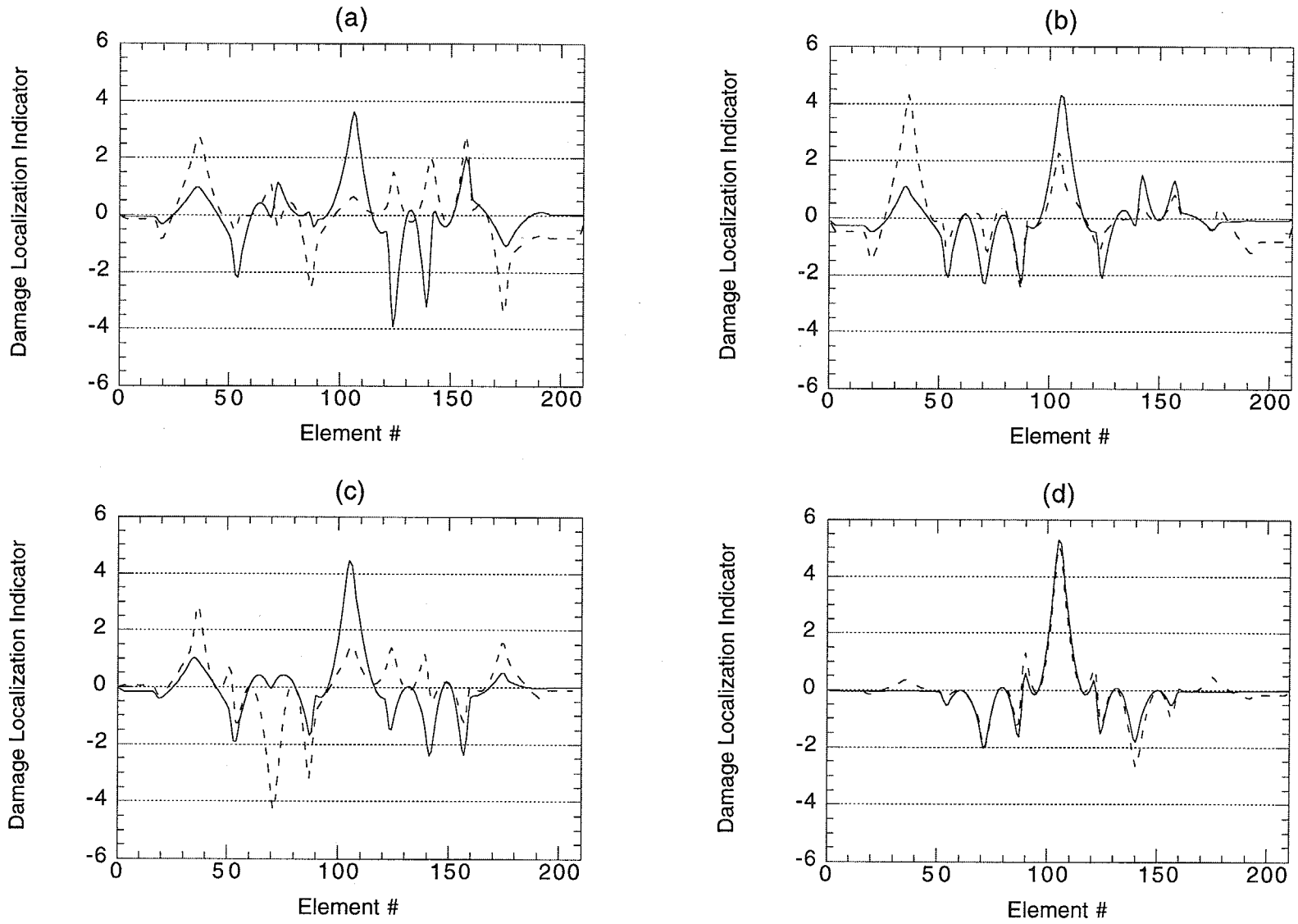

Fig. 46. Damage localization indicator for case (a) E-1, (b) E-2, (c) E-3, and (d) E-4 computed using the SET2 modal data and a cubic polynomial interpolation scheme: ——— , two modes; - - - - - , all six modes.

TABLE X

Summary of Predicted Damage Locations for Damage Cases E-1 through E-4 using SET2 Modal Data

	Six Modes		Two Modes	
Damage Case	# of Elements with DLI ≥ 2.0	Range of Elements	# of Elements with DLI ≥ 2.0	Range of Elements
E-1	9	34 - 38 141 156 - 158	8	103 - 109 157
E-2	12	31 - 40 104 - 105	9	101 - 109
E-3	4	35 - 38	10	101 - 110
E-4	9	101 - 109	10	101 - 110

Results summarized in Table X indicate that when damage is not severe, the damage locations predicted with the DLI may be misleading when modes unaffected by damage are included in the calculation.

V. A. 2. Damage Index Method Applied to Numerical Data

Figure 47 shows the DLI values calculated for damage cases A-1 through A-3 using the SET3 modal data and a cubic spline interpolation scheme. No clear indication of the correct damage location is apparent until case A-3 (i.e., 3 1/2 foot web plus total flange cut) was introduced. The DLI for damage cases A-1 through A-3 is also plotted for the cubic polynomial interpolation, as shown in Fig. 48. Contrary to the results produced from the cubic spline, there exist accurate indications of damage for the two intermediate levels of damage, cases A-1 and A-2, in addition to the final damage case A-3. At midspan, the criteria for damage was satisfied in the element range of 79 through 81 for cases A-1 and A-2. For damage case A-3, the affected element range expanded to 76 through 85. Thus, the typical smeared damage behavior does not occur until the bottom flange is completely severed. However, for cases A-1 and A-2, when the cubic polynomial interpolation scheme is used, there are incorrect indications of damage at element 20. This element corresponds to locations where there is an abrupt change in the flange dimensions of the plate girder. Flange dimensions over the piers have been increased from 21 x 1.25 in. to 24 x 2.625 in. to better resist the higher bending moments at these locations. This increased dimension produces a 58.5% increase in the bending stiffness for the portions of the plate girders near the piers. A similar change in flange dimension occurs at element 140, but there is no evidence of a false indication of damage at this location.

A similar analysis was performed for the damage conditions of cases A-4 through A-8 and for the alternate undamaged case, A-9. The results are shown in Figs. 49 through 50 and summarized in Table XI. As shown in plots (a) of Figs. 49 and 50, both mode shape interpolation schemes were able to locate the damage associated with case A-4. For damage case A-5, an accurate prediction was made only when the mode shapes were interpolated with the cubic polynomial function (see Fig. 50(b)). The DLI obtained via the spline interpolated mode shapes showed a false damage location near the end of the span (see Fig. 49(b)) which was believed to be caused by inaccuracies in the end conditions of the fit. From Figs. 49 and 50 (c), the DLI computed for damage case A-6 revealed two positive peaks at the two damaged locations, elements 40 and 100. However, the damage criteria ($|Z| > 2$) was satisfied only at one location: halfway between midspan and the quarter point. Neither of the two interpolation methods were able to predict the damage location for case A-7 (view plot (d) of Figs. 49 and 50) and the cubic polynomial interpolation scheme, in

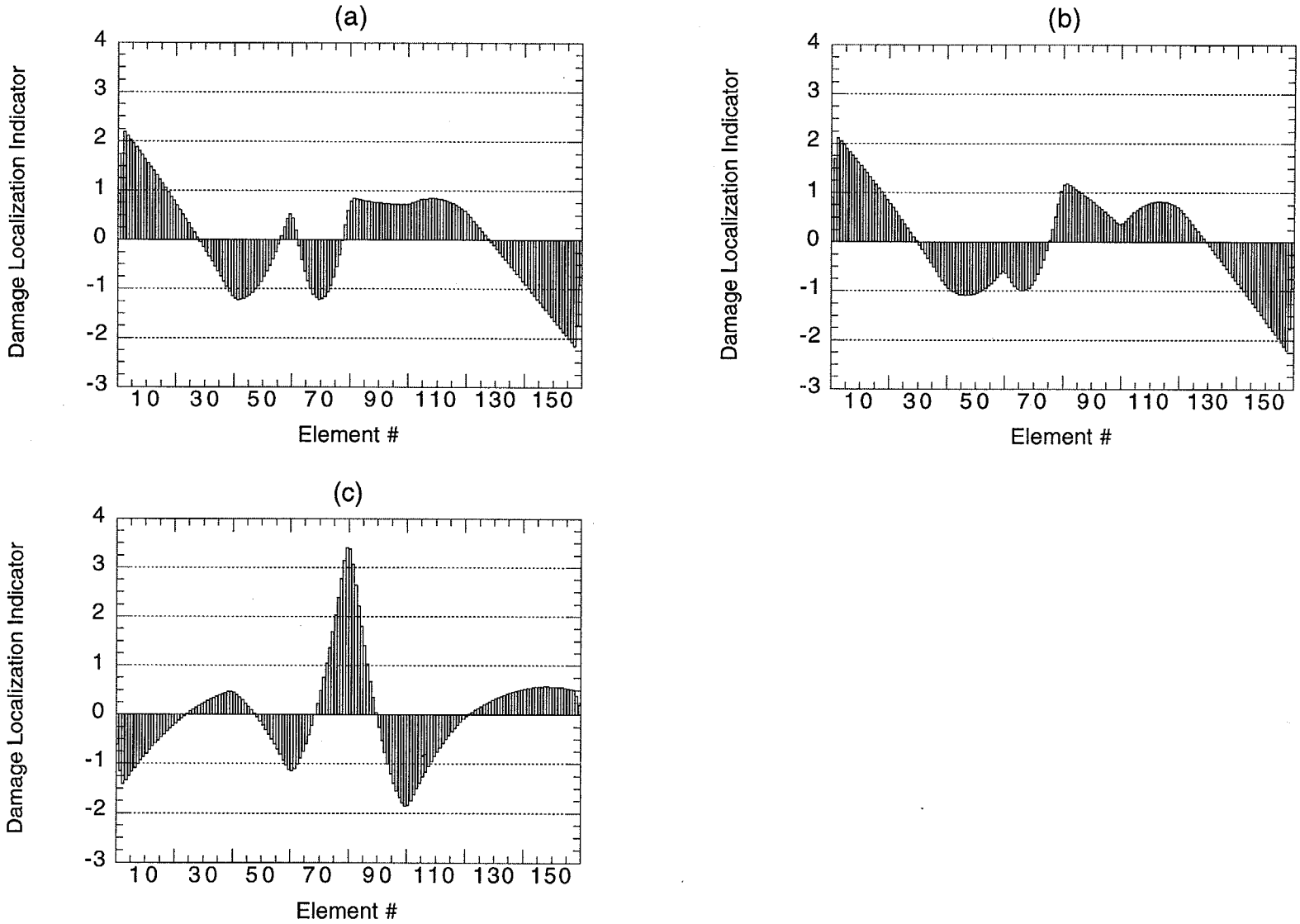

Fig. 47. Damage localization indicator for damage case (a) A-1, (b) A-2, and (c) A-3 computed using the SET3 modal data and a cubic spline interpolation scheme.

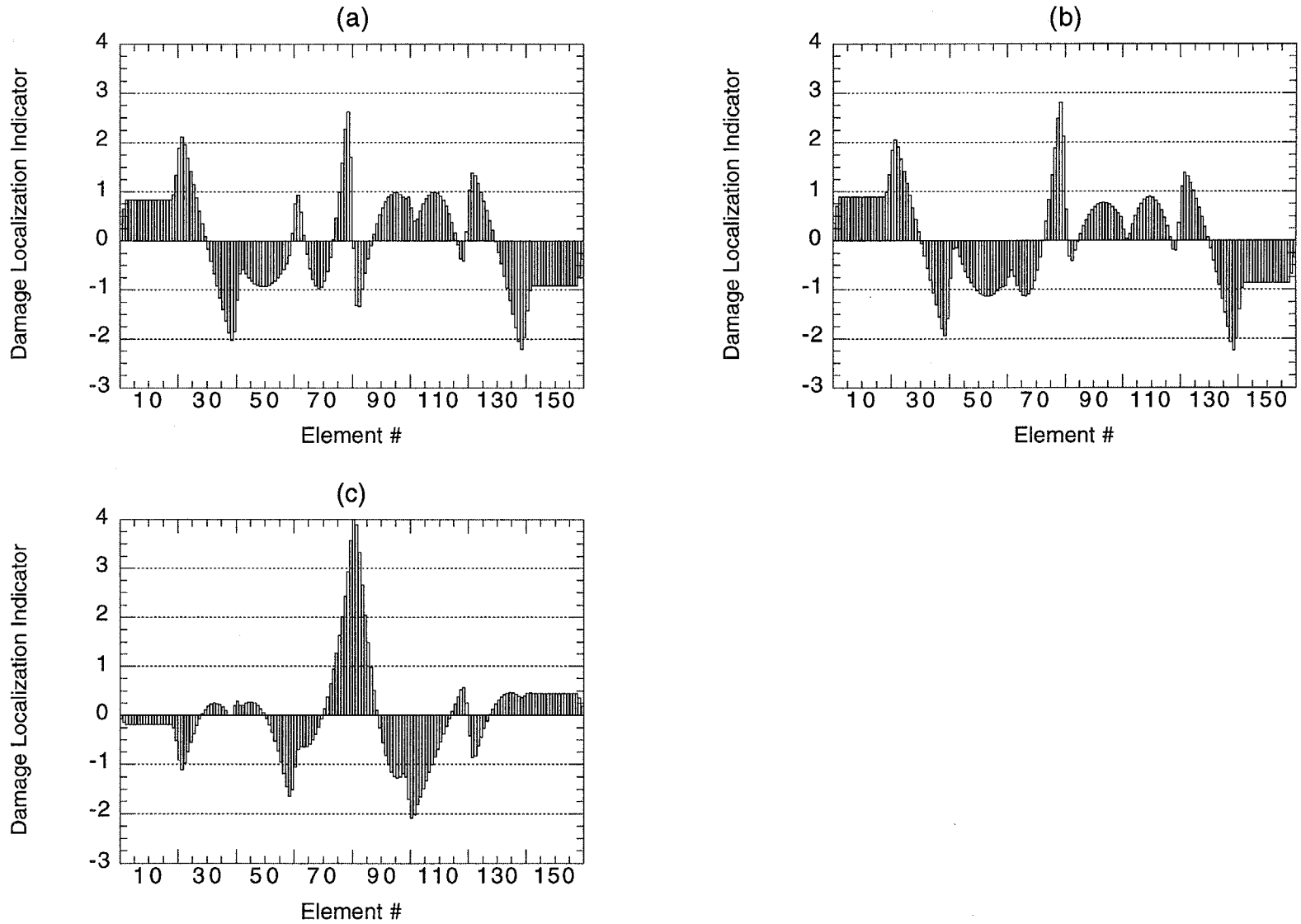

Fig. 48. Damage localization indicator for damage case (a) A-1, (b) A-2, and (c) A-3 computed using the SET3 modal data and a cubic polynomial interpolation scheme.

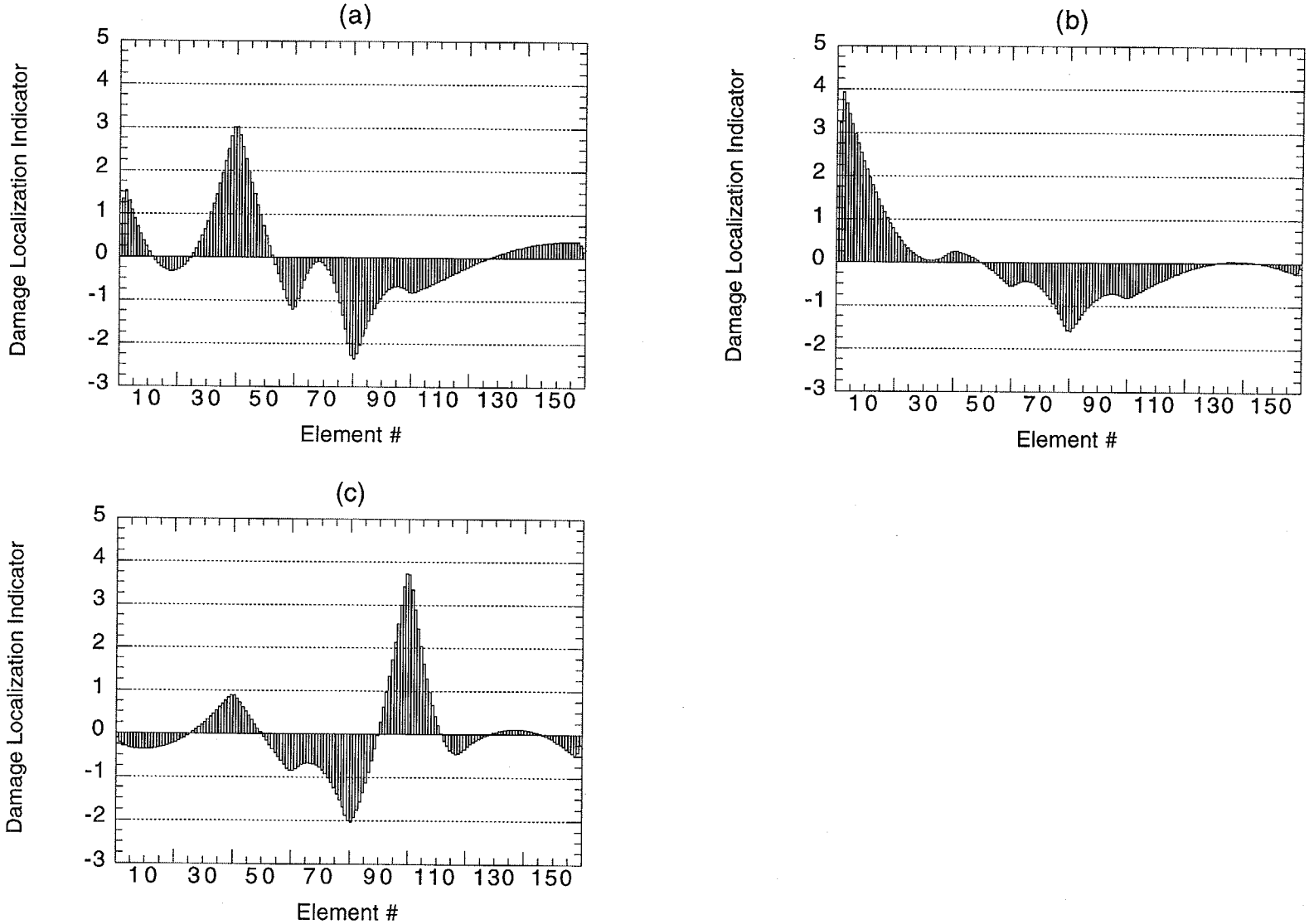

Fig. 49. Damage localization indicator for damage case (a) A-4, (b) A-5, and (c) A-6 computed using the SET3 modal data and a cubic spline interpolation scheme.

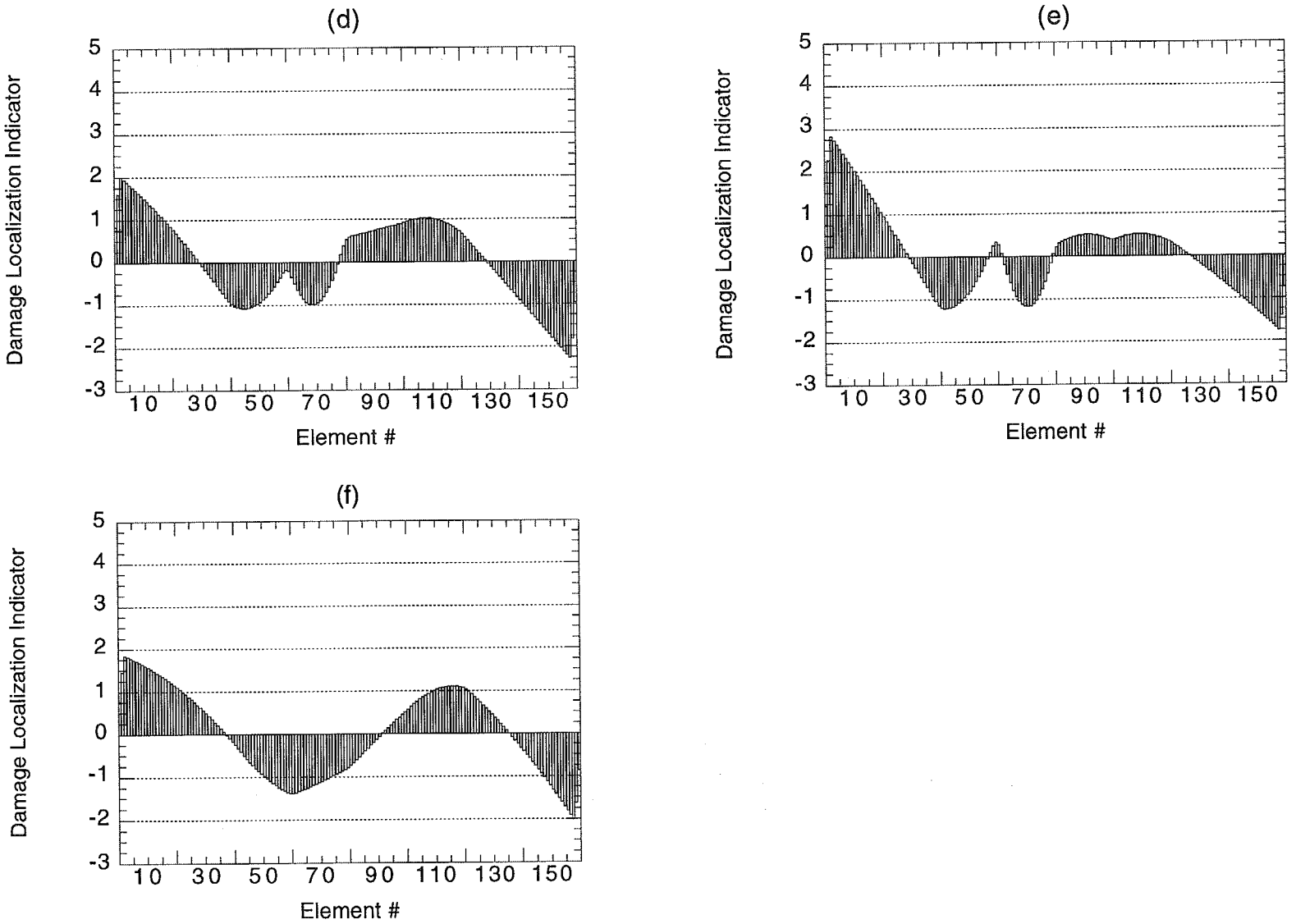

Fig. 49 (cont). Damage localization indicator for damage case (d) A-7, (e) A-8, and the alternate undamaged case (f) A-9 computed using the SET3 modal data and a cubic spline interpolation scheme.

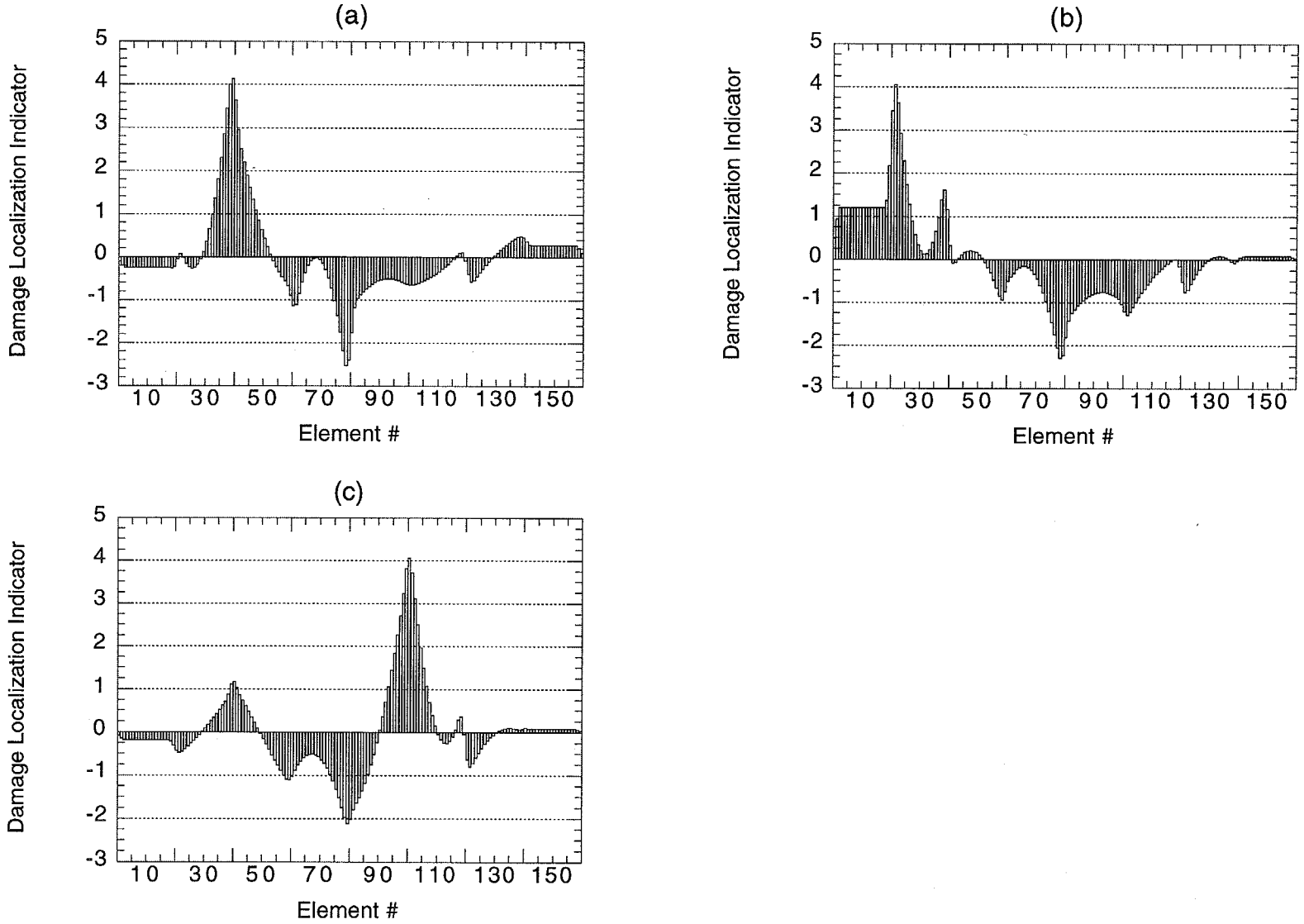

Fig. 50. Damage localization indicator calculated for damage case (a) A-4, (b) A-5, and (c) A-6 computed using the refined set of simulated accelerometer measurements; mode shapes are interpolated with a cubic polynomial function.

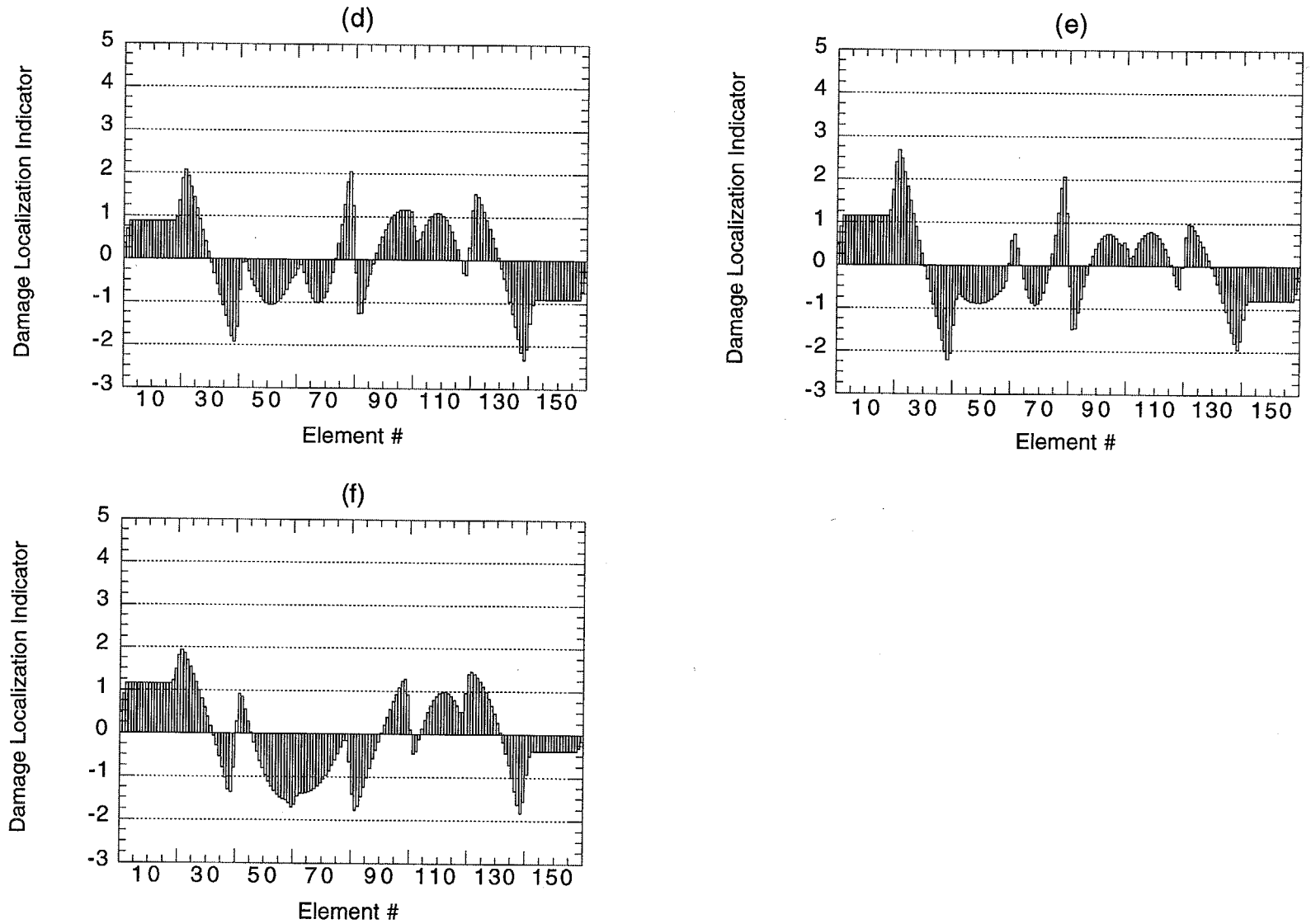

Fig. 50 (cont). Damage localization indicator calculated for damage case (d) A-7, (e) A-8, and the alternate undamaged case (f) A-9 computed using the refined set of simulated accelerometer measurements; mode shapes are interpolated with a cubic polynomial function.

TABLE XI

Summary of Predicted Damage Locations for Damage Cases A-4 through A-8 using SET3 Modal Data

	Cubic Spline Interpolation		Cubic Interpolation	
Damage Case	# of Elements with DLI ≥ 2.0	Range of Elements	# of Elements with DLI ≥ 2.0	Range of Elements
A-4	8	37 - 44	9	36 - 44
A-5	10	2 - 11	6	20 - 25
A-6	10	96 - 105	8	97 - 104
A-7	0	-----	2	22, 79
A-8	10	2 - 11	5	21 - 24, 79

fact, gives two incorrect indications of damage at element 22 and element 79. Comparison of Fig. 49(e) and Fig. 50(e) reveals that only the cubic polynomial interpolation gave positive indications of the damage location for case A-8, but this plot also shows a false indication of damage at element 79. For case A-9, the damage criteria was not met for any location by either interpolation scheme, although it is very close to being met near element 3 when the spline function is used and element 20 when the polynomial function is used (see plot (f) of Figs. 49 and 50). Therefore no false-positive readings were obtained with this method. Based on the performance of the cubic polynomial interpolation, it was decided that all subsequent damage identification studies would be done with only the cubic polynomial interpolation function.

V. B. Mode Shape Curvature Method

Damage is associated with decreases in the resonant frequencies, increases in the damping values, and alterations of the modes of vibration of the structure (Pandey, et al., 1991). The first two attributes have shown little promise for detecting the presence of damage and their applicability for locating damage is limited. This inability to locate damage is caused by the fact that two separate damage situations, dissimilar in extent and/or location, may cause the same shift in these modal parameters. Furthermore, direct comparison of the pre- and post-damage mode shapes has been found ineffective in identifying the damaged region unless damage is severe. In an effort to overcome these restrictions, researchers at Duke University proposed a method capable of not only locating damage but also estimating its severity. Advantages of the Mode Shape Curvature Method resemble those described as important features of the Damage Index Method. In addition, the computation required to implement the Mode Shape Curvature Method is less demanding than the Damage Index Method.

In Pandey, et al. (1991) the Mode Shape Curvature technique was applied successfully utilizing displacement mode shapes extracted numerically from finite element models of a cantilever and simply supported beam. A localized loss of stiffness was simulated simply by reducing the modulus of elasticity of a single element. The location of damage was varied by imposing a fixed percentage reduction to the modulus of elasticity sequentially to each element. In each case, the maximum change in curvature was associated with the vicinity of damage. To further the study, various levels of damage were simulated by reducing the modulus of elasticity of an individual element by increasing percentages. Again, the maximum change in curvature occurred at the location of damage. Furthermore, the maximum change in curvature at the damaged location increased with each incremental decrease in the modulus of elasticity.

The general idea of this technique is that a stiffness reduction caused by damage will present itself with an increase in curvature at that same location. This logic is based on the relationship between curvature and the flexural stiffness of a beam. By definition, curvature is the bending moment in

the cross-section of a beam divided by its flexural stiffness. Because of this inverse relationship, for a given moment, decreasing the flexural stiffness of the beam consequently causes an increase in curvature. Assuming that damage occurs in a localized region, the maximum difference between the pre- and post-damage mode shapes is expected to be localized in the vicinity of damage. Because the flexural stiffness is represented as the product of the moment of inertia and the modulus of elasticity, a reduction in stiffness is produced by a decrease in either quantity. In this study, the stiffness reduction is associated with a decrease in the moment of inertia because damage consisted of a loss of cross section and not an alteration of the material properties.

Implementation of this approach requires only a few steps. First, a cubic interpolation function is fit through the known modal amplitudes associated with the undamaged and damaged structure to obtain pre- and post-damage mode shape functions. Again, it was decided that only the cubic form of interpolation will be used because of its performance with the Damage Index Method. Curvature mode shapes, representative of the structure before and after damage, are then determined by differentiating the mode shape functions. The absolute value of the difference between the respective curvature mode shapes is then calculated for each individual mode. Differences for each mode are added to form a final measure of the change in curvature at a particular location.

V. B. 1. Mode Shape Curvature Method Applied to Experimental Data

For the cases of increasing damage at the midspan of the north girder, E-1 through E-4, the absolute difference between the curvature mode shapes for the undamaged and damaged bridge are plotted in Figs. 51 and 52. The results plotted in Fig. 51 and Fig. 52 were generated using the SET1 and SET2 sets of modal data, respectively.

Recall that the largest maximum change corresponds to the location in which damage is most probable. According to plot (a) of Fig. 51 which corresponds to damage case E-1, the maximum difference in curvature occurs in the vicinity of nodes 97, 33, and 82 in order of decreasing maximum change. Noting that damage was located in the vicinity of node 82, the exact damage location was associated with the third largest change in curvature. For the second damage level, case E-2, the incorrect damage location at node 33 was eliminated leaving only nodes 96 and 82 as possible damage areas (see plot (b) of Fig. 51). In this case, the correct damage location was associated with the second largest change in curvature. For the last two stages, damage cases E-3 and E-4, the maximum difference in curvature occurs in the damaged region (see plots (c) and (d) of Fig. 51). From these plots, it is evident that the accuracy of the algorithm improves as the amount of damage increased. the need for a quantifiable method for assessing whether a change in the curvature indicates damage is apparent in these plots. If these tests were performed blind, it would be difficult to claim that the plot in Fig. 51d did not identify three damage locations.

For purpose of comparison, a similar scale is used for all four plots of Fig. 51. Note that the maximum change in curvature at the damage location increases as we progress from plot (a) to (d). From this observation, it is evident that the magnitude of the change in curvature increases as more damage is induced to the bridge. It is also apparent that plot (a) represents the damage in its initial stage and plot (d) corresponds to the most severe damage. Curvature changes from six modes were used to generate the plots in Fig. 51.

Using the SET2 collection of modal data, the change in curvature was computed for damage cases E-1 through E-4 and plotted in Fig. 52. Note that two sets of mode shape curvature data are presented in each plot of the figure. The first set is the sum of the absolute difference between the curvature mode shapes of the first bending and first torsional modes, only. The second set represents an accumulation of the absolute difference in curvature mode shapes for all six modes.

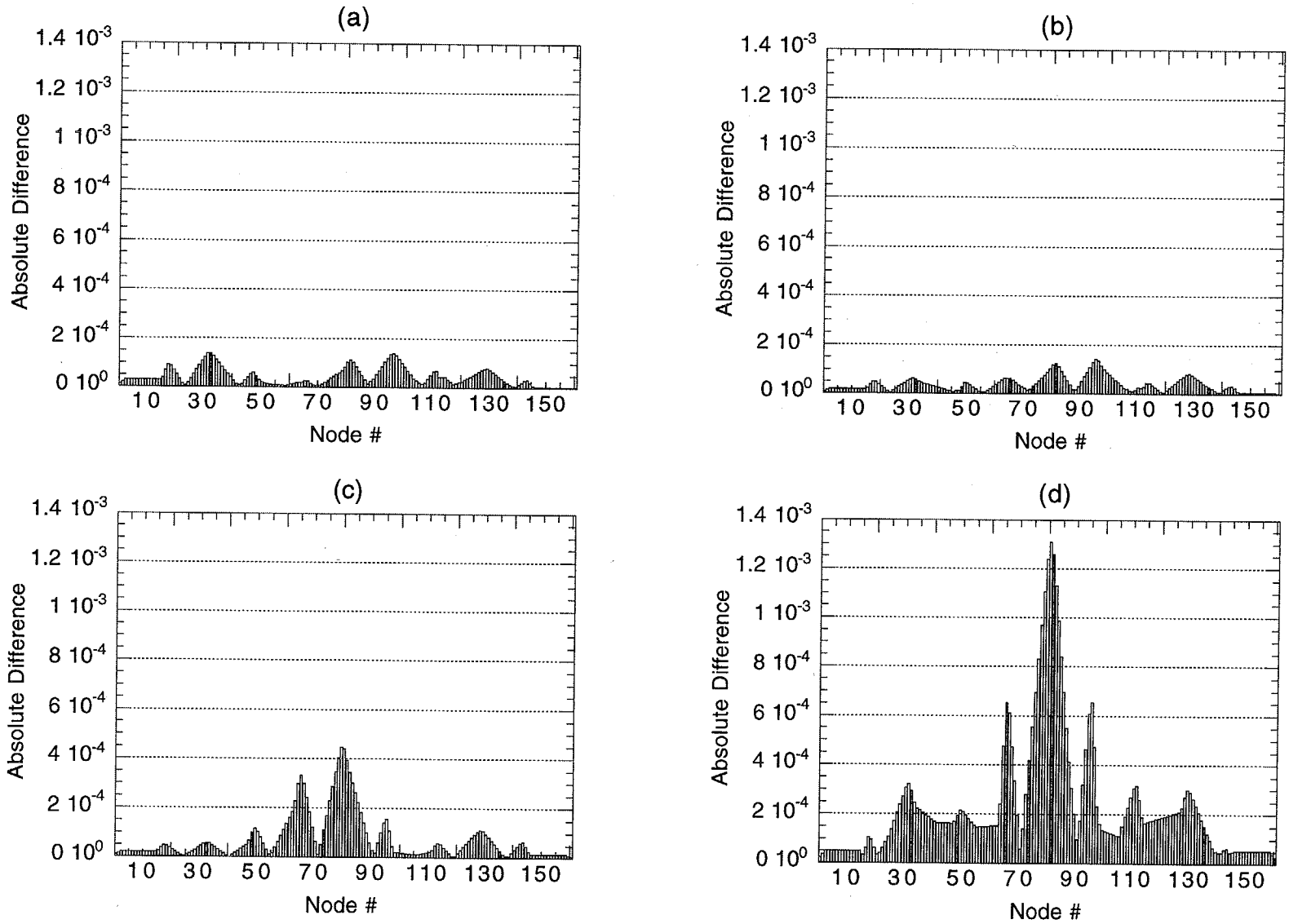

Fig. 51. Absolute difference in mode shape curvatures between the undamaged and damaged bridge for damage case (a) E-1, (b) E-2, (c) E-3, and (d) E-4 computed using the SET1 modal data.

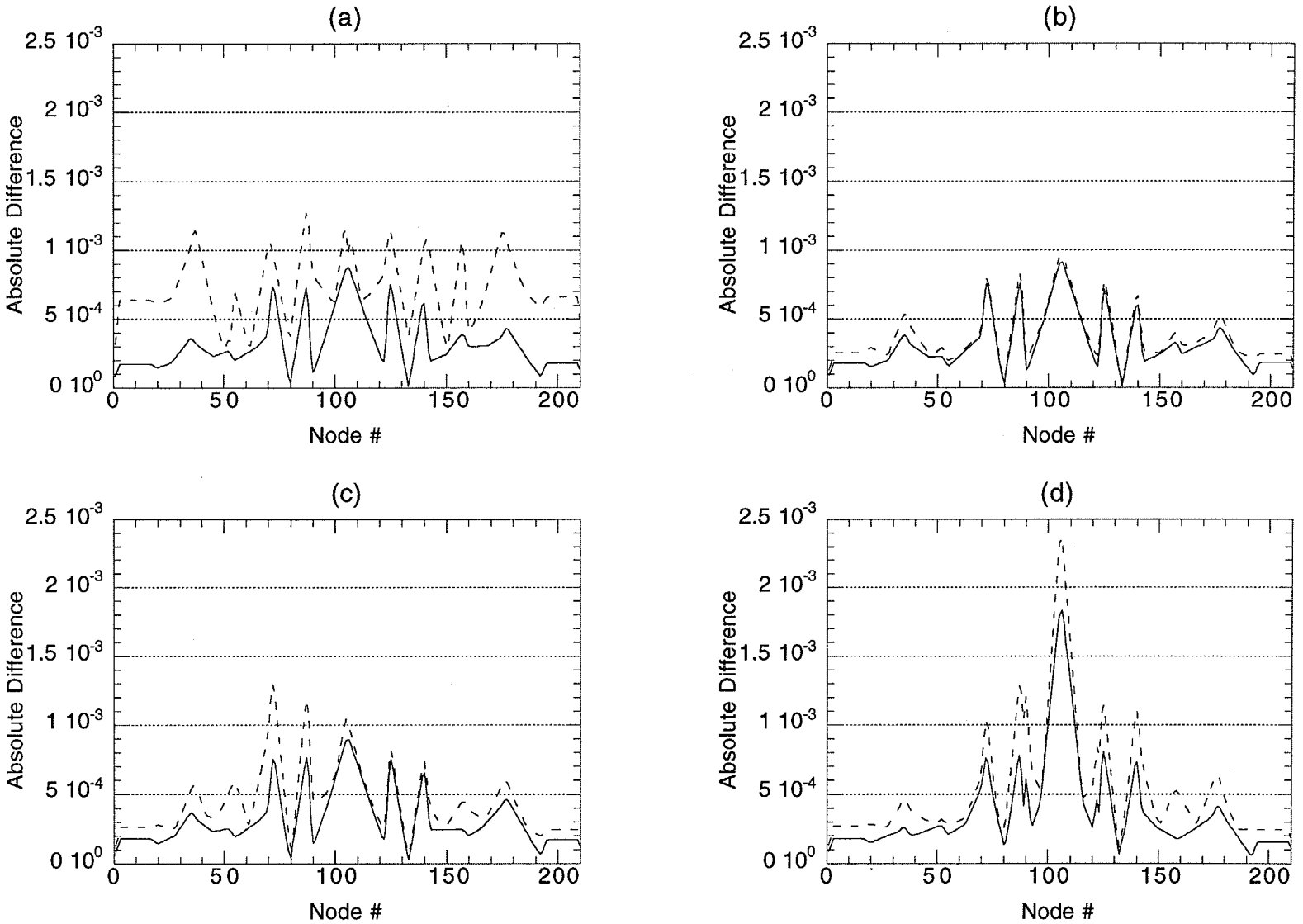

Fig. 52. Absolute difference in mode shape curvatures between the undamaged and damaged bridge for damage case (a) E-1, (b) E-2, (c) E-3, and (d) E-4 computed using the SET2 modal data: ———, two modes; - - - - - , all six modes.

For all four damage cases, the change in curvature computed using only two modes reached a peak at the immediate vicinity of damage (Node 106). Moreover, the peak was most distinct for damage case E-4. For the initial stages of damage (cases E-1 through E-3) the maximum change in curvature at the true damaged location is accompanied by smaller peaks in adjacent areas. When all six modes were included, the maximum change in curvature for damage cases E-1 and E-3 did not coincide with the actual location of damage. For damage cases E-2 and E-4 (see plots (b) and (d) of Fig. 52), the maximum change in curvature appears at the damaged region regardless of whether only two or all six modes are used in the calculation. Thus, when damage is not severe, inaccurate predictions may be made if modes not significantly affected by damage are included in the calculation of the change in curvature. Furthermore, the true location of damage, as shown by the maximum change in curvature, is most definite for extreme damage cases.

V. B. 2. Mode Shape Curvature Method Applied to Numerical Data

Similar analyses were done using numerically extracted data from three modes for damage cases A-1 through A-3 (see Fig. 53). The maximum curvature change for the two initial damage cases A-1 and A-2, plotted in (a) and (b), are not found in the region of damage (nodes 82 and 83) and thus, offer no clear indication of where damage resides. For damage case A-3, however, the maximum curvature difference is located in the proximity of node 82 (i.e., the correct damage location). Incidentally, a significant peak occurred adjacent to the damage region. Again, in a blind test it would not be obvious that these peaks are not associated with other damage locations. When plot (c) in Fig. 53, corresponding to damage case A-3 is compared to plot (d) in Fig. 51, corresponding to damage case E-4, it is seen that the changes in curvature for the analytical case are smaller in magnitude than those determined from the experimental data. The smaller changes in curvature associated with the analytical model are caused by the boundary condition specified in these models (neglecting the piers) and the fact that the cut in the web is smaller than that in the actual experiments.

Plots of the absolute difference in curvature for the final five damage cases, A-4 through A-8, and the alternate undamaged case A-9 are presented in Fig. 54. Accurate predictions for the damage location were made for cases A-4 through A-6 as shown in plots (a), (b) and (c). In each case, the change in curvature was maximum at the damaged region. Moreover, for damage case A-6, the two locations of damage (nodes 40 and 100) are evident by recognizing that the maximum differences in curvature simultaneously occur at these locations and these two differences are of almost equal magnitude.

Cases A-7 and A-8, plotted in (d) and (e) of Fig. 54, which involved intermediate levels of damage, did show positive signs of damage at the proper locations (Nodes 20 and 40, respectively) although the clarity was not as refined as that achieved when damage was more extreme (i.e., cases A-4 and A-5). Damage case A-9, which consisted of a modification of the original forcing function and not an incident of damage, resulted in inaccurate indications of damage as shown in Fig. 54(f) where changes in curvature larger than those associated with damage cases A-7 and A-8 are observed. The plot in Fig. 54(f) shows the threshold levels of curvature change that are needed to distinguish damage from random variations in the data analysis procedures. Thus, in the event that the excitation of the bridge is altered, the modes of vibration of the structure may be modified which can ultimately lead to faulty predictions of damage using this technique.

V. C. Change in Flexibility Method

Much of the research to date for damage assessment has focused on utilizing changes in the modal properties of a structure (i.e., resonant frequencies, damping values, and mode shapes). Variations in the structural parameters such as the stiffness and flexibility matrices, which can be derived from modal data, have not received nearly as much attention. One of the techniques for

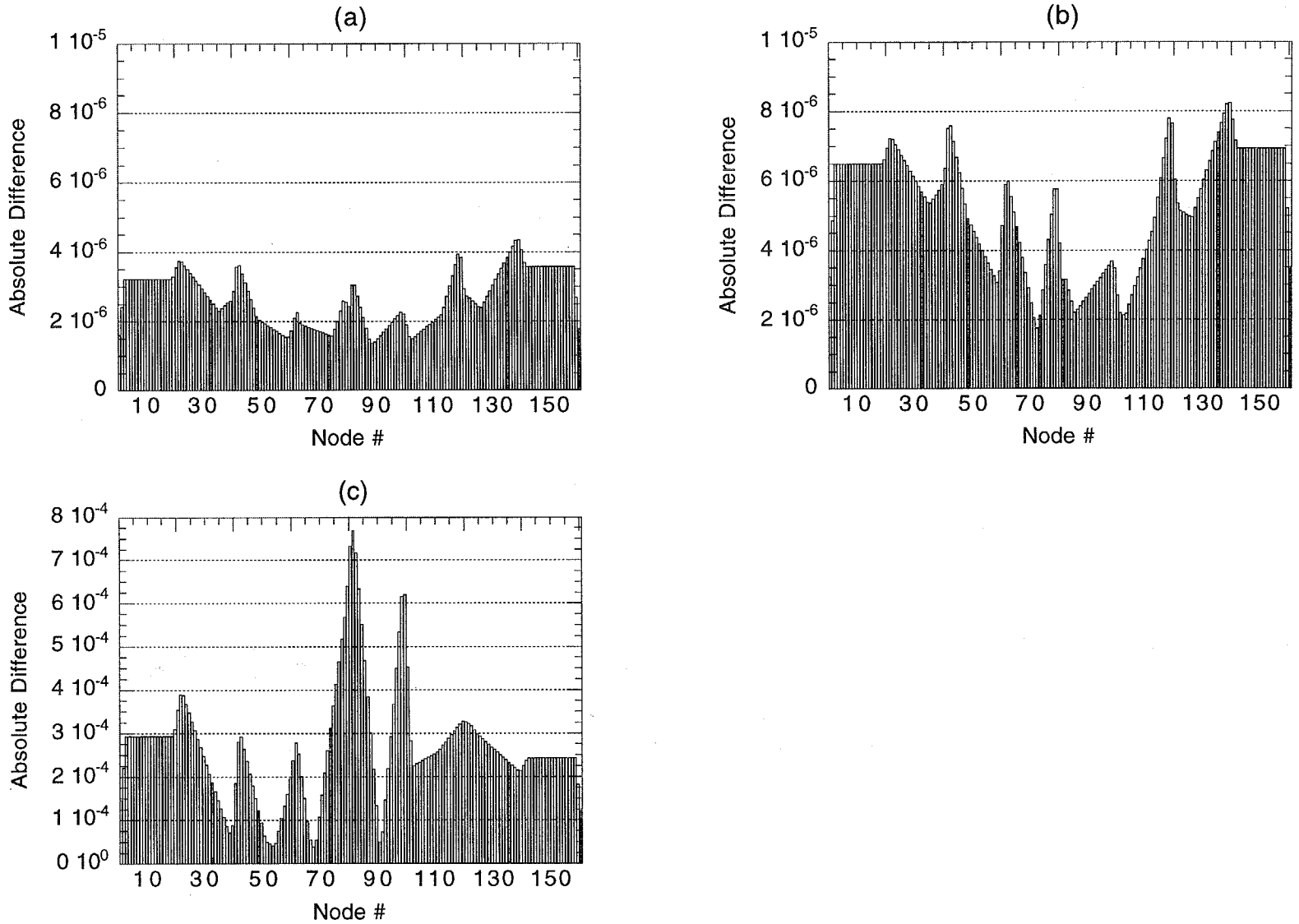

Fig. 53. Absolute difference in mode shape curvatures between the undamaged and damaged bridge for damage case (a) A-1, (b) A-2, and (c) A-3 computed using the SET3 modal data.

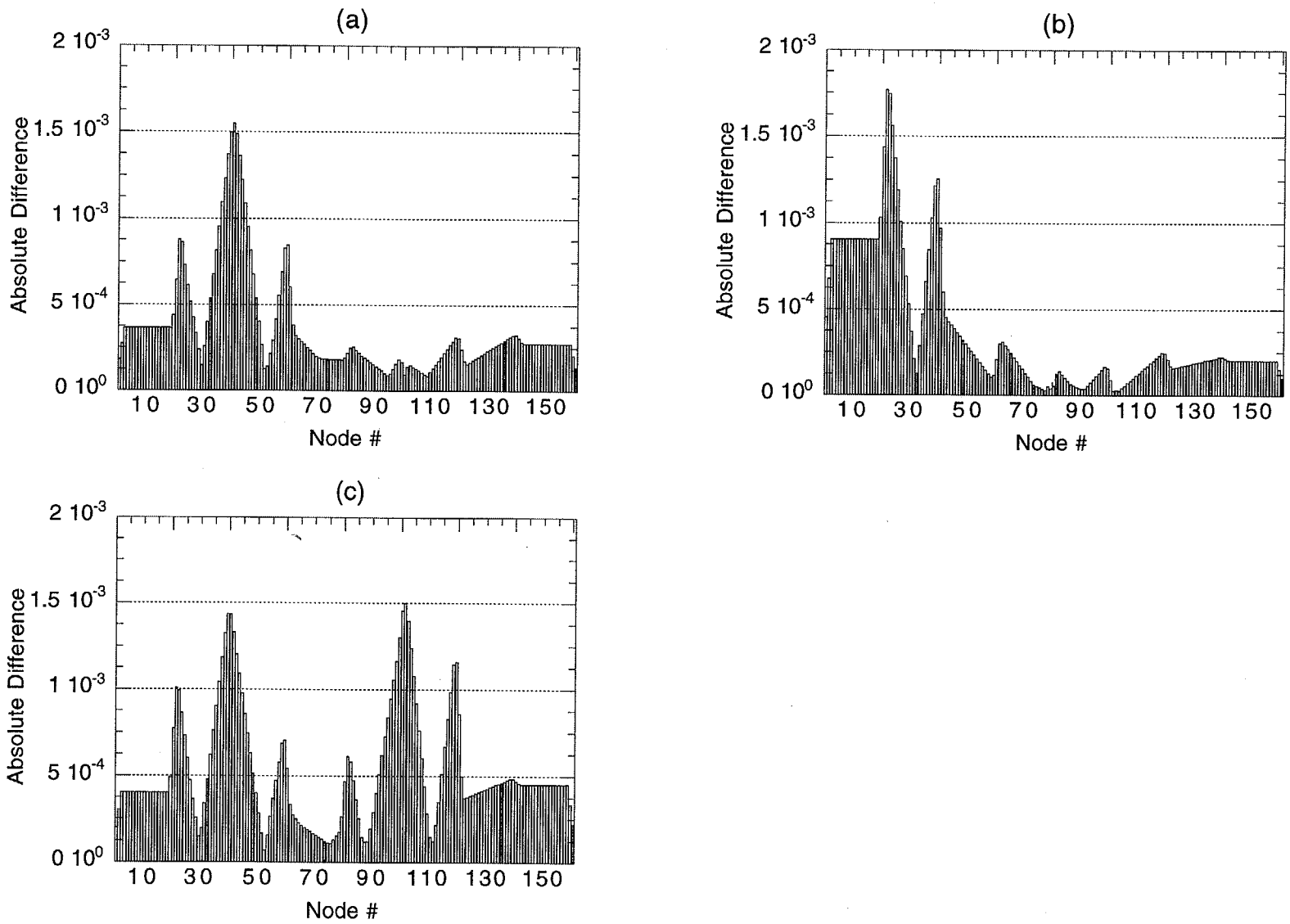

Fig. 54. Absolute difference in mode shape curvatures between the undamaged and damaged bridge for damage case (a) A-4, (b) A-5, and (c) A-6 computed using the SET3 modal data.

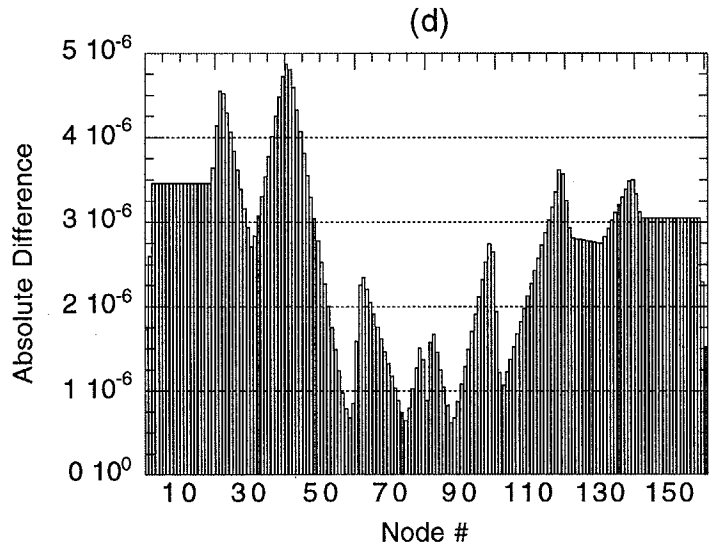

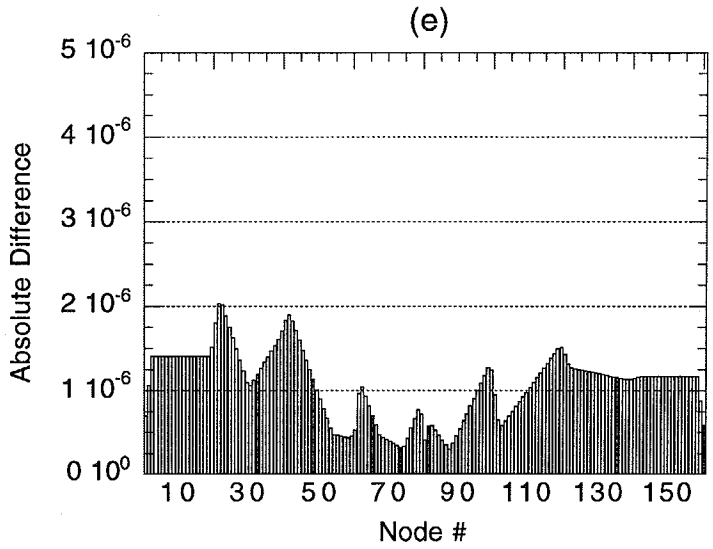

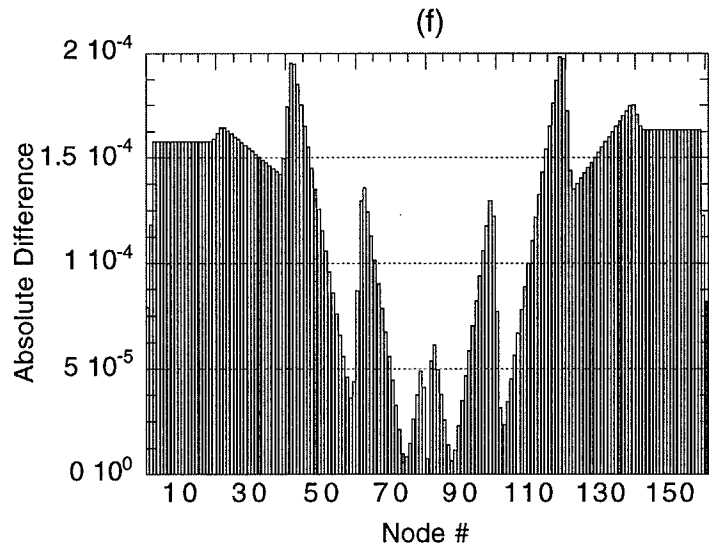

Fig. 54 (cont). Absolute difference in mode shape curvatures between the undamaged and damaged bridge for damage case (d) A-7, (e) A-8, and the alternate undamaged case (f) A-9 computed using the SET3 modal data.

detecting damage using changes in the structural parameters is the Change in Flexibility Method reported by Pandey and Biswas (1994). Differences in the flexibility matrix are used primarily to identify the presence and location of damage in a structure. Two significant advantages of this routine are (1) the flexibility matrix can be formulated from a few low frequency modes and (2) a measure of the change in flexibility can be readily estimated with simple matrix operations. The first advantage is fortunate because difficulties of measuring high frequency modes in the field require that a damage detection scheme be able to diagnose damage based solely on modal data for low frequency modes in order to be practical. Furthermore, the computational labor required to make the necessary damage diagnosis must be kept to a minimum.

In Pandey and Biswas (1994) the technique was tested using numerical modal data gathered from analytical beam models with varying boundary conditions and with experimental modal data gathered from a steel beam supported on elastomeric bearings. For the analytical study, damage was simulated by reducing the modulus of elasticity of an individual element of the analytical model. This approach allowed the extent and location of damage to be easily controlled by varying the decrease in the modulus of elasticity and the location of the damaged element. In each case of damage, the largest change in flexibility occurred at the location of damage. Furthermore, the magnitude of the flexibility change increased with reductions in the modulus of elasticity. In the experimental setup, the wide-flange beam had a splice at its midspan. Various levels of damage were inflicted by removing the flange splice plate and some additional rows of bolts in the web plate. In contrast to the analytical investigation, removal of different members of the splice reduces the moment of inertia at the splice location and not the modulus of elasticity. In either event, the bending stiffness of the beam is decreased and thus, damage is simulated. Again, the largest change in flexibility occurred in the damage vicinity (i.e., the splice location) and the flexibility change increased with reductions in the moment of inertia caused by removal of splice components.

As shown in Eq. 23, the flexibility matrix is more strongly influenced by the lower frequency modes. Therefore, an accurate representation of a structure's flexibility can be obtained with a limited number of low-frequency measured modes. Assuming that a modal survey has been performed on a structure while in an undamaged condition and then after some damage event, the flexibility matrices of the structure reflective of the two conditions can be formulated from the gathered modal data and then subtracted. Because of their inverse relationship, a decrease in stiffness should result in an increase in flexibility.

As discussed earlier, the calculation of the change in flexibility requires only a few steps. Flexibility matrices for the undamaged and damaged structures are first formulated from their associated modal data. The change in flexibility is then evaluated by subtracting the respective matrices and extracting the maximum absolute value from each column of the difference matrix as indicated by Eqs. 25 and 26. Remembering that a column of the flexibility matrix represents the deformed shape of the structure when a unit load is applied at the degree of freedom associated with the column, a vector containing the measures of flexibility change corresponds to the largest change in flexibility as a unit load is applied, in turn, to each degree of freedom. Theoretically, the greatest flexibility change should occur when the unit load is positioned at the damaged degree of freedom.

V. C. 1. Change in Flexibility Method Applied to Experimental Data

For the four cases of actual damage, E-1 through E-4, the change in flexibility computed using the modal data from SET1 is shown in Fig. 55. The results show that the damage location, element 82 between nodes 82 and 83, is not obvious until the final level of damage. At this stage, the flexibility change is approximately zero at the ends of the span and increases to a maximum at the damaged region (see plot (d)).

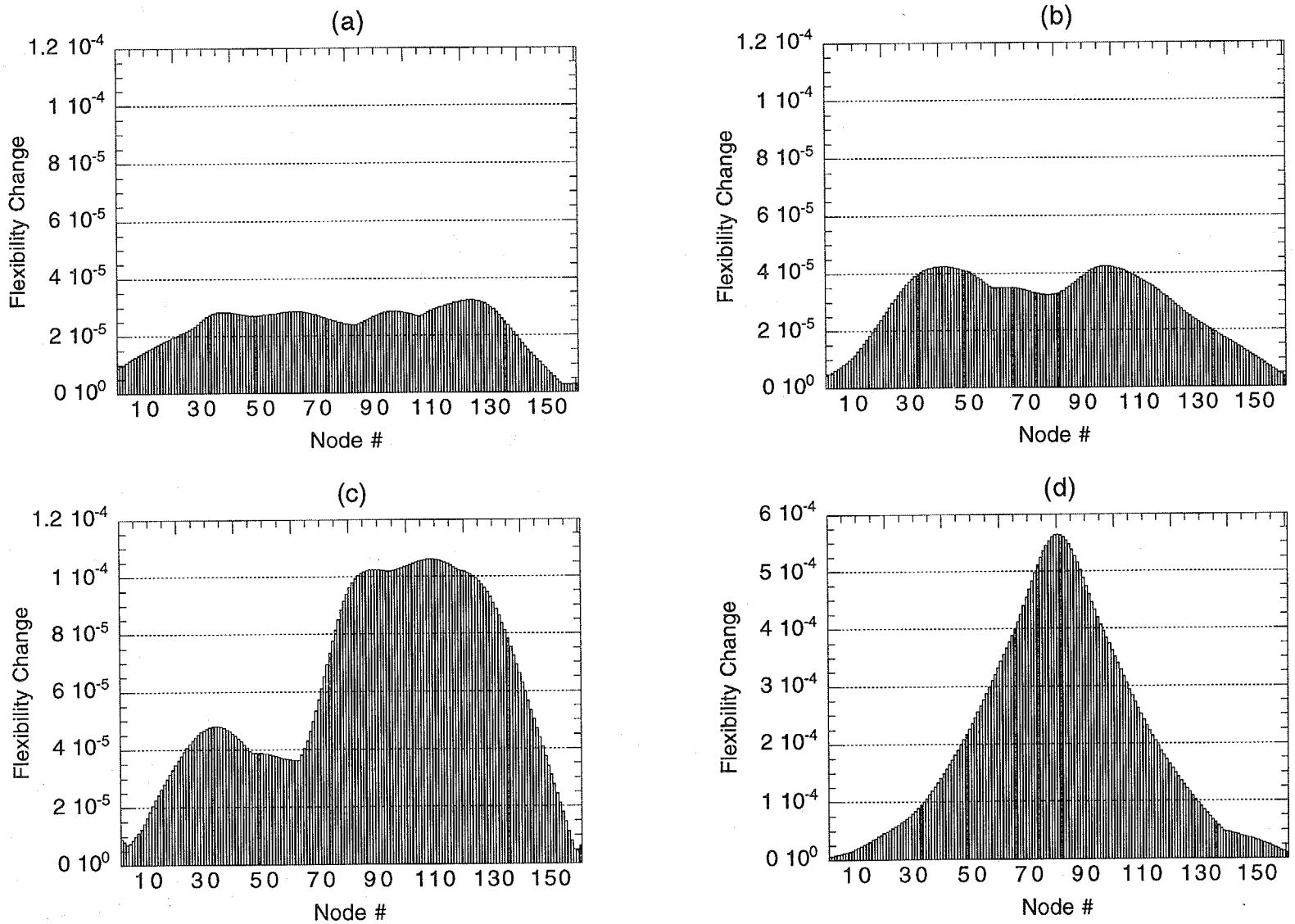

Fig. 55. Change in flexibility for damage case (a) E-1, (b) E-2, (c) E-3, and (d) E-4 computed using modal data from SET1.

The change in flexibility for damage cases E-1 and E-2 was essentially constant along the length of the span with no distinct peaks (see plot (a) and (b) of Fig. 55). Case E-3 reached a maximum in the vicinity of node 80 and remained constant up to node 120 (see Fig. 55(c)), thus confining the damage location to exist within a 40 foot range (approximately 1/4 the span length). The actual damaged location, element 82, does fall within the affected range.

Although the exact location of damage is not obvious, plots (a) through (c) of Fig. 55 show an increase in the change in flexibility as we advance from case E-1 to E-3. This increase in flexibility from stage to stage may be indicative of the growth of damage. Furthermore, there is an increase in the flexibility change from case E-2 to E-3 caused by severing half of the bottom flange. Since the bottom flange represents a primary component of the bending stiffness, decreasing its cross-sectional area by one-half significantly affects the flexibility. Thus, large increases in the change in flexibility from one damage case to another may reflect the propagation of damage to a main load carrying component.

The flexibility changes for damage cases E-1 through E-3 computed using the SET2 modal data are plotted in (a) through (c) of Fig. 56. Plots (a) and (b), corresponding to damage cases E-1 and E-2, did not give any indications of the true damage location regardless of whether two or six modes were used to calculate the flexibility matrices. However, the change in flexibility derived from only two modes shown in plot (c) did reveal a peak in the area of node 106 for damage case E-3. The change in flexibility obtained using all six modes did not give a clear damage location. For damage case E-4, the flexibility change is plotted in Fig. 57 as a function of the number of modes used. According to the figure, the maximum change in flexibility occurs in the vicinity of damage and converges using only one mode. From this figure it is obvious that damage affects mainly the first bending and first torsion mode. There is virtually no improvement in the change in flexibility when the final four modes are included in the calculation.

V. C. 2. Change in Flexibility Method Applied to Numerical Data

Figure 58 shows the resulting flexibility change for damage cases A-1 through A-3 obtained using the SET3 modal data. Inaccurate predictions for the location of damage were obtained for all three cases. According to the three plots of Fig. 58, the maximum change in flexibility occurs between the beam midspan and both ends of the span. Since the derivation of the flexibility matrix is directly dependent on the modal parameters, inaccuracies in the eigenvalues and eigenvectors will lead to errors in the flexibility matrix, thus, producing an erroneous change in flexibility. Although damage went undetected, some indication of the presence of damage is revealed by comparing the magnitudes of the three plots. As we progress from case A-1 to A-3 the change in flexibility increases indicating that the amount of damage has also increased.

The change in flexibility vectors computed from the SET3 modal data for damage cases A-4, A-5, and A-6 are shown in (a), (b), and (c) of Fig. 59, respectively. For all three cases, the maximum change in flexibility coincided with the damaged location. When damage occurred at two locations (case A-6), the change in flexibility at the location closer to midspan exceeded the change at the other damaged region (see Fig. 59(c)). However, the lack of a procedure to quantify changes associated with damage could lead one to believe that damage occurred in three locations for this case. Areas adjacent to the maximum bending moment region of the structure have been shown to experience a larger change in flexibility than regions positioned further away (Pandey and Biswas, 1994). This observation is also justified by comparing the change in flexibility presented in plots (a) and (b) of Fig. 59. Again, the results plotted in (a) which correspond to a damage location closer to midspan exceed those shown in plot (b). Thus, the method generates larger changes in flexibility when damage occurs in a region of large bending moment. Unsuccessful predictions were made for the alternate undamaged case A-9 in addition to the damage conditions A-7 and A-8 as shown in the three plots (d), (e), and (f) of Fig. 59.

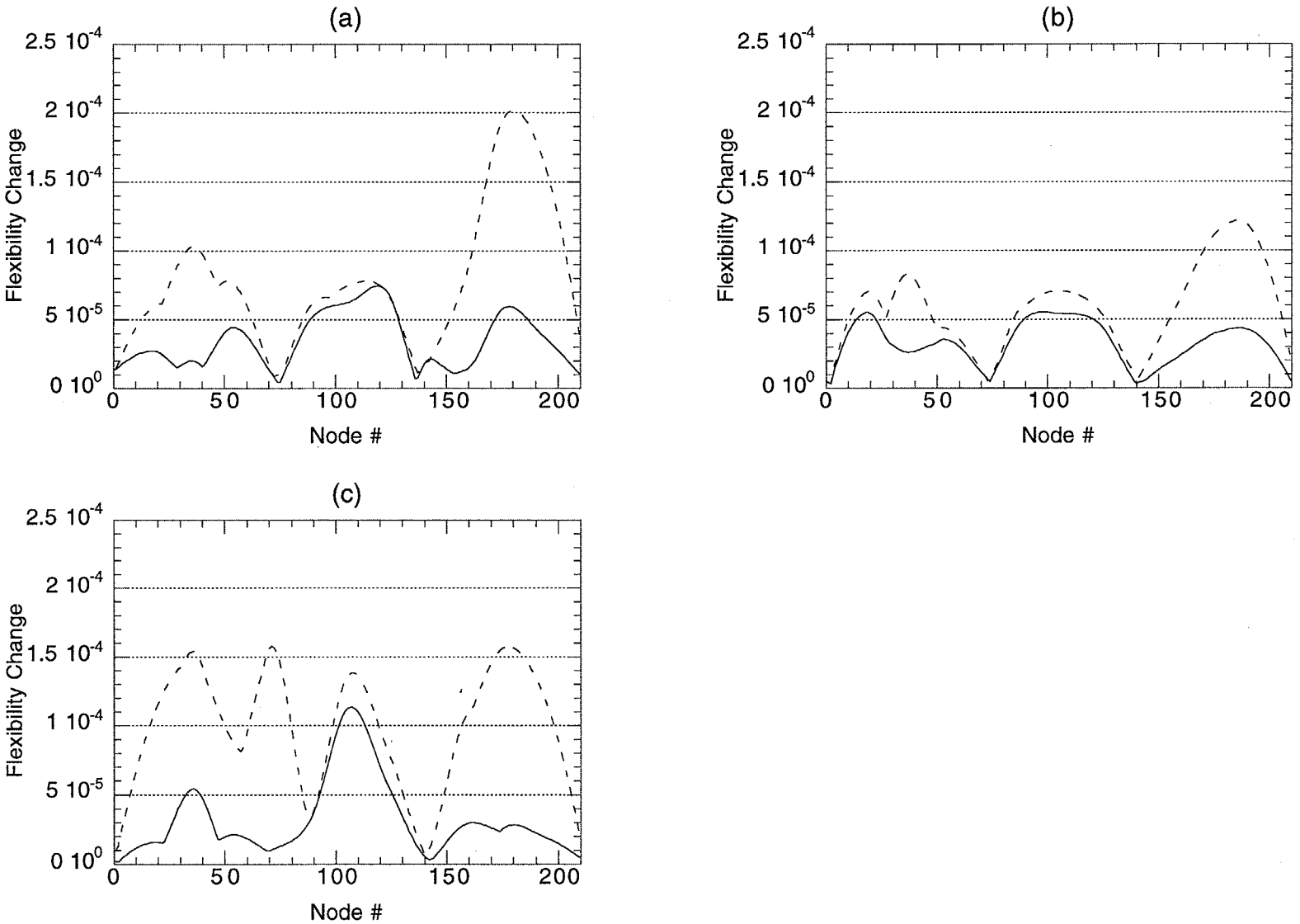

Fig. 56. Change in flexibility for damage case (a) E-1, (b) E-2, and (c) E-3 computed using modal data from SET2: ———,two modes; - - - - - , all six modes.

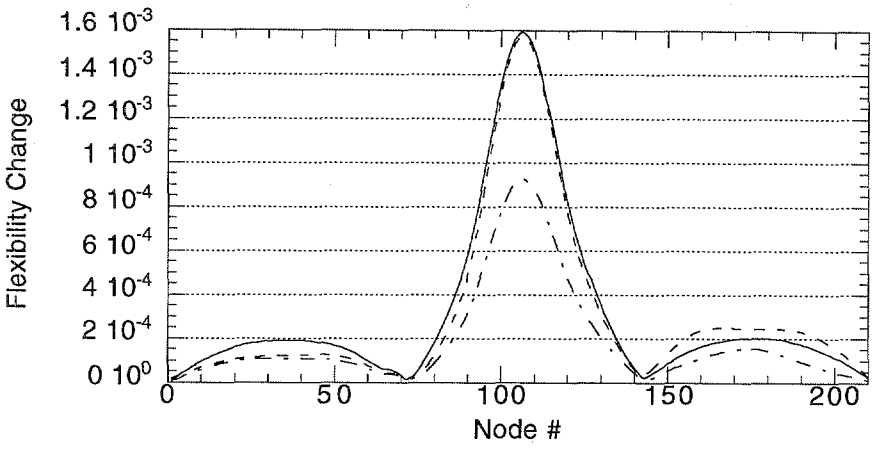

Fig. 57. Change in flexibility for damage case E-4 computed using the SET2 modal data as a function of the number of modes used: ·-·-·-·-·-·, one mode; ———, two modes; and - - - - -, six modes.

V. D. Change in Uniform Flexibility Shape Curvature Method

Two ways in which to portray a structure's flexibility is in terms of the uniform load flexibility vector and the unit load flexibility matrix. The uniform load flexibility (or uniform load surface) corresponds to the deflected profile of the structure obtained by simultaneously applying a unit load at each degree of freedom. Individual columns of the flexibility matrix correspond to the deflected shape of the structure as a unit load is placed at the particular degree of freedom associated with that column. Hence, column 1 represents the structure's deflected shape with a unit load positioned at degree of freedom one, column 2 represents the structure's deflected shape with a unit load positioned at degree of freedom two, and so on. By superposition, the uniform load surface is the sum of individual columns of the unit load flexibility matrix. Knowing the flexibility of the structure, before and after damage, the question arises if the change in curvature between the pre-damage flexibility and post-damage flexibility can be used to locate and possibly estimate the extent of damage.

Zhang and Aktan (1995) developed a damage detection scheme by combining the basic concepts of the Mode Shape Curvature Method and the Change in Flexibility Method. To demonstrate the technique, Zhang and Aktan used a two-dimensional grid model of a 3-span continuous steel stringer bridge. The grid model was first calibrated to match the resonant frequencies and mode shapes from an experimental modal test. Following the calibration, five states of damage were simulated by reducing the modulus of elasticity by increasing percentages at midspan of one of the girders. For each case of damage, the curvature difference of the structure's uniform load surface from undamaged to damaged condition was greatest at the affected area. Furthermore, there was an increase in the curvature difference for each decrease in the modulus of elasticity. The authors also show that direct comparison of the uniform load surface, before and after damage, reveals the location of damage only for extreme levels of damage.

Assuming that modal data had been collected for the structure in an undamaged condition and after damage, it is possible to derive a pre- and post-damage flexibility matrix. Recall that each column of the flexibility matrices contains a set of coordinates corresponding to the deflection profile of the structure caused by a unit load at the associated degree of freedom. The uniform load flexibility is them obtained by multiplying the flexibility matrix times a vector containing one at each entry with the same column dimension as the flexibility matrix or, equivalently, by summing individual

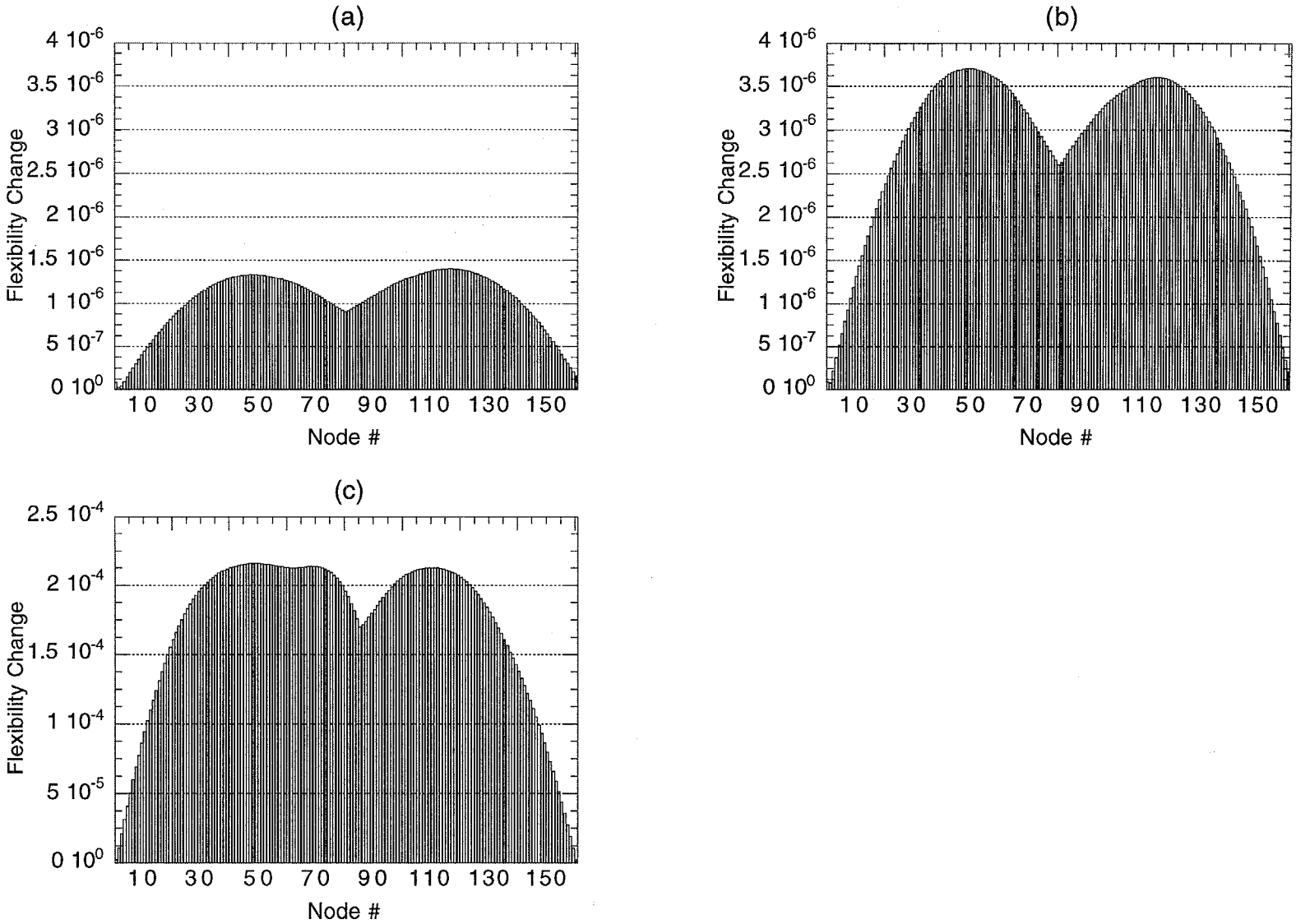

Fig. 58. Change in flexibility for damage case (a) A-1, (b) A-2, and (c) A-3 computed using modal data from SET3.

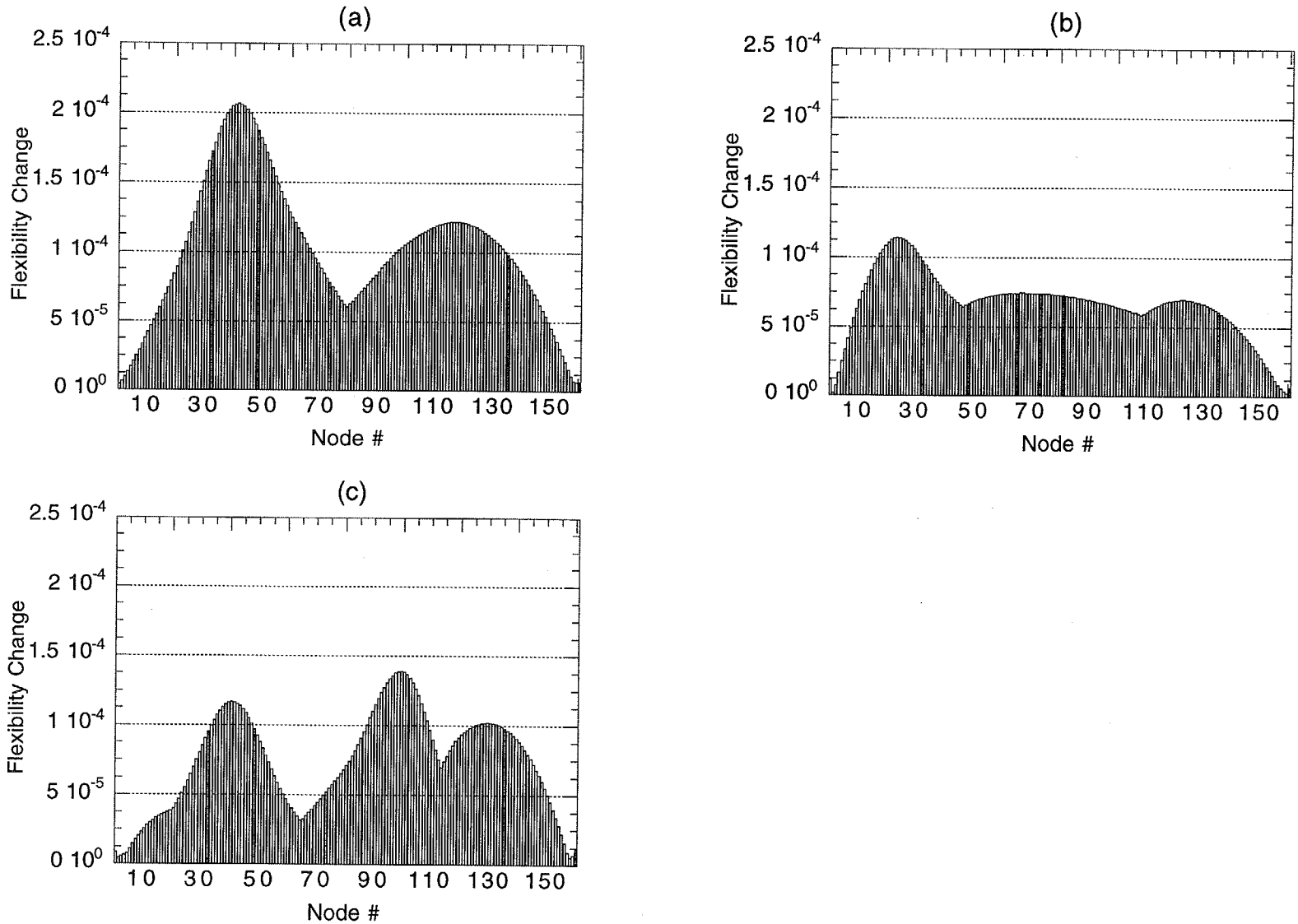

Fig. 59. Change in flexibility for damage case (a) A-4, (b) A-5, and (c) A-6 computed using modal data from SET3.

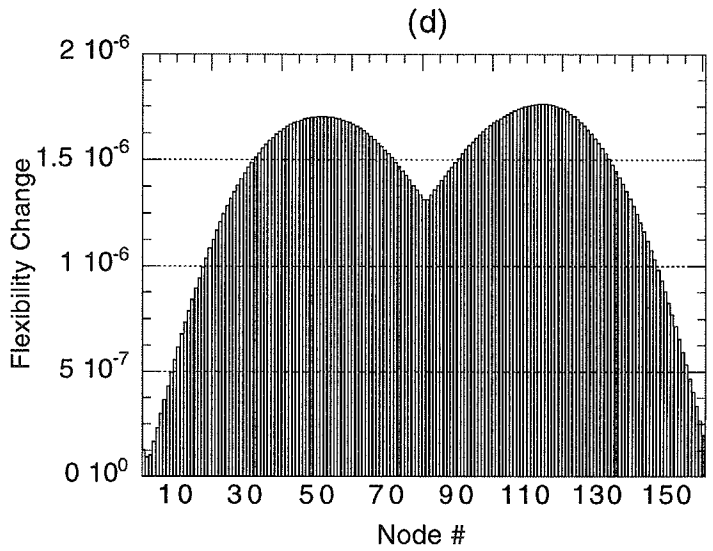

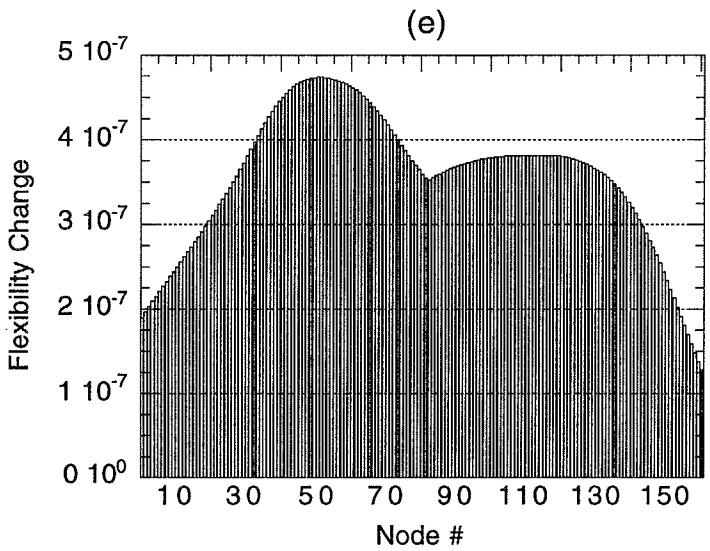

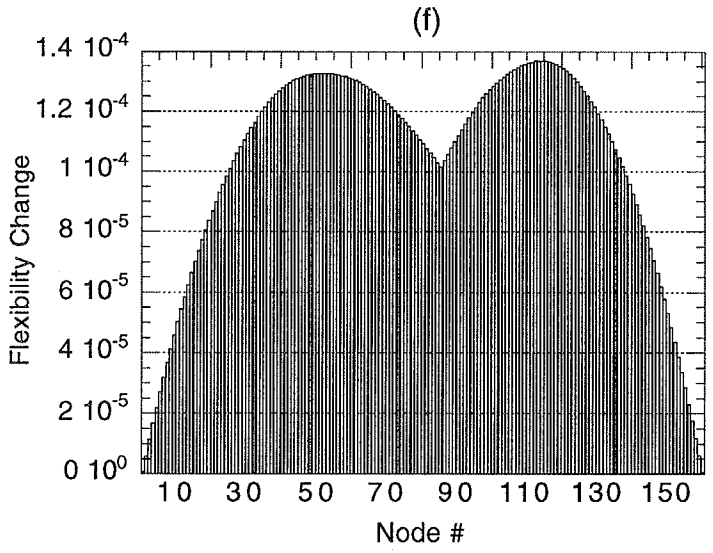

Figure 59 (cont). Change in flexibility for damage case (d) A-7, (e) A-8, and the alternate undamaged case (f) A-9 computed using modal data from SET3.

columns of the unit flexibility matrix. Next, the absolute value of the curvature change for each unit load flexibility is computed by fitting a cubic polynomial to the flexibility shape and then these shapes are summed. As in the Mode Shape Curvature Method, a loss of cross-section (i.e., stiffness reduction) should result in an increase in curvature.

This method for determining the curvature change differs slightly from the approach taken by Zhang and Aktan (1995) in that the absolute value of the curvature change is first computed and then accumulated. In Zhang and Aktan (1995), the curvature change is first accumulated and then the absolute value is taken. In order to switch the order in which the summation and absolute value were performed, each unit load flexibility shape needed to be considered, which required a larger amount of computation. Although this adjustment was minor, a significant improvement in the results was achieved.

V. D. 1. Change in Uniform Flexibility Shape Curvature Method Applied to Experimental Data

The absolute difference in curvature of the unit load flexibility shapes obtained from the SET1 modal data for damage cases E-1 through E-4 are shown in Fig. 60. According to the figure, the true damage location is unclear until the third state of damage. At the second level of damage (case E-2), the greatest curvature difference occurs at node 96 and then at node 82, the correct damage location. From (c) and (d) of Fig. 60, the largest peak of the absolute difference occurs at the damaged location. Comparison of plots (a) and (b) shows relatively no difference between the magnitudes of the curvature change. This result is expected because the web does not significantly influence the bending stiffness of the girder. However, the transition from damage case E-2 to E-3 did cause a large jump in the extent of the change in curvature. An even larger jump occurred from the damage case E-3 to E-4 transition. Recall that the final two damage cases involved severing the bottom flange of the girder. Because bending is primarily resisted by the girder flanges and the concrete deck, damage to these components decreases the flexural stiffness by a larger proportion. Thus, by inspecting the magnitude difference in the change in curvature between two incidents of damage it may be possible to determine if damage has progressed into a main load carrying member. Again, it can be seen that in Fig. 60(c) that without a quantitative method for assessing if changes in curvature are indicative of damage, one could be mislead to believe that damage occurred in two locations.

Figure 61 presents the results for damage cases E-1 through E-3 that were determined using the modal data from SET2. The contribution of all six modes were included in the computation of the change in curvature presented in plots (a) through (c). As shown in these three plots, the change in curvature algorithm failed to identify the damage location. The maximum difference in curvature for damage cases E-1 through E-3 occurred in the vicinity of nodes 124, 36, and 71, respectively, none of which represent the actual location of damage. The change in curvature computed for damage case E-4 is plotted in Fig. 62. Again, the contribution of all six modes was included in the calculation. For this case, the algorithm did succeed in identifying the true location of damage as shown by the peak at node 106.

V. D. 2. Change in Uniform Flexibility Shape Curvature Method Applied to Numerical Data

Damage cases A-1 and A-2 went undetected as shown in (a) and (b) of Fig. 63 using the SET3 collection of modal data. Peak values of the curvature difference occurred at two incorrect locations: the quarter points of the span. When damage case A-3 was induced, however, the largest curvature change occurred in the vicinity of damage (see Fig. 63(c)). A notable change also occurred approximately 20 feet from the damage location.

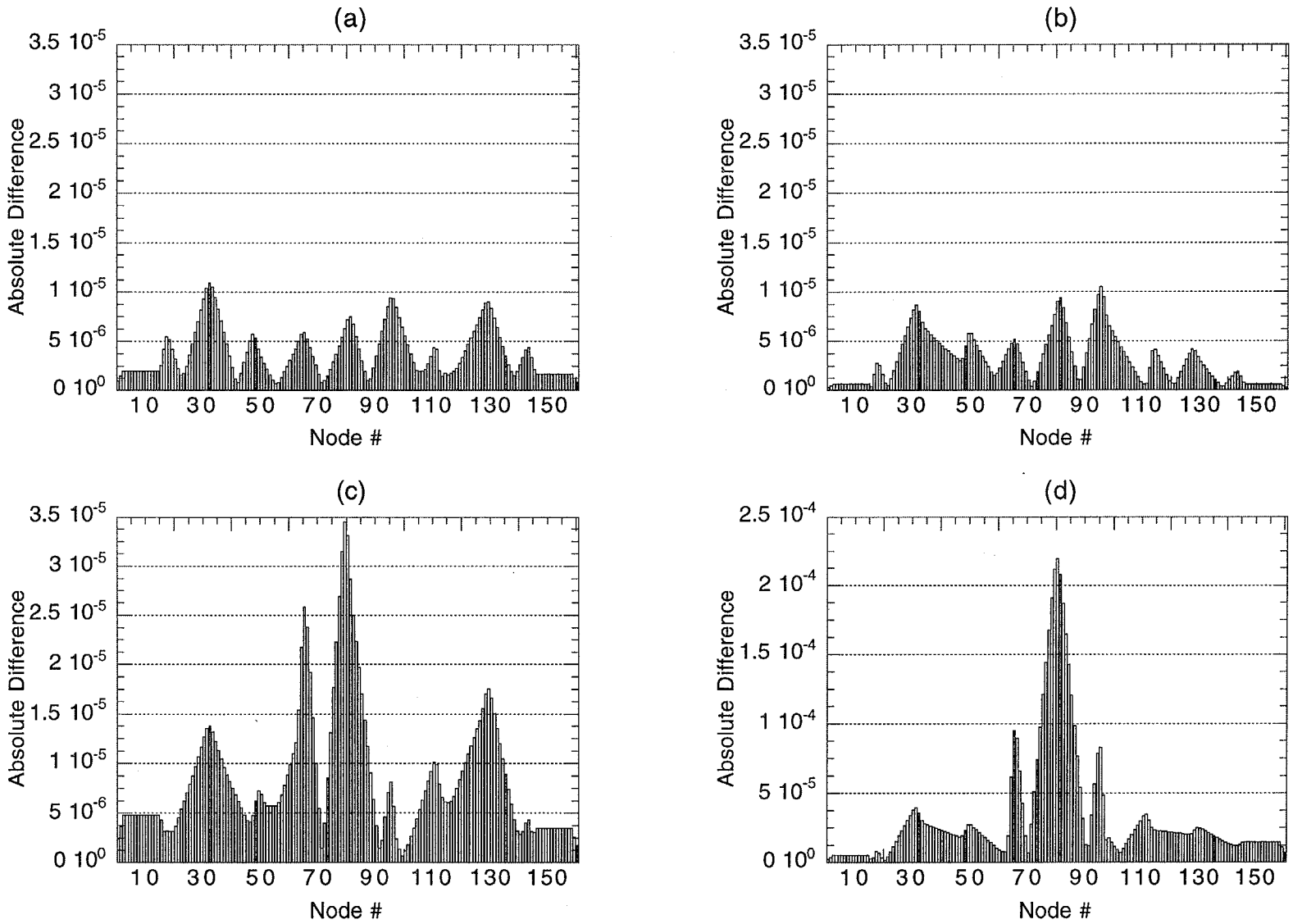

Fig. 60. Absolute difference in uniform flexibility shape curvatures for damage case (a) E-1, (b) E-2, (c) E-3, and (d) E-4 computed with modal data from SET1.

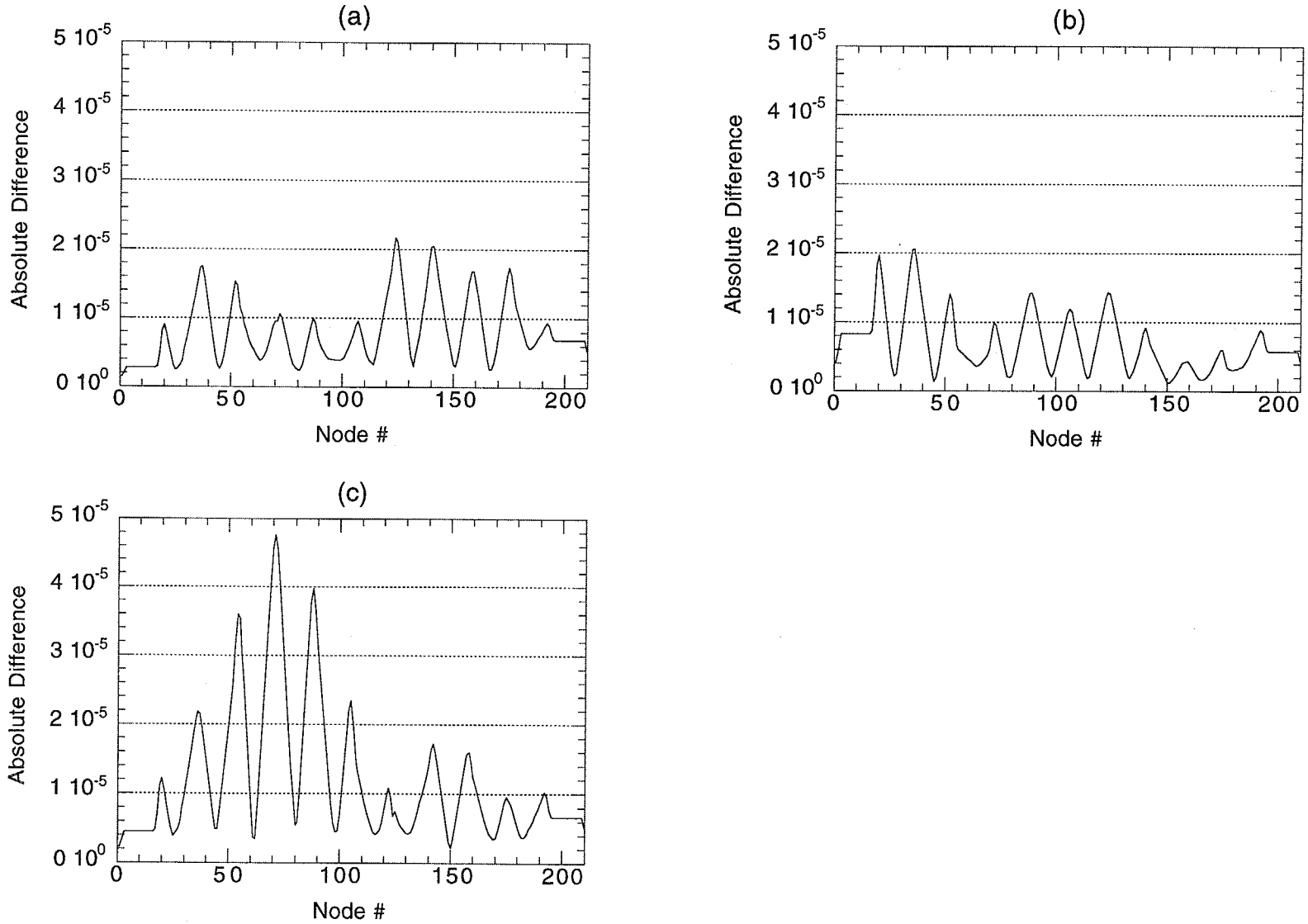

Fig. 61. Absolute difference in uniform flexibility shape curvatures for damage case (a) E-1, (b) E-2, and (c) E-3 computed with modal data from SET2.

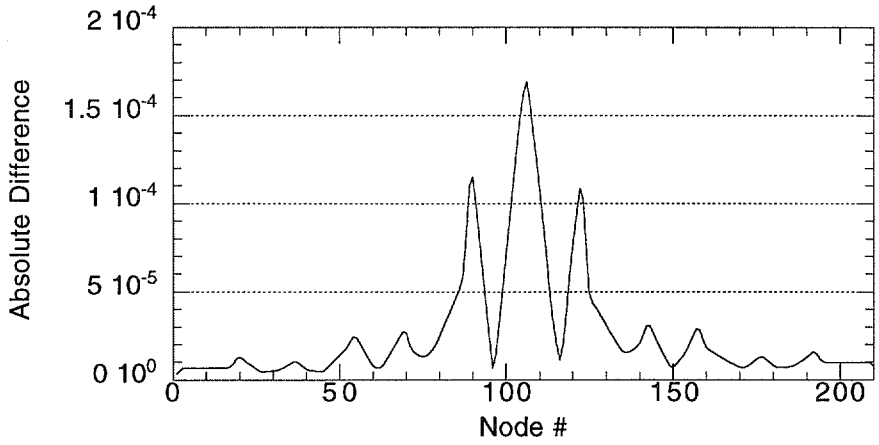

Fig. 62. Absolute difference in uniform flexibility shape curvatures for damage case E-4 obtained via modal data from SET2.

From (a) and (b) of Fig. 64, the maximum change in curvature of the unit load flexibility shapes occur at the quarter point and at an eighth point, respectively. These locations correspond to the exact areas of damage for cases A-4 and A-5. Comparison of these two plots also shows that the magnitude of the curvature change was greater when the damage was positioned closer to the end of the span. This result is expected because the damage at the quarter point is near a splice plate, which under dead load represents an inflection point (i.e., transition from positive to negative moment or vice versa). The damage positioned closer to the end of the span is in a region of large negative moment. Previous studies show that the curvature change is greatest when the damage occurs in high stressed areas such as interior supports of continuous beams.

Multiple damage was identified accurately as shown by the locations of the two maximum peaks in plot (c) of Fig. 64. Note that the size of the curvature change at the damage location nearer to midspan exceeded the difference at the quarter point. Again, the damage closer to midspan is in a higher stressed region (i.e., large positive moment) and will therefore experience larger changes in curvature. Although the magnitude of the change in curvature for the alternate undamaged case A-9 is higher than for damage case A-7, plots (d) and (f) of Fig. 64 are essentially identical. In both damage cases, the algorithm produced ambiguous results. Plot (e) of Fig. 64 did show the maximum change in curvature in the vicinity of damage. These results show that detecting the location of damage in areas of low stress becomes even more difficult when the degree of damage is not severe. Moreover, it is easier to detect damage in higher stressed areas.

V. E. Change in Stiffness Method

In Zimmerman and Kaouk (1994), a Minimum Rank Update Theory (MRPT) was developed for locating and estimating the degree of damage in a structure. The method was applied successfully to two- and three-dimensional trusses. First, a FEM of the test structure is constructed with no effort made to match the measured modal parameters. Next, the FEM is refined and calibrated to obtain an updated model capable of reproducing the vibrational parameters measured experimentally. When this is accomplished, the analytical model is believed to represent the stiffness of the actual structure and therefore is considered capable of simulating the structure's actual behavior. No modification is made to the original mass distribution of the structure since the modeling errors is assumed to be strictly related to the stiffness. Damage is then introduced to the calibrated model by removing and/or reducing the modulus of elasticity of various members of the truss. Resonant frequencies and mode shapes associated with the damaged condition together with the original mass, stiffness, and damping matrices of the structure are then used to compute a

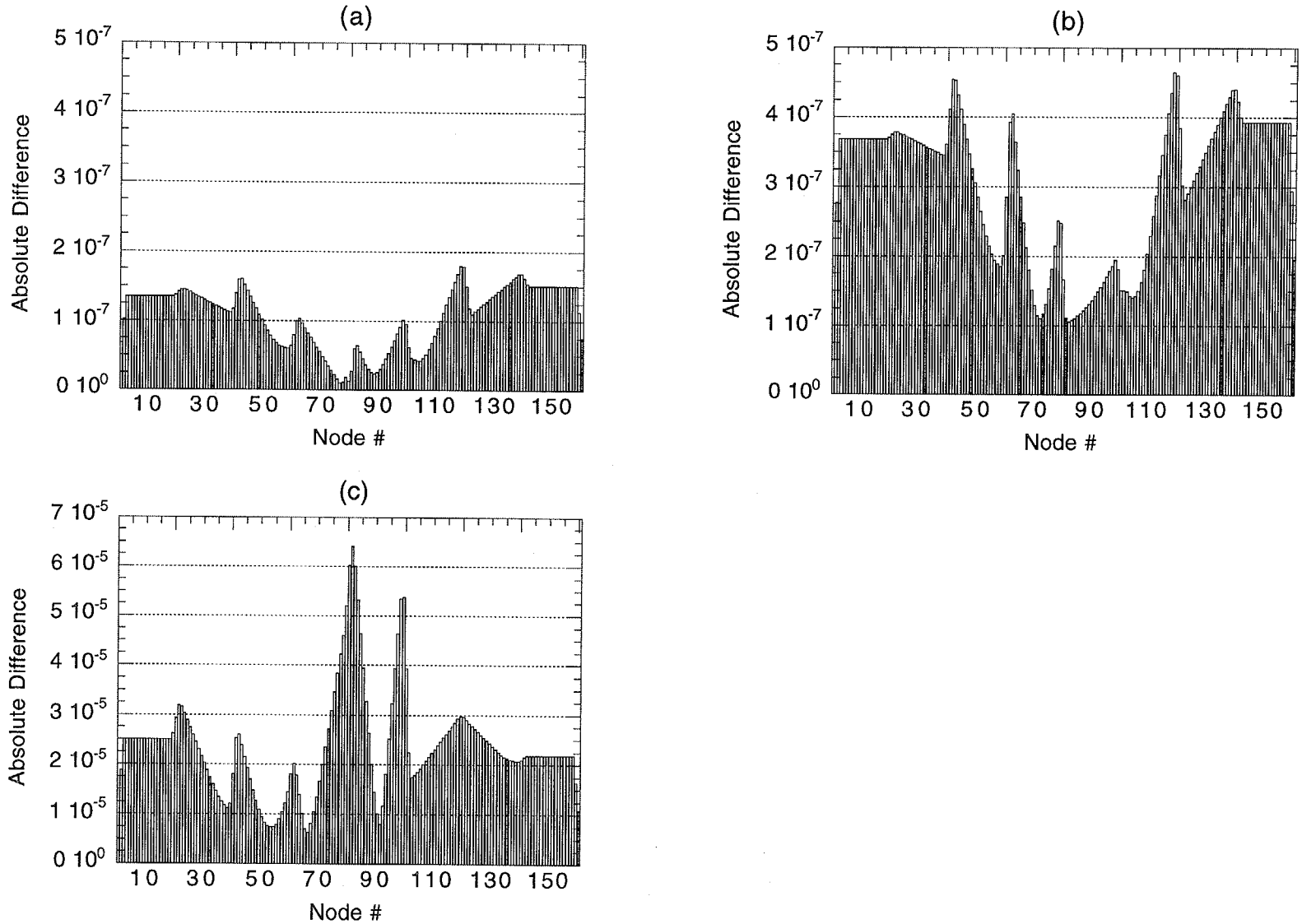

Fig. 63. Absolute difference in uniform flexibility shape curvatures for damage case (a) A-1, (b) A-2, and (c) A-3 computed with modal data from SET3.

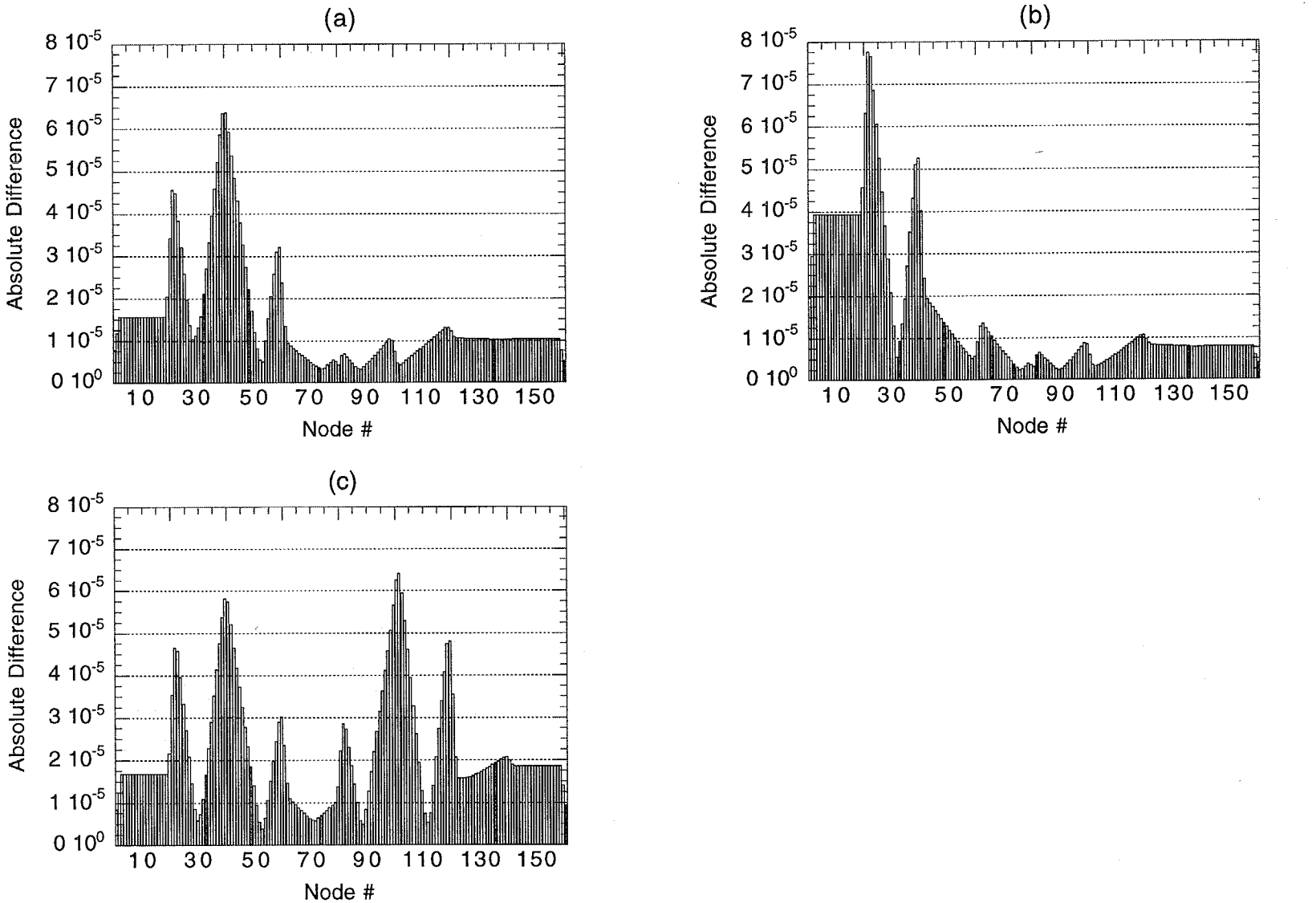

Fig. 64. Absolute difference in uniform flexibility shape curvatures for damage case (a) A-4, (b) A-5, and (c) A-6 computed with modal data from SET3.

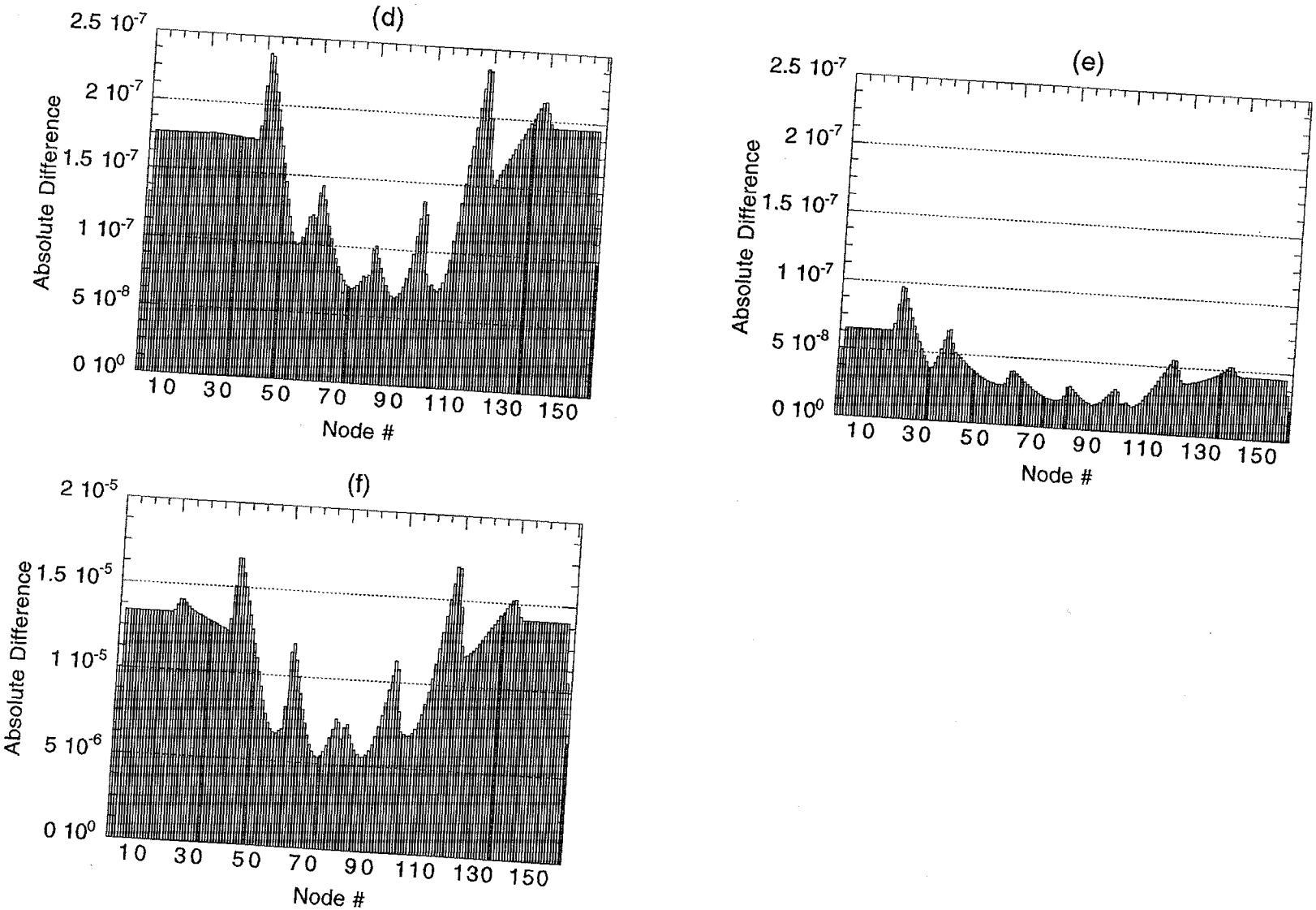

Fig. 64 (cont). Absolute difference in uniform flexibility shape curvatures for damage case (d) A-7, (e) A-8, and the alternate undamaged case (f) A-9 computed with modal data from SET3.

damage vector from Eq. 33. Alternatively, perturbations in the structure's mass and stiffness matrices can be substituted for the original matrices and the damage vector can be computed using Eq. 33. However, calibrated models of the damaged structure are required to obtain these perturbation matrices. According to the damage array, the largest values occur at the degrees of freedom associated with the strut that has been removed or reduced in stiffness.

In Kaouk and Zimmerman (1994), the MRPT was augmented to include the case when no original analytical model is available. Using only pre- and post-damage modal properties of a structure, the technique is able to approximate the location and extent of damage in two- and three-dimensional truss-like structures. The technique was exercised using both numerical and experimental modal properties. First, a baseline representation of the mass and stiffness of the structure is obtained using the pre-damage modal parameters. With the healthy model determined, the damage array is then computed utilizing the post-damage modal properties. Although the results were shown favorable, the authors conclude that the damage assessment algorithms perform better when an original analytical model is available.

In this study, damage is assumed to affect only the stiffness properties of the structure. The analysis is further simplified in that stiffness matrices representative of the structure before and after damage are formulated from a set of pre- and post-damaged modal data generated experimentally or numerically. Hence, no attempt was made to match the vibrational response of an analytical model to a set of measured resonant frequencies and mode shapes. By utilizing the connectivity of the sensor locations it is possible to improve the stiffness matrix to one that is more physically meaningful. Each node of the damage detection model is first assumed to be connected to its adjacent node or nodes. Under this assumption, no relationship exists between the node and those positioned further away. Thus, stiffness coefficients off the tri-diagonal can be eliminated and forced to zero. Following this modification, the reduced pre- and post-damage stiffness matrices are subtracted and multiplied by the damaged mode shape to obtain a damage vector. This approach resulted in improved results as opposed to using fully populated stiffness matrices.

Derivation of the stiffness matrix from modal data requires two important criteria to be met. Ideally, the number of extracted modes should equal the number of sensors and all modes should be measured or at least the high frequency modes. Considering that the modal data extracted for this investigation consisted solely of low frequency modes and the number of modes recorded was less than the number of sensors, the two requirements for obtaining an accurate representation of the stiffness matrix were not met in their entirety.

V. E. 1. Change in Stiffness Method Applied to Experimental Data

The damage vector computed using six modes of the SET1 modal data for the four damage cases E-1 through E-4 is plotted in Fig. 65. Based on the plots, the algorithm was unable to identify damage until the bottom flange was entirely severed (i.e., damage case E-4). At intermediate cuts, the damage location algorithm failed to detect the affected area.

The first singular vector of scaled damage matrix for damage cases E-1 through E-4 determined using the SET2 modal data are shown in plots (a) through (d) of Fig. 66. This normalization of the damage vector was done to account for stiff areas near the interior supports of the bridge. Otherwise, the largest peaks of the damage vector would always reside at the interior supports. All four plots show a peak in the vicinity of damage when only the first bending and first torsional modes are used. When all six modes were included in the calculation, the algorithm generated ambiguous results for damage cases E-1 through E-3 and the peak at the damage location for damage case E-4 was not as distinct. Once more, contributions of unaffected modes appear to be disrupting the performance of the algorithm.

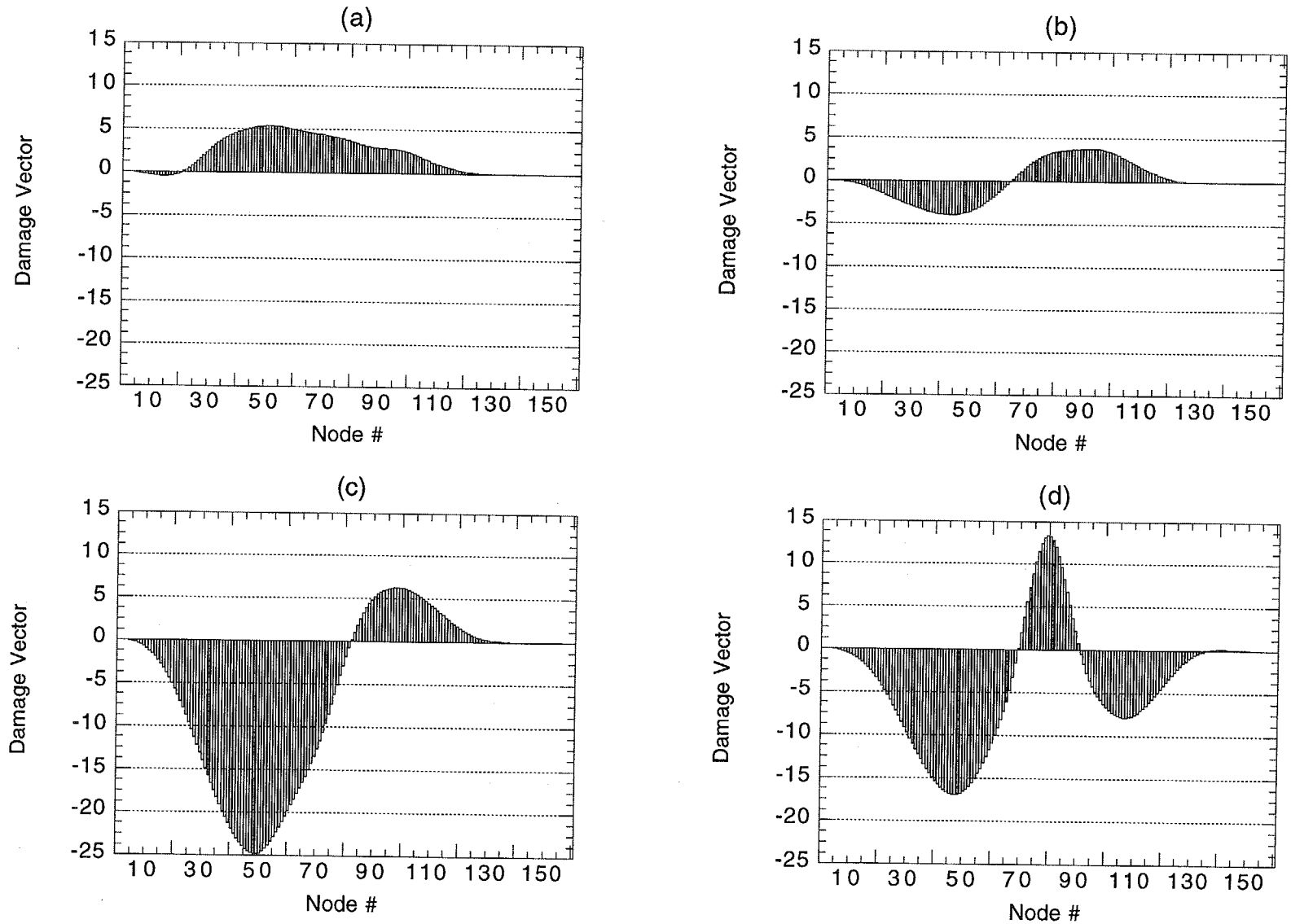

Fig. 65. Damage vector calculated for damage case (a) E-1, (b) E-2, (c) E-3, and (d) E-4 using the modal data from SET1.

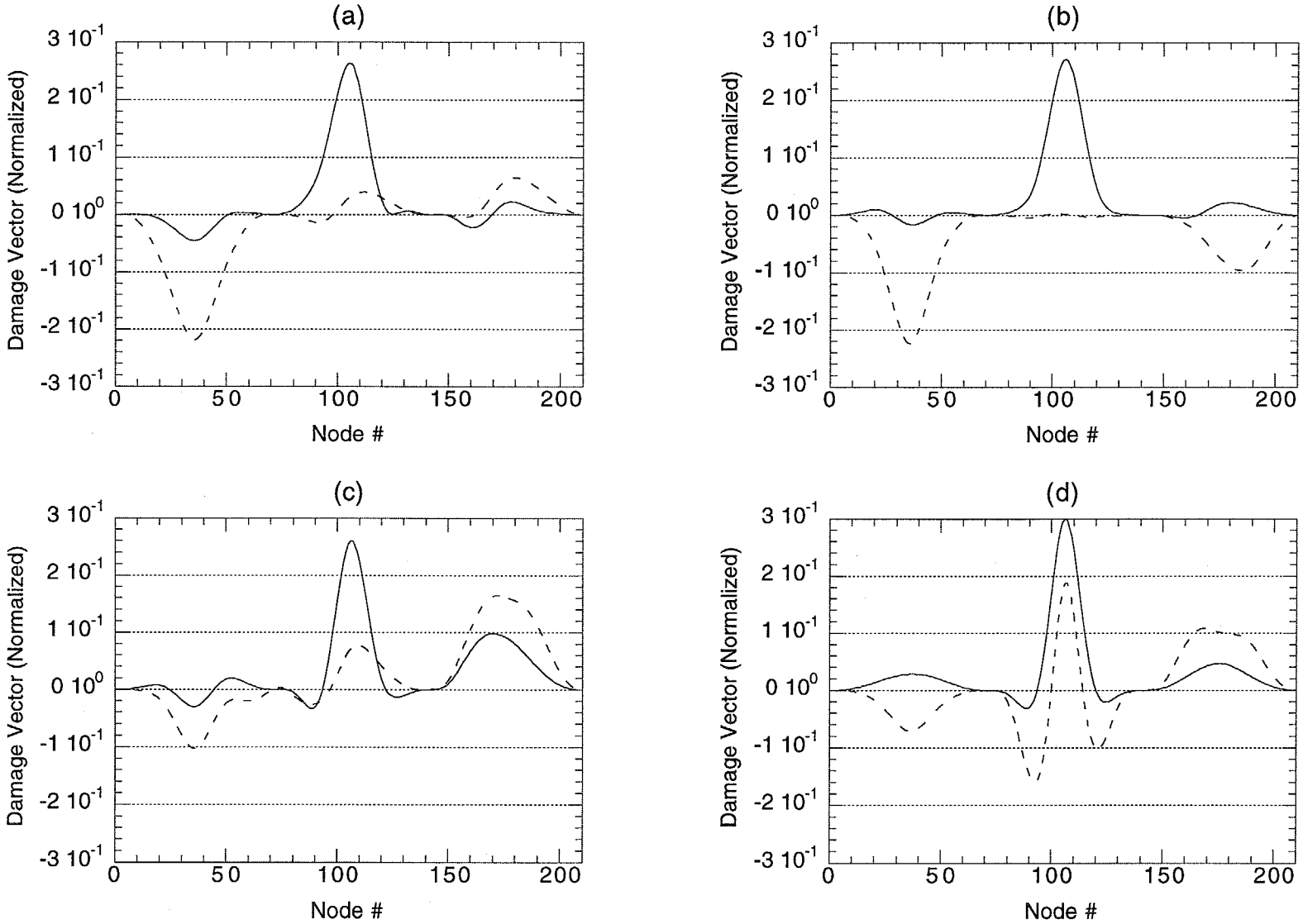

Fig. 66. First left singular vector of the normalized damage matrix for damage case (a) E-1, (b) E-2, (c) E-3, and (d) E-4 calculated using the modal data from SET2: ——— , two modes; - - - - - , all six modes.

V. E. 2. Change in Stiffness Method Applied to Numerical Data

Figure 67 displays plots of the damage location vector for the three damage cases A-1, A-2, and A-3 computed using the SET3 modal data. For all three cases, the damage vector failed to locate the damage. The damage vector for case A-3 showed large values close to node 50 which is about 30 feet from the true damage location. Compared to cases A-1 and A-2, the magnitude of the damage vector for case A-3 is extremely large. This occurs because the finite element model did not produce changes in the modal properties of the structure until the bottom flange was completely severed.

The damage vector was able to identify the exact location of damage for case A-4 (Fig. 68). For case A-5, the predicted location was about 5 feet away from the actual damaged area. Hence, the node numbers at which damage was clearly shown for damage cases A-4 and A-5 were 40 and 25, respectively (see plots (a) and (b) of Fig. 68). For damage case A-6 (see plot (c) of Fig. 68), the largest positive peaks of the location vector occurred at nodes 40 and 100 which represent the damaged nodal locations exactly. Damage cases A-7 and A-8 remained undetected as shown in plots (d) and (e). A positive peak occurred at node 100 for damage case E-9, which is misleading since no damage is present (view plot (f)).

VI. SUMMARY AND CONCLUSIONS

A study was undertaken to compare five damage identification methods that have been proposed in the technical literature for bridge applications. This comparison was accomplished with experimental data from the I-40 Bridge over the Rio Grande in Albuquerque, NM, and numerically generated obtained data from finite element simulations of the same bridge. Tests performed to obtain the experimental modal data from the bridge in an undamaged and in various damaged conditions are summarized in Farrar, et al. (1994). Development of the finite element models used in the numerical study is summarized in Farrar, et al. (1996). After benchmarking a finite element model against measured modal data from the I-40 Bridge in its undamaged and damaged condition, numerical studies were performed to further evaluate the various damage detection techniques when they were applied to other damage scenarios.

In choosing the damage identification methods to be compared, the authors have limited their study to those requiring only measured responses before and after damage as opposed to those requiring a correlated FEM. Although the FEMs in this study were benchmarked against measured modal data, this benchmarking was done only to verify that the models were accurately predicting the dynamic response of the structure. Model-updating damage identification methods, which require correlated FEMs, were not used in this study because it is the author's opinion that it would be impractical to develop correlated FEMs for a large population of bridges.

The five damage identification algorithms that were investigated require mode shape data from the undamaged and damaged structure. In addition, some of the methods require resonant frequencies corresponding to the undamaged and damaged structure as well as mass-normalized mode shapes. To obtain mass-normalized mode shapes experimentally, the excitation force must be measured along with the excitation point response. However, it is the authors' opinion that if automated damage identification methods are to become an accepted part of a comprehensive bridge management system, these methods will have to monitor the response of a bridge to ambient (typically traffic-induced) vibration, hence a measure of the input will not be available. To this end, the data reduction methods used in the numerical portion of this study have assumed that the input is not monitored.

Experimental damage cases correspond to four cuts made in the web and extended down to and through the bottom flange of the north plate girder at the center of the middle span. The numerically simulated damage cases correspond to similar cuts made at various locations along the

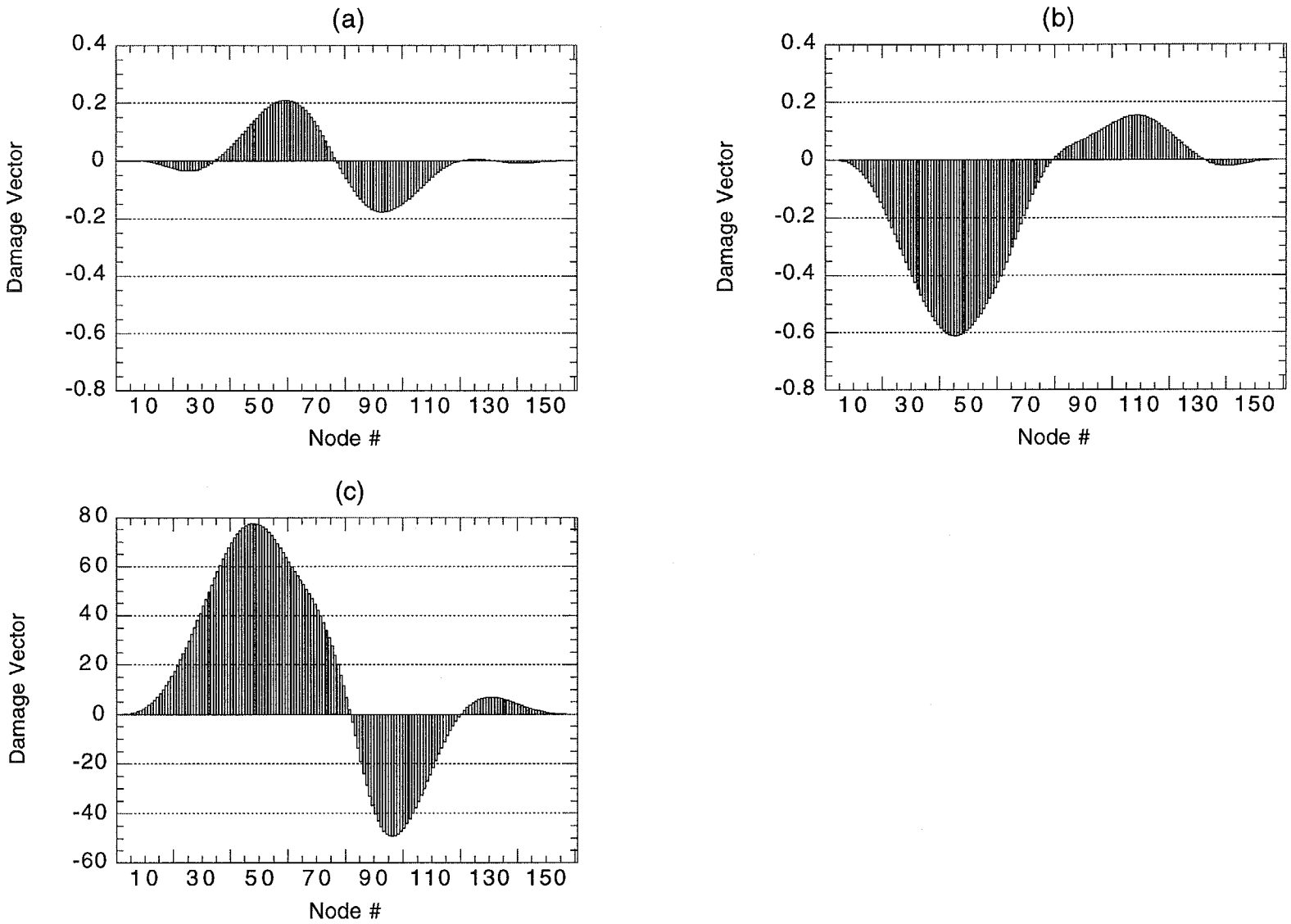

Fig. 67. Damage vector calculated for damage case (a) A-1, (b) A-2, and (c) A-3 using the modal data from SET3.

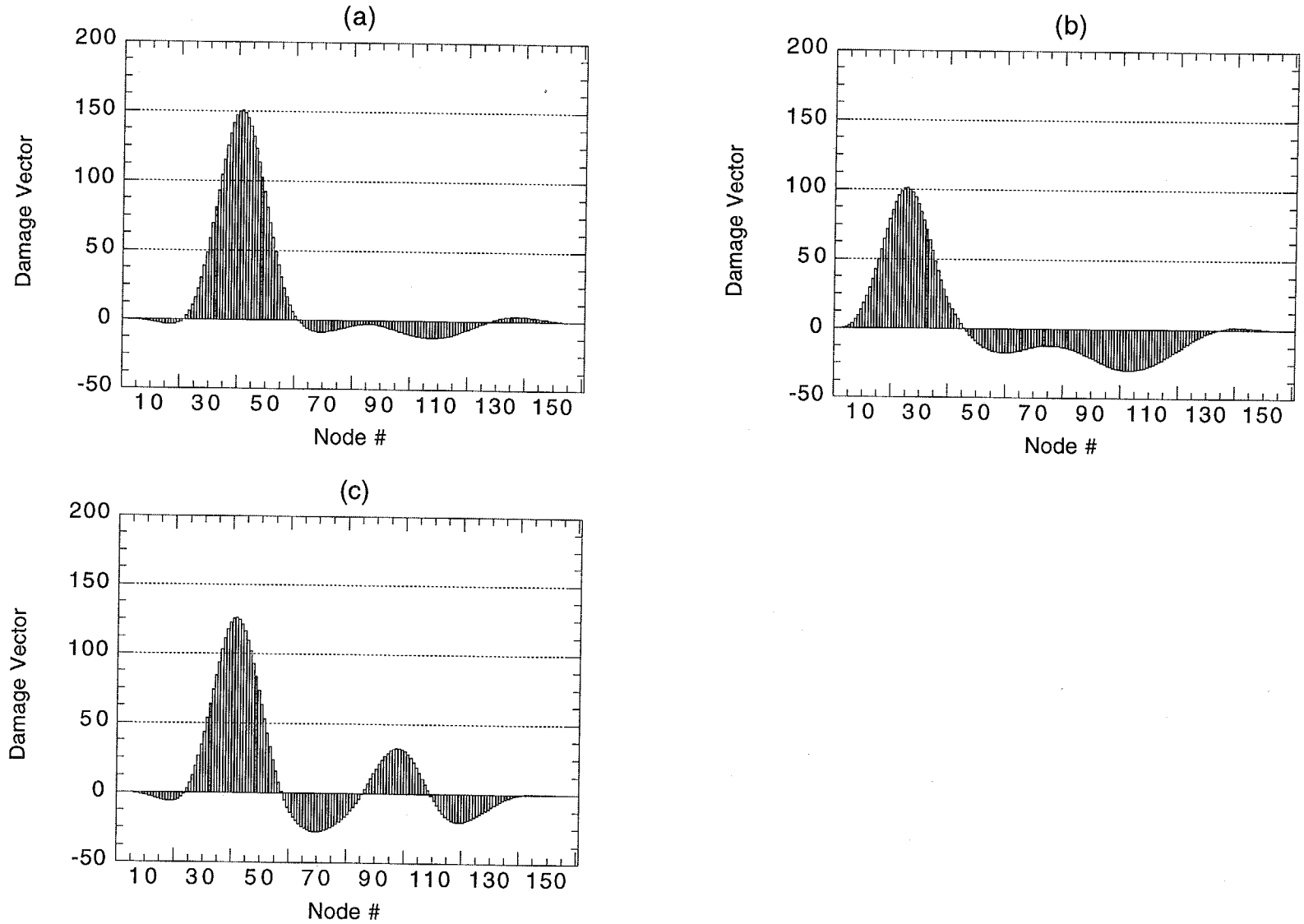

Fig. 68. Damage vector calculated for damage case (a) A-4, (b) A-5, and (c) A-6 using the modal data from SET3.

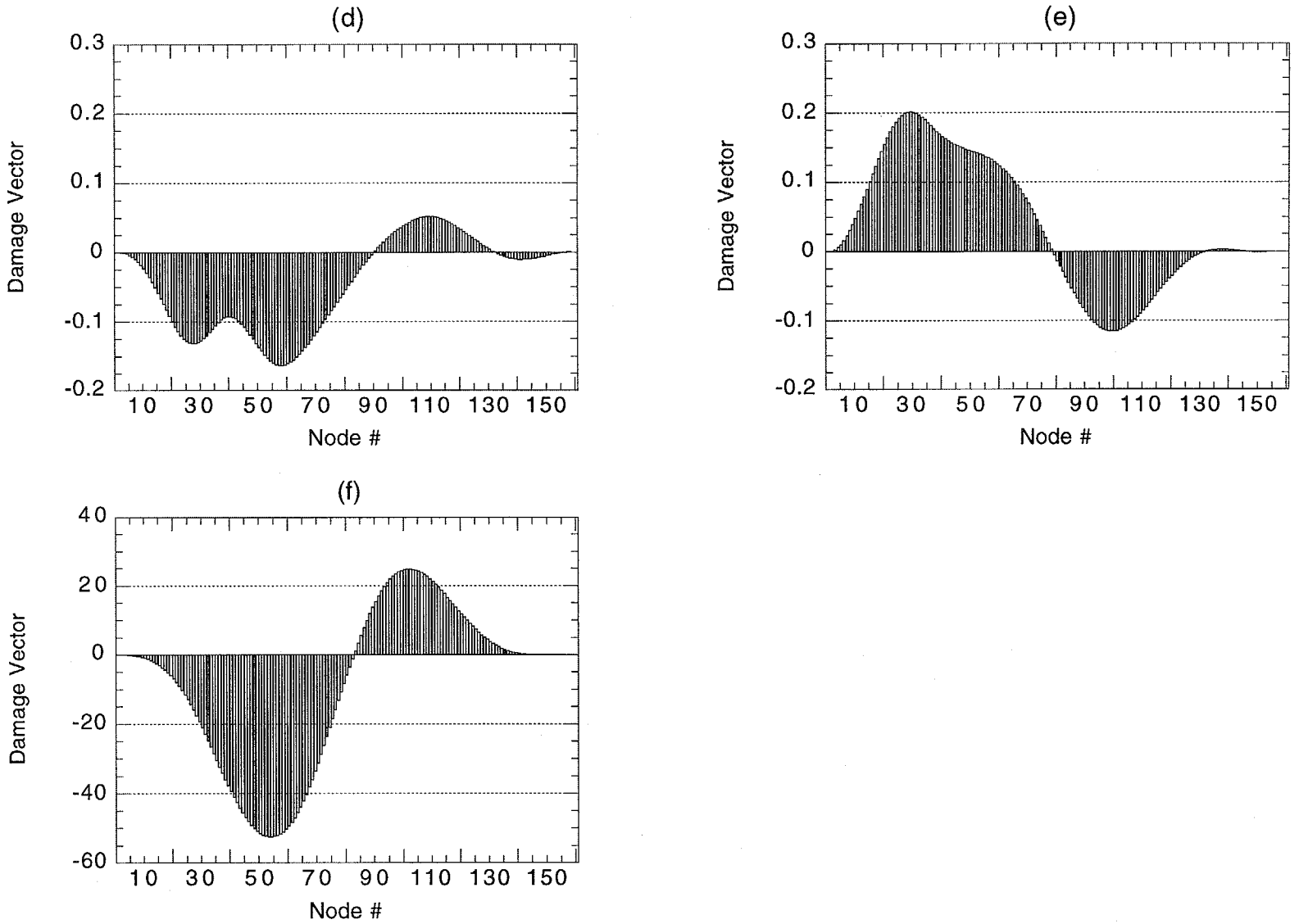

Figure 68 (cont). Damage vector calculated for damage case (a) A-7, (b) A-8, and the alternate undamaged case (c) A-9 using the modal data from SET3.

length of the middle span and one case where two different cut locations were specified in the middle span. Also, in the numerical studies, a final undamaged analysis was performed by replacing the original random forcing function with one that had identical frequency content and an identical peak amplitude. This case was used to determined if the algorithms would yield a false-positive reading, that is identify that damage had occurred when data from two different undamaged cases were analyzed.

Three sets of data, two experimental and one analytical, were used in this study. The first set (SET1) corresponds to a refined set of accelerometers located on the span of the girder where damage was introduced. Response measurements were made on the bridge before damage was introduced and after each level of damage. Although a hydraulic shaker provided the excitation for these tests, to simulate an ambient test, the input from the shaker was not recorded. Resonant frequencies were determined by curve fitting cross-correlation functions as discussed in Farrar et al. (1994). Mode shapes were determined from the phase and amplitude information contained in the CPS calculated with respect to a reference accelerometer. The mode shapes were normalized assuming an identity matrix for the mass matrix. Similar data reduction procedures were applied to nodal point accelerations, corresponding to locations that approximate the SET1 accelerometers, determined from the finite element analyses. These data are referred to as SET3. Also, measurements from a coarse set of accelerometers that were located on all three spans were used to form the data set referred to as SET2. Data from these accelerometers were recorded on the bridge before damage was introduced and after each level of damage. Again a hydraulic shaker provided the input for these measurements, and for SET2 this input was measured. These modal data were reduced using standard measured-input experimental modal analysis methods, and, hence, yielded mass-normalized mode shapes.

In general, all methods identified the damage location correctly for a cut, either the actual experimental one or the numerically simulated ones, completely through the bottom flange. However, for several of these methods, if they had been applied blindly, it would be difficult to tell if damage had not also occurred at locations other than the actual one. The methods were inconsistent and did not clearly identify the damage location when they were applied to the less severe damage cases. Results of this study show that the Damage Index Method performed the best when the entire set of analyses and experiments are considered. This performance is attributed to the methods of normalizing changes in the parameters that are used to indicate damage relative to the undamaged case. Also, this method is the only one that specifies criteria to quantify when changes in the monitored parameters are indicative of damage. Such a criteria is essential when trying to determine if damage has occurred at more than one location and for preventing false-positive readings. This criteria could, most likely, be adopted to the other methods used in this study.

Tables XII through XIV summarize the results of the five damage detection algorithms applied to the experimental and numerical modal data. In Table XII it can be seen that the Damage Index Method identified most of the damage cases correctly. This performance is considered noteworthy when one considers that the lowest level of damage, corresponding to only a 0.15 % reduction in the cross-section moment of inertia of the plate girder at the damage location, was located with the coarse set of accelerometers using only two measured modes as shown in Table XIII. The Damage Index Method failed only for damage case A-7, and for identification of the second damage location in case A-6. For the remaining damage cases, the location of damage was either clearly identified or narrowed down to two locations. It is pointed out that this method has the attractive feature of not needing mass-normalized mode shapes.

The Mode Shape Curvature Method also performed well. Only damage cases A-1 and A-2 went undetected using this technique, although for some of the lower levels of damage several locations were identified when there was only one actual damage location.

TABLE XII

Summary of Damage Detection Results using
Experimental Modal Data from Refined Set of Accelerometers (SET1)

Damage Case	Damage Index Method	Mode Shape Curvature Method	Change in Flexibility Method	Change in Uniform Flexibility Shapes Curvature Method	Change in Stiffness Method
E-1: 2' web cut centered vertically at the girder mid-height positioned at the girder midspan	•	•••	○	○	○
E-2: 6' web cut to topside of bottom flange positioned at the girder midspan	•	••	○	•••	○
E-3: 6' web plus half of bottom flange cut positioned at the girder midspan	•	•	○	•	○
E-4: 6' web plus full bottom flange cut positioned at the girder midspan	•	•	•	•	•

• Damage located
•• Damage narrowed down to two locations
••• Damage narrowed down to three locations
○ Damage not located

The Change in Flexibility Method had problems identifying less severe damage cases. As seen in Table XII, the location of damage was detected only for damage case E-4. Using the coarse set of accelerometer measurements (see Table XIII), the algorithm succeeded for cases E-3 and E-4 and failed for cases E-1 and E-2. Only damage cases A-4 through A-6, all of which involved severe damage, were detected from the numerical modal data (see Table XIV). Again, the algorithm failed to detect intermediate levels of damage when applied to the numerical data. Unexpectedly, damage case A-3 also went undetected although it consisted of a high level of damage.

The Change in Uniform Flexibility Shape Curvature Method performed satisfactorily using the experimental modal data from the refined set of accelerometers (SET1). The algorithm failed completely only for damage case E-1. This technique did not perform well when applied to the experimental data obtained from the coarse set of accelerometers (SET2). For damage cases E-1 through E-3, the technique generated ambiguous results. Using the numerical modal data, damage corresponding to cases A-1, A-2, and A-7 went undiscovered.

In contrast to the Change in Uniform Flexibility Shape Curvature Method, the Change in Stiffness Method improved when applied to the modal data from the coarse set of accelerometers. Significant improvements were also shown when only the first two modes were used instead of all six as shown in Table XIII. Using the refined measurements, only the final damage case (E-4) was detected, whereas all damage cases were detected from the SET2 modal data. When applied to the numerical data, the technique generated similar results as the Change in Flexibility Method (see Table XIV).

TABLE XIII

Summary of Damage Detection Results using
Experimental Modal Data from Coarse Set of Accelerometers (SET2)

Damage Case	Damage Index Method	Mode Shape Curvature Method	Change in Flexibility Method	Change in Uniform Flexibility Shapes Curvature Method	Change in Stiffness Method
E-1: 2' web cut centered vertically at the girder mid-height positioned at the girder midspan	**	**	○	○	**
E-2: 6' web cut to topside of bottom flange positioned at the girder midspan	**	*	○	○	**
E-3: 6' web plus half of bottom flange cut positioned at the girder midspan	**	**	**	○	**
E-4: 6' web plus full bottom flange cut positioned at the girder midspan	*	*	*	*	*

* Damage located
** Damage located using only 2 modes; damage unclear using all 6 modes
○ Damage not located

Although not rigorously verified, it appeared that using an assumed identity mass matrix to normalize the modes did not adversely affect the methods that require mass-normalized mode shapes. This result is attributed to the fact that the measured modes resemble beam-like response and the mass of the bridge is uniformly distributed along the longitudinal axis of this "beam".

When this study was performed, there was concern that the discontinuities in the plate girder where the flanges change dimension and at the splice plate locations could cause erroneous indications of damage by the various methods. With the experimental data from the coarse set of accelerometers for the lower level damage cases E-1 through E-3, the damage index method gave false indications of damage at locations where the flanges abruptly changed dimensions (elements 140 and 158) as well as at other locations that did not correspond to any significant change in geometry (elements 35 and 135). However, other locations of changes in the flange dimensions did not show indications of damage. Except for the damage indicated at element 35 when six modes were used, the other false reading were not consistent from one damage case to the other. For the damage index method the false reading were more pronounced when six modes were used as opposed to two modes. No false indications of damage were given by the Damage Index Method when data from the refined set of accelerometers were used. When the damage index method using the cubic polynomial interpolation was applied to the numerical data, false indications of damage were found for cases A-1, A-2 and A-7 at element 20, which corresponds to the location of the change in flange dimension. However, for these cases no erroneous indications of damage result when the cubic spline interpolation function is used. For case A-9 a false positive reading is almost given at element 20.

The Mode Shape Curvature method shows peaks in the change in curvature reading at various locations near the discontinuities when applied to the SET2 experimental data, but false peaks are also evident at locations that do not correspond to discontinuities. When applied to the numerical

TABLE XIV

Summary of Damage Detection Results using
Numerical Modal Data from Refined Set of Monitored Responses (SET3)

Damage Case	Damage Index Method	Mode Shape Curvature Method	Change in Flexibility Method	Change in Uniform Flexibility Shapes Curvature Method	Change in Stiffness Method
A-1: 3.5' web cut to topside of bottom flange positioned at the girder midspan	••	○	○	○	○
A-2: 3.5' web plus half of bottom flange cut positioned at the girder midspan	••	○	○	○	○
A-3: 3.5' web plus full bottom flange cut positioned at the girder midspan	•	•	○	•	○
A-4: 3.5' web plus full bottom flange cut positioned 40' from the interior support	•	•	•	•	•
A-5: 3.5' web plus full bottom flange cut positioned 20' from the interior support	•	•	•	•	•
A-6: 3.5' web plus full bottom flange cuts positioned 40' from the interior support and 20' from the girder midspan	• one damage location was not identified	•	•	•	•
A-7: 3.5' web cut to topside of bottom flange positioned 40' from the interior support	○	•	○	○	○
A-8: 3.5' web cut to topside of bottom flange positioned 20' from the interior support	••	•	○	•	○

• Damage located
•• Damage narrowed down to two locations
••• Damage narrowed down to three locations
○ Damage not located

data, this method shows significant changes in curvature at element 20 and element 140, as well as other locations for cases when the damage was located elsewhere. Similar results were obtained with the Change in Uniform Flexibility Shape Curvature Method. Although significant changes in the monitored parameter where noted at locations that did not correspond to damage, The Change in Flexibility method and the Change in Stiffness Method did not give false indications of damage at locations that could be associated with abrupt changes in geometry of the structure. In summary, no consistent trends could be observed in this study regarding the effects of abrupt geometric discontinuities on the ability of the various methods to correctly identify damage.

The authors acknowledge that recently reported improvements to the damage identification methods used in this study may offer enhanced capabilities to detect damage from changes in measured

modal properties. As an example, Doebling (1995) investigated the problem of assembling flexibility matrices from measured modal data. Methods for calculating residual flexibilities (the contribution of the unmeasured modes to the flexibility matrix) were developed and shown effective in improving the accuracy of the flexibility matrices. Using the experimental modal data corresponding to the coarse set of accelerometers, the flexibility shape of the I-40 Bridge with a unit load positioned at the damage location was derived with the bridge undamaged and then for the four experimental damage conditions. Comparison of the flexibility shapes revealed a local increase in flexibility at the damage location during the progression from the 2' web cut to the 6' web plus total flange cut. Because the Change in Flexibility Method and the Change in Uniform Flexibility Shape Curvature Method rely heavily on the accuracy of the flexibility matrices, their performance may be improved by deriving the flexibility matrices in accordance with Doebling (1995).

A more refined application of the Change in Stiffness Method to the I-40 Bridge can be found in James, et al. (1995). In this investigation, an attempt was made to derive mass and stiffness matrices, which better resemble the properties of the structure, by assuming a certain connectivity between the sensors. Under this assumption, terms of the mass and stiffness matrices not reflective of the assumed sensor connectivity are forced to zero. The matrices are further modified by separating the portion reflective of the assumed connectivity from the portion not reflective of the assumed connectivity. By considering the mass and stiffness matrices associated with the assumed model of the structure, the performance of the Change in Stiffness Method was improved.

The fact that all the damage identification algorithms except the Damage Index Method gave false-positive readings is of concern, particularly when one considers the possibility of implementing these algorithms in the field as part of an automated bridge surveillance system. Although not verified because of the need to run many more time-history analyses, it is the authors' opinion that forming the CPS or CPSD from more averages will help to alleviate this problem with false-positive readings.

Another observation from this study, which the authors feel should be emphasized, is that the Damage Index Method is the only method tested that has a specific criteria for determining if damage has occurred at a particular location. The other methods only look for the largest change in a particular parameter and it is ambiguous at times to determine if these changes indicate damage at more than one location. This ambiguity is illustrated in Figs. 51d and 60d where, in a blind test, it would be difficult to tell if damage has occurred at one or three locations. The criteria used by the damage index method for determining if a change in the damage index corresponds to actual damage is to look for statistical outliers in the population of all damage indices. It is the authors' opinion, though again not rigorously verified analytically, that this method will have difficulties if numerous damage locations are present (implying that the outliers will be closer to the mean) as was indicated by damage case A-6.

Notable contributions of this work include: (1) a summary of research reported in the technical literature related to the field of damage detection algorithms applied to bridges; (2) the generation of numerical time-history data from a benchmarked FEM of the I-40 Bridge for a variety of damage scenarios which required approximately one day of CPU time on a CRAY-YMP computer; (3) an unbiased, direct comparison of various linear damage identification methods when applied to a common set of damage scenarios. The authors acknowledge that many other damage identification methods exist and an obvious extension of this work would be to apply these methods to the same data sets reported herein.

VII. REFERENCES

ABAQUS/Standard User's Manual, Vols. I and II, Version 5.4, (1994) Hibbitt Karlsson & Sorenson, Inc. Providence, RI.

ABAQUS/Post Manual, Version 5.4, (1994) Hibbitt Karlsson & Sorenson, Inc. Providence, RI.

Aktan, A. E., K. L. Lee, C. Chuntavan, and T. Aksel (1994) "Modal Testing for Structural Identification and Condition Assessment of Constructed Facilities," *Proceedings of the 12th International Modal Analysis Conference*, **1**, 462-468.

Aktan, A. E., V. J. Hunt, M. J. Lally, R. B. Stillmaker, D. L. Brown, and S. J. Shelley (1995) "Field Laboratory for Modal Analysis and Condition Assessment of Highway Bridges," *Proceedings of the 13th International Modal Analysis Conference*, **1**, 718-727.

Bendat, J. S. and A. G. Piersol (1980) *Engineering Applications of Correlation and Spectral Analysis*, John Wiley, New York.

Biswas, M., A. K. Pandey, and M. M. Samman (1990) "Diagnostic Experimental Spectral/Modal Analysis of a Highway Bridge," *The International Journal of Analytical and Experimental Modal Analysis*, **5**, 33-42.

Doebling, S. W., et al., (1996) "Damage Identification in Structures and Mechanical Systems Based on Changes in their Vibration Characteristics: A Detailed Literature Review," Los Alamos National Laboratory report LA-13070-MS.

Doebling, S. W., (1995) "Measurement of Structural Flexibility Matrices for Experiments with Incomplete Reciprocity," Doctoral Dissertation, Dept. of Aerospace Engineering, Univ. of Colorado, Boulder.

Ewins, D. J. (1985) *Modal Testing: Theory and Practice,* John Wiley, New York.

Farrar, C. R., et al., (1994) "Dynamic Characterization and Damage Detection in the I-40 Bridge over the Rio Grande," Los Alamos National Laboratory report LA-12767-MS.

Farrar, C. R., et al., (1996) "Finite Element Analysis of the I-40 Bridge over the Rio Grande," Los Alamos National Laboratory report LA-12979-MS.

Gates, J. H. (1976) "California's Seismic Design Criteria For Bridges," *ASCE Journal of Structural Engineering*, **102**, 2301-2313.

Jain, B. K. (1991) "Diagnostics Through Experimental Vibration Signature Analysis of Prestressed Concrete Bridges," *International Symposium on Fracture in Steel and Concrete Structures*, 1123-1136.

James, G., R. Mayes, T. Carne, T. Simmermacher, and J. Goodding (1995) "Health Monitoring of Operational Structures - Initial Results," *Proc. of the 36th AIAA/ASME/ASCE/AHS/ASC Structures, Structural Dynamics, and Materials Conference.*

Kaouk, M. and D. C. Zimmerman (1994) "Structural Damage Detection using Measured Modal Data and No Original Analytical Model," *Proceedings of the 12th International Modal Analysis Conference*, **1**, 731 - 737.

Kato, M. and S. Shimada (1986) "Vibration of PC Bridge During Failure Process," *ASCE Journal of Structural Engineering*, **112**, 1692-1703.

Kim, J.-T. and N. Stubbs (1993) "Assessment of the Relative Impact of Model Uncertainty on the Accuracy of Global Nondestructive Damage Detection in Structures," report prepared for New Mexico State University.

Law, S. S., P. Waldron, and C. Taylor (1992) "Damage Detection of a Reinforced Concrete Bridge Deck Using Frequency Response Function," *Proceedings of the 11th International Modal Analysis Conference*, **2**, 772 - 778.

Liang, Z., M. Tong and G. C. Lee (1995) "Modal Energy Measurements of a Long Steel Bridge," *Proceedings of the 13th International Modal Analysis Conference*, **1**, 226 - 232.

MATLAB Reference Guide (1992) The MathWorks, Inc., Natick, MA.

MATLAB User's Guide (1992) The MathWorks, Inc., Natick, MA.

Mayes, R. L. and M. A. Nusser (1994) "The Interstate-40 Bridge Shaker Project," Sandia National Laboratory report SAND94-0228.

Mayes, R. L. (1995) "An Experimental Algorithm for Detecting Damage Applied to the I-40 Bridge over the Rio Grande," *Proceedings of the 13th International Modal Analysis Conference*, **1**, 219-225.

Mazurek, D. F. and J. T. DeWolf (1990) "Experimental Study of Bridge Monitoring Technique," *ASCE Journal of Structural Engineering*, **116**, 2532-2549.

Pandey, A. K., M. Biswas, and M. M. Samman (1991) "Damage Detection from Changes in Curvature Mode Shapes," *Journal of Sound and Vibration*, **145**(2), 321-332.

P3/PATRAN User Manual (1992) PDA Engineering, Costa Mesa, CA.

Pandey, A. K. and M. Biswas (1994) "Damage Detection in Structures using Changes in Flexibility," *Journal of Sound and Vibration*, **169**(1), 3-17.

Peterson, L.D., K. F. Alvin, S. W. Doebling, and K. C. Park (1993) "Damage Detection Using Experimentally Measured Mass and Stiffness Matrices," *Proc. of 34th AIAA/ASME/ASCE/AHS/ASC Structures, Structural Dynamics and Materials Conference*, 1993, 1518 - 1528,

Raghavendrachar, M. and A. E. Aktan (1992) "Flexibility by Multireference Impact Testing for Bridge Diagnostics," *ASCE Journal of Structural Engineering*, **118**, 2186-2203.

Richardson, M. H. (1980) "Detection of Damage in Structures from Changes in their Dynamic (Modal) Properties- A Survey," NUREG/CR-1431, U.S. Nuclear Regulatory Commission, Washington, D.C.

Salane, H. J., J. W. Baldwin, and R. C. Duffield (1981) "Dynamics Approach for Monitoring Bridge Deterioration," *Transportation Research Record* , **832,** 21-28.

Samman, M. M., M. Biswas, and A. K. Pandey (1991) "Employing Pattern Recognition for Detecting Cracks in a Bridge Model," *The International Journal of Analytical and Experimental Modal Analysis*, **6**, 35-44.

Signal Processing Toolbox (1992) The MathWorks, Inc., Natick, MA.

Shirole, A. M. and R. C. Holt (1991) "Planning for a Comprehensive Bridge Safety Assurance Program", *Transportation Research Record 1290,* 39-50.

Simmermacher, T., D. C. Zimmerman, R. L. Mayes, G. M. Reese, and G. H. James (1995) "The Effects of Finite Element Grid Density on Model Correlation and Damage Detection of a Bridge," *Proc. of the 36th AIAA/ASME/ASCE/AHS/ASC Structures, Structural Dynamics, and Materials Conference.*

Stubbs, N.and J.-T. Kim (1994) "Field Verification of a Nondestructive Damage Localization and Severity Estimation Algorithm," Texas A&M Univ. report prepared for New Mexico State Univ.

Stubbs, N., J.-T. Kim, and C. R. Farrar (1995) "Field Verification of a Nondestructive Damage Localization and Severity Estimation Algorithm," *Proceedings of the 13th International Modal Analysis Conference*, **1**, 210-218.

Spyrakos, C., H. L. Chen, J. Stephens, and V. Govidaraj (1990), "Evaluating Structural Deterioration Using Dynamic Response Characterization," *Proceedings Intelligent Structures,* Elsevier Applied Science, 137-154.

Structural Measurements Systems (1987) Modal 3.0, San Jose, CA.

Tang, J. P. and K.-M. Leu (1991) "Vibration Tests and Damage Detection of P/C Bridges," *Journal of the Chinese Institute of Engineers,* Vol. 14, 531-536.

Toksoy, T. and A. E. Aktan (1994) "Bridge-condition Assessment by Modal Flexibility," *Experimental Mechanics*, 271-278.

Turner, J. D. and A. J. Pretlove (1988) "A Study of the Spectrum of Traffic-Induced Bridge Vibration," *Journal of Sound and Vibration*, **122**, 31-42.

White, K. R., J. Minor, and K. N. Derucher (1992) *Bridge Maintenance, Inspection and Evaluation,* Marcel Dekker, New York.

Zhang, Z. and A. E. Aktan (1995) "The Damage Indices for the Constructed Facilities," *Proceedings of the 13th International Modal Analysis Conference*, **2**, 1520-1529.

Zimmerman, D. C. and M. Kaouk (1992) "Eigenstructure Assignment Approach for Structural Damage Detection," *AIAA Journal*, **30**(7), 1848-1855.

Zimmerman, D. C. and M. Kaouk (1994) "Structural Damage Detection using a Minimum Rank Update Theory," *Journal of Vibration and Acoustics*, **116**, 222-231.

APPENDIX A

EXPERIMENTAL MODE SHAPE DATA USED WITH DAMAGE IDENTIFICATION ALGORITHMS

TABLE A-1
Undamaged Mode Shape Data From Refined -Sensor, Cross-Power Spectra

	Mode 1 :	2.500 Hz	Mode 2 :	2.969 Hz	mode 3 :	3.562 Hz
Pt.	mag. g^2x10^{-9}	phase (degrees)	mag. g^2x10^{-9}	phase (degrees)	mag. g^2x10^{-9}	phase (degrees)
X1	2.202E+01	-2.532E+00	3.219E+01	-5.971E-01	1.010E+01	1.760E+02
X2	2.827E+02	6.782E-01	3.789E+02	2.114E-01	1.074E+02	1.862E+00
X3	5.698E+02	0.000E+00	7.582E+02	0.000E+00	1.790E+02	0.000E+00
X4	8.051E+02	5.495E-01	1.084E+03	4.129E-01	1.697E+02	1.111E+00
X5	9.764E+02	2.727E-01	1.306E+03	3.224E-01	1.007E+02	2.866E+00
X6	1.004E+03	3.346E-02	1.351E+03	4.066E-01	1.702E+01	9.825E+00
X7	9.478E+02	6.762E-02	1.256E+03	8.007E-01	7.686E+01	-1.791E+02
X8	7.933E+02	-7.207E-02	1.059E+03	7.976E-01	1.478E+02	1.791E+02
X9	5.827E+02	2.871E-01	7.872E+02	1.106E+00	1.682E+02	1.790E+02
X10	2.647E+02	-2.878E-01	3.643E+02	8.772E-01	9.043E+01	-1.789E+02
X11	2.550E+01	-7.886E-01	4.064E+01	-4.411E+00	1.555E+01	-2.091E+01

TABLE A-2
Damaged Mode Shape Data From Refined-Sensor, Cross-Power Spectra
Two-Foot-Cut at Center of the Web

	Mode 1 :	2.531 Hz	Mode 2 :	3.000 Hz	mode 3 :	3.594 Hz
Pt.	mag. g^2x10^{-9}	phase (degrees)	mag. g^2x10^{-9}	phase (degrees)	mag. g^2x10^{-9}	phase (degrees)
X1	1.672E+01	-6.427E+00	2.703E+01	2.436E+00	1.684E+01	1.648E+02
X2	2.180E+02	8.009E-01	3.145E+02	4.196E-01	1.360E+02	7.140E-01
X3	4.389E+02	0.000E+00	6.257E+02	0.000E+00	2.285E+02	0.000E+00
X4	6.196E+02	7.284E-01	8.937E+02	6.380E-01	2.087E+02	7.099E-01
X5	7.508E+02	4.059E-01	1.074E+03	4.360E-01	1.106E+02	4.188E+00
X6	7.797E+02	2.343E-01	1.117E+03	4.838E-01	1.692E+01	1.167E+02
X7	7.322E+02	1.180E-01	1.034E+03	9.206E-01	1.362E+02	1.709E+02
X8	6.124E+02	3.210E-02	8.697E+02	8.814E-01	2.236E+02	1.735E+02
X9	4.487E+02	3.473E-01	6.446E+02	1.315E+00	2.408E+02	1.750E+02
X10	2.039E+02	-3.884E-01	2.989E+02	1.185E+00	1.306E+02	1.758E+02
X11	1.927E+01	-5.214E+00	3.205E+01	9.973E-01	1.931E+01	-1.828E+01

TABLE A-3
Damaged Mode Shape Data From Refined-Sensor, Cross-Power Spectra
Six-Foot-Cut to Bottom of the Web

	Mode 1 :	2.531 Hz	Mode 2 :	3.000 Hz	mode 3 :	3.531 Hz
Pt.	mag. g^2x10^{-9}	phase (degrees)	mag. g^2x10^{-9}	phase (degrees)	mag. g^2x10^{-9}	phase (degrees)
X1	2.251E+00	1.277E+00	1.096E+01	7.615E+00	4.838E+00	1.715E+02
X2	2.757E+01	5.624E-01	1.247E+02	4.957E-01	3.667E+01	1.639E+00
X3	5.504E+01	0.000E+00	2.511E+02	0.000E+00	6.263E+01	0.000E+00
X4	7.915E+01	5.758E-01	3.584E+02	2.468E-01	5.941E+01	1.028E+00
X5	9.636E+01	2.272E-01	4.314E+02	7.153E-02	3.533E+01	1.918E+00
X6	9.941E+01	1.606E-01	4.470E+02	6.585E-02	5.963E+00	1.430E+01
X7	9.346E+01	1.084E-01	4.142E+02	3.891E-01	2.770E+01	1.764E+02
X8	7.826E+01	-1.151E-01	3.462E+02	4.062E-01	5.162E+01	1.776E+02
X9	5.739E+01	2.789E-01	2.568E+02	9.323E-01	5.798E+01	1.780E+02
X10	2.621E+01	-1.641E-01	1.186E+02	1.199E+00	3.134E+01	1.788E+02
X11	2.555E+00	4.546E+00	1.350E+01	1.000E+01	5.119E+00	-8.770E+00

TABLE A-4
Damaged Mode Shape Data From Refined -Sensor, Cross-Power Spectra
Six-Foot-Cut to the Bottom of the Web and Cut Through Half the Bottom Flange

	Mode 1 :	2.469 Hz	Mode 2 :	2.938 Hz	mode 3 :	3.500 Hz
Pt.	mag. g^2x10^{-9}	phase (degrees)	mag. g^2x10^{-9}	phase (degrees)	mag. g^2x10^{-9}	phase (degrees)
X1	1.604E+01	-7.263E-01	3.612E+01	7.879E-01	7.300E+00	1.751E+02
X2	1.951E+02	3.378E-01	4.225E+02	4.739E-02	6.524E+01	1.112E+00
X3	3.907E+02	0.000E+00	8.506E+02	0.000E+00	1.099E+02	0.000E+00
X4	5.560E+02	5.551E-01	1.221E+03	2.726E-01	1.035E+02	6.430E-01
X5	6.787E+02	1.996E-01	1.480E+03	1.559E-01	5.986E+01	1.800E+00
X6	7.001E+02	-2.605E-02	1.535E+03	1.540E-01	8.325E+00	8.103E+00
X7	6.569E+02	-4.889E-02	1.427E+03	4.738E-01	5.129E+01	-1.799E+02
X8	5.493E+02	-6.362E-02	1.196E+03	5.469E-01	9.388E+01	1.793E+02
X9	4.031E+02	5.275E-01	8.842E+02	9.250E-01	1.045E+02	1.794E+02
X10	1.824E+02	-2.169E-01	4.062E+02	4.199E-01	5.656E+01	-1.797E+02
X11	1.851E+01	-3.758E+00	4.229E+01	-1.675E+00	8.894E+00	-1.922E+01

TABLE A-5

Damaged Mode Shape Data From Refined-Sensor, Cross-Power Spectra
Six-Foot-Cut to the Bottom of the Web and Cut Through the Entire Bottom Flange

	Mode 1 :	2.312 Hz	Mode 2 :	2.844 Hz	mode 3 :	3.500 Hz
Pt.	mag. g^2x10^{-9}	phase (degrees)	mag. g^2x10^{-9}	phase (degrees)	mag. g^2x10^{-9}	phase (degrees)
X1	1.230E+00	1.070E+01	9.110E+00	-1.472E+00	3.862E+00	-1.791E+02
X2	1.577E+01	4.181E-01	1.079E+02	4.261E-01	3.866E+01	1.152E+00
X3	3.252E+01	0.000E+00	2.228E+02	0.000E+00	6.535E+01	0.000E+00
X4	4.938E+01	3.772E-01	3.417E+02	2.078E-01	6.257E+01	2.756E-01
X5	6.509E+01	-7.649E-02	4.445E+02	5.227E-02	3.870E+01	-5.862E-02
X6	7.350E+01	-4.978E-01	5.035E+02	2.559E-02	8.478E+00	-2.865E+00
X7	6.477E+01	-4.358E-01	4.363E+02	2.366E-01	2.647E+01	-1.788E+02
X8	5.053E+01	-3.573E-01	3.405E+02	1.365E-01	5.048E+01	1.798E+02
X9	3.508E+01	1.584E-01	2.388E+02	4.811E-01	5.770E+01	1.793E+02
X10	1.504E+01	6.280E-01	1.059E+02	-2.621E-01	3.171E+01	1.790E+02
X11	1.354E+00	8.664E+00	1.172E+01	1.527E+00	4.446E+00	1.856E+00

TABLE A-6
Test t16tr Undamaged Forced-Vibration Coarse-Sensor
Global Polynomial Curve-Fit Results

Location	Mode 1 F=2.48 Hz, ζ=1.06 %	Mode 2 F=2.96 Hz, ζ=1.29 %	Mode 3 F=3.50 Hz, ζ=1.52 %	Mode 4 F=4.08 Hz, ζ=1.10 %	Mode 5 F=4.17 Hz, ζ=0.86 %	Mode 6 F=4.63 Hz, ζ=0.92 %
S1	M=257u P=184	173u 353	472u 12.9	702u 358	513u 176	414u 5.63
S2	M=6.90m P=174	5.55m 360	0.014 1.72	0.013 6.25	0.011 172	9.88m 2.90
S3	M=0.010 P=174	8.38m 1.39	0.019 1.99	0.017 6.99	0.015 173	0.013 2.99
S4	M=8.01m P=178	6.98m 4.00	0.013 3.08	9.94m 8.91	0.010 175	7.67m 4.04
S5	M=16.6u P=70.3	137u 165	716u 3.55	1.17m 2.70	609u 172	1.03m 1.59
S6	M=0.014 P=358	0.014 180	4.48m 172	7.72m 355	3.44m 10.8	7.49m 357
S7	M=0.023 P=3.33	0.024 183	1.04m 139	0.015 0.626	1.89m 58.4	0.014 0.09
S8	M=0.015 P=2.84	0.016 182	3.87m 5.74	9.44m 2.45	2.71m 158	8.43m 360
S9	M=456u P=353	535u 176	511u 164	1.06m 352	491u 13.8	1.08m 0.168
S10	M=8.62m P=183	8.87m 0.053	0.014 178	7.73m 350	0.012 4.50	8.61m 2.15
S11	M=0.010 P=177	0.011 356	0.020 174	0.013 349	0.017 2.41	0.014 360
S12	M=7.54m P=184	8.43m 359	0.016 177	0.011 352	0.013 5.210	0.012 1.76
S13	M=423u P=181	472u 9.33	895u 178	697u 355	918u 6.95	827u 5.18
N1	M=302u P=202	293u 150	478u 10.0	610u 351	735u 2.03	552u 193
N2	M=7.46m P=183	7.62m 185	0.014 0.555	0.010 348	0.015 2.33	0.015 184
N3	M=0.010 P=183	0.011 186	0.018 0.954	0.012 347	0.019 2.57	0.018 184
N4	M=8.12m P=184	8.42m 184	0.011 360	6.58m 343	0.012 1.32	9.92m 184
N5	M=201u P=205	111u 136	652u 0.569	900u 349	869u 1.38	1.26m 181
N6	M=0.014 P=2.66	0.016 2.61	4.28m 179	7.71m 2.75	4.25m 177	9.68m 181
N7	M=0.021 P=4.04	0.024 2.32	464u 202	0.013 360	879u 143	0.017 182
N8	M=0.014 P=3.34	0.017 2.28	3.39m 0.195	6.85m 355	3.38m 5.00	0.010 182
N9	M=367u P=325	783u 347	427u 160	942u 1.73	605u 176	1.50m 179
N10	M=7.52m P=185	9.97m 182	0.012 180	0.010 10.4	0.013 182	0.011 186
N11	M=0.010 P=179	0.014 178	0.019 177	0.017 6.54	0.020 179	0.019 183
N12	M=6.99m P=178	9.54m 178	0.015 176	0.014 5.73	0.016 178	0.015 183
N13	M=434u P=188	561u 183	981u 170	1.04m 5.53	1.18m 179	1.23m 185

m = x 10^{-3}, u = x 10^{-6}, M = magnitude, P = phase in degrees

TABLE A-7
Test t17tr Damaged (First Stage) Forced-Vibration Coarse-Sensor
Global Polynomial Curve-Fit Results

Location	Mode 1 F=2.52 Hz, ζ=1.20 %	Mode 2 F=3.00 Hz, ζ=0.80 %	Mode 3 F=3.57 Hz, ζ=0.87 %	Mode 4 F=4.12 Hz, ζ=1.00 %	Mode 5 F=4.21 Hz, ζ=1.04 %	Mode 6 F=4.69 Hz, ζ=0.90 %
S1	M=3.95m P=178	3.70m 159	8.17m 176	9.66m 357	8.19m 181	7.19m 2.48
S2	M=0.218 P=170	0.171 168	0.443 179	0.393 3.79	0.392 178	0.346 3.47
S3	M=0.320 P=171	0.258 169	0.597 179	0.497 4.18	0.532 178	0.449 3.62
S4	M=0.257 P=175	0.218 172	0.404 180	0.293 5.68	0.363 178	0.278 4.15
S5	M=6.08m P=113	3.76m 103	0.024 175	0.034 3.03	0.024 177	0.035 3.97
S6	M=0.454 P=358	0.433 355	0.151 349	0.248 356	0.090 359	0.219 358
S7	M=0.732 P=4.27	0.715 359	0.049 316	0.473 0.468	0.020 142	0.423 1.54
S8	M=0.491 P=4.74	0.490 359	0.119 189	0.275 1.98	0.120 175	0.255 1.98
S9	M=0.015 P=6.04	0.016 4.92	0.016 345	0.035 353	0.012 7.55	0.034 0.641
S10	M=0.268 P=181	0.273 177	0.435 358	0.294 354	0.367 0.742	0.275 1.68
S11	M=0.314 P=175	0.322 172	0.603 356	0.465 353	0.494 358	0.421 359
S12	M=0.230 P=179	0.246 176	0.497 359	0.403 356	0.411 1.27	0.374 1.44
S13	M=0.015 P=161	0.014 175	0.019 6.35	0.019 5.36	0.025 8.86	0.020 11.1
N1	M=0.010 P=194	6.18m 346	0.015 183	0.018 0.438	0.020 359	0.017 190
N2	M=0.263 P=186	0.222 357	0.448 181	0.371 355	0.471 0.170	0.453 183
N3	M=0.372 P=186	0.322 358	0.581 182	0.451 355	0.617 0.320	0.565 183
N4	M=0.279 P=185	0.242 356	0.368 181	0.248 353	0.390 359	0.315 183
N5	M=4.90m P=226	1.73m 203	0.024 175	0.031 356	0.028 0.386	0.039 181
N6	M=0.494 P=4.80	0.468 177	0.125 4.32	0.238 5.12	0.126 173	0.273 181
N7	M=0.741 P=5.93	0.714 178	0.011 101	0.418 2.80	0.024 119	0.486 181
N8	M=0.486 P=3.07	0.490 177	0.123 177	0.239 359	0.115 3.76	0.291 181
N9	M=0.019 P=346	0.030 199	0.013 336	0.032 10.7	0.013 169	0.044 175
N10	M=0.278 P=181	0.292 358	0.396 359	0.283 9.98	0.420 178	0.332 181
N11	M=0.353 P=179	0.390 357	0.599 358	0.478 9.65	0.637 177	0.557 181
N12	M=0.247 P=176	0.268 358	0.463 358	0.394 7.85	0.491 176	0.452 181
N13	M=0.013 P=176	0.014 7.86	0.026 355	0.023 6.92	0.036 176	0.032 184

m = x 10^{-3}, u = x 10^{-6}, M = magnitude, P = phase in degrees

TABLE A-8
Test t18tr Damaged (Second Stage) Forced-Vibration Coarse-Sensor
Global Polynomial Curve-Fit Results

Location	Mode 1 F=2.52 Hz, ζ=1.33 %	Mode 2 F=2.99 Hz, ζ=0.82 %	Mode 3 F=3.52 Hz, ζ=0.95 %	Mode 4 F=4.09 Hz, ζ=0.85 %	Mode 5 F=4.19 Hz, ζ=0.65 %	Mode 6 F=4.66 Hz, ζ=0.84 %
S1	M=5.56m P=178	3.15m 162	6.18m 356	9.92m 5.32	7.41m 173	6.28m 3.56
S2	M=0.226 P=173	0.194 174	0.393 1.48	0.339 7.73	0.353 176	0.332 3.38
S3	M=0.316 P=165	0.285 174	0.530 2.33	0.421 9.00	0.475 175	0.420 1.53
S4	M=0.246 P=171	0.236 178	0.355 2.79	0.247 10.8	0.324 176	0.257 2.00
S5	M=0.037 P=237	8.37m 159	0.017 339	0.032 356	0.024 180	0.034 357
S6	M=0.425 P=353	0.435 357	0.134 172	0.209 360	0.096 13.4	0.230 355
S7	M=0.684 P=359	0.711 0.703	0.043 135	0.407 4.70	0.047 83.6	0.429 358
S8	M=0.475 P=359	0.495 360	0.105 13.6	0.248 6.06	0.098 164	0.263 358
S9	M=0.016 P=359	0.016 359	0.015 165	0.028 358	0.014 21.8	0.035 360
S10	M=0.255 P=174	0.263 178	0.392 181	0.224 357	0.344 5.44	0.265 358
S11	M=0.306 P=170	0.307 174	0.558 178	0.361 355	0.472 3.69	0.408 356
S12	M=0.225 P=171	0.234 178	0.464 181	0.322 359	0.395 6.72	0.368 358
S13	M=9.16m P=167	0.015 188	0.025 185	0.021 358	0.026 6.49	0.27 357
N1	M=0.013 P=197	7.03m 339	0.013 4.34	0.018 0.301	0.022 8.60	0.016 191
N2	M=0.223 P=182	0.211 360	0.384 2.46	0.307 357	0.459 4.90	0.444 180
N3	M=0.331 P=183	0.313 0.619	0.502 3.56	0.369 357	0.604 5.33	0.562 181
N4	M=0.260 P=184	0.229 359	0.311 2.28	0.197 355	0.381 4.77	0.311 182
N5	M=7.27m P=201	4.84m 221	0.019 348	0.027 353	0.026 1.53	0.036 179
N6	M=0.441 P=1.68	0.464 181	0.123 184	0.196 9.22	0.128 177	0.270 179
N7	M=0.680 P=3.20	0.711 181	0.015 187	0.344 6.38	0.032 130	0.493 179
N8	M=0.454 P=358	0.479 180	0.088 4.20	0.188 4.15	0.112 12.3	0.295 178
N9	M=0.014 P=338	0.022 176	9.05m 175	0.026 9.87	0.016 177	0.042 176
N10	M=0.250 P=176	0.279 0.511	0.343 180	0.243 15.1	0.410 180	0.320 180
N11	M=0.329 P=173	0.377 0.484	0.534 180	0.419 13.2	0.636 180	0.549 179
N12	M=0.221 P=170	0.258 0.259	0.415 179	0.343 12.5	0.486 179	0.441 179
N13	M=0.014 P=179	0.016 3.30	0.027 181	0.024 14.0	0.034 181	0.033 179

m = x 10^{-3}, u = x 10^{-6}, M = magnitude, P = phase in degrees

TABLE A-9
Test t19tr Damaged (Third Stage) Forced-Vibration Coarse-Sensor
Global Polynomial Curve-Fit Results

Location	Mode 1 F=2.46 Hz, ζ=0.82 %	Mode 2 F=2.95 Hz, ζ=0.89 %	Mode 3 F=3.48 Hz, ζ=0.92 %	Mode 4 F=4.04 Hz, ζ=0.81%	Mode 5 F=4.14 Hz, ζ=0.62 %	Mode 6 F=4.58 Hz, ζ=1.06 %
S1	M=4.48m P=171	2.90m 149	8.38m 3.78	0.011 357	0.010 171	6.52m 15.3
S2	M=0.200 P=174	0.182 178	0.433 2.94	0.352 6.36	0.374 174	0.315 7.43
S3	M=0.295 P=175	0.277 179	0.583 3.00	0.441 7.15	0.502 174	0.409 7.26
S4	M=0.231 P=179	0.230 182	0.392 4.36	0.259 8.92	0.342 176	0.250 8.44
S5	M=3.07m P=162	429u 53.2	0.021 6.78	0.034 2.97	0.023 172	0.035 4.35
S6	M=0.389 P=360	0.441 359	0.152 175	0.228 357	0.092 11.6	0.236 357
S7	M=0.636 P=4.92	0.730 2.62	0.051 158	0.444 2.53	0.045 96.2	0.452 0.738
S8	M=0.427 P=3.71	0.498 1.67	0.105 10.5	0.267 3.66	0.111 166	0.284 0.729
S9	M=0.012 P=4.72	0.016 5.46	0.016 166	0.032 355	0.011 17.0	0.036 0.271
S10	M=0.250 P=181	0.277 178	0.423 180	0.255 355	0.351 3.76	0.247 0.944
S11	M=0.293 P=176	0.322 174	0.597 177	0.409 354	0.478 2.03	0.388 359
S12	M=0.218 P=180	0.252 177	0.501 180	0.366 357	0.403 5.12	0.360 1.18
S13	M=0.014 P=180	0.017 177	0.032 179	0.025 355	0.028 5.08	0.027 1.70
N1	M=9.50m P=194	8.38m 355	0.019 7.78	0.020 357	0.024 4.88	0.015 204
N2	M=0.208 P=185	0.234 0.612	0.428 2.78	0.354 354	0.454 4.06	0.417 186
N3	M=0.297 P=185	0.340 1.08	0.559 2.90	0.435 354	0.597 4.10	0.518 186
N4	M=0.226 P=184	0.252 359	0.349 2.03	0.240 351	0.373 3.04	0.279 186
N5	M=2.68m P=209	1.24m 321	0.19 2.39	0.029 354	0.025 2.85	0.035 184
N6	M=0.405 P=4.30	0.480 181	0.129 181	0.205 6.78	0.132 177	0.284 180
N7	M=0.625 P=5.40	0.737 182	7.65m 197	0.375 3.87	0.033 143	0.510 181
N8	M=0.418 P=3.01	0.504 180	0.114 1.31	0.215 359	0.107 7.60	0.300 181
N9	M=0.013 P=2.24	0.021 174	0.012 166	0.025 6.23	0.015 172	0.043 178
N10	M=0.226 P=175	0.260 359	0.366 176	0.234 9.30	0.388 176	0.298 179
N11	M=0.313 P=179	0.378 2.30	0.588 180	0.423 11.7	0.640 179	0.544 182
N12	M=0.217 P=177	0.261 2.89	0.458 179	0.351 10.7	0.493 178	0.439 182
N13	M=0.011 P=174	0.021 12.7	0.036 176	0.026 10.4	0.036 178	0.038 181

m = x 10^{-3}, u = x 10^{-6}, M = magnitude, P = phase in degrees

TABLE A-10
Test t22tr Damaged (Final Stage) Forced-Vibration Coarse-Sensor
Global Polynomial Curve-Fit Results

Location	Mode 1 F=2.30 Hz, ζ=1.60 %	Mode 2 F=2.84 Hz, ζ=0.66 %	Mode 3 F=3.49 Hz, ζ=0.80 %	Mode 4 F=3.99 Hz, ζ=0.80 %	Mode 5 F=4.15 Hz, ζ=0.71 %	Mode 6 F=4.52 Hz, ζ=1.06 %
S1	M=8.40m P=135	6.64m 141	0.016 9.20	9.55m 337	0.016 176	0.012 8.34
S2	M=0.101 P=161	0.247 176	0.405 1.92	0.278 1.73	0.414 180	0.365 3.25
S3	M=0.143 P=162	0.365 175	0.543 2.20	0.339 1.39	0.553 180	0.469 3.56
S4	M=0.110 P=169	0.292 179	0.364 3.68	0.193 1.98	0.377 181	0.284 4.40
S5	M=0.013 P=152	2.19m 185	0.021 13.8	0.022 360	0.025 176	0.037 359
S6	M=0.204 P=347	0.495 355	0.135 176	0.220 4.91	0.090 360	0.282 355
S7	M=0.368 P=354	0.797 359	0.036 177	0.411 5.90	0.019 160	0.513 359
S8	M=0.251 P=356	0.550 358	0.102 6.93	0.236 6.02	0.118 179	0.311 359
S9	M=7.19m P=67.0	0.015 360	0.015 158	0.028 357	0.011 5.34	0.038 357
S10	M=0.131 P=168	0.322 178	0.399 181	0.249 6.03	0.370 1.09	0.312 359
S11	M=0.177 P=169	0.384 174	0.560 179	0.394 3.46	0.498 359	0.485 357
S12	M=0.118 P=170	0.297 179	0.469 182	0.352 6.69	0.419 1.60	0.444 359
S13	M=0.013 P=113	0.017 182	0.029 174	0.022 9.86	0.028 1.84	0.032 4.16
N1	M=0.012 P=207	478u 351	0.021 17.3	0.022 9.75	0.027 1.83	9.95m 199
N2	M=0.204 P=181	0.104 0.076	0.418 4.76	0.435 4.94	0.480 1.83	0.383 180
N3	M=0.292 P=179	0.154 360	0.543 5.02	0.546 5.28	0.630 1.98	0.487 180
N4	M=0.232 P=178	0.122 359	0.341 4.32	0.309 3.86	0.395 1.35	0.272 180
N5	M=0.014 P=156	741u 85.5	0.022 17.3	0.027 10.8	0.027 2.58	0.029 180
N6	M=0.500 P=2.24	0.298 179	0.130 181	0.140 8.63	0.145 182	0.171 179
N7	M=0.964 P=3.61	0.559 180	0.013 167	0.386 6.93	0.026 192	0.446 179
N8	M=0.535 P=1.25	0.323 179	0.105 6.16	0.170 4.28	0.111 1.39	0.199 177
N9	M=0.023 P=343	0.016 167	9.99m 148	0.023 0.811	0.015 183	0.034 173
N10	M=0.252 P=177	0.116 353	0.338 178	0.265 3.58	0.398 179	0.275 179
N11	M=0.342 P=182	0.169 357	0.563 182	0.482 8.37	0.679 182	0.510 181
N12	M=0.226 P=181	0.108 355	0.435 182	0.388 7.92	0.519 182	0.401 181
N13	M=0.011 P=187	6.02m 0.846	0.033 172	0.031 9.52	0.041 183	0.034 179

m = x 10^{-3}, u = x 10^{-6}, M = magnitude, P = phase in degrees

APPENDIX B

NUMERICAL MODE SHAPE DATA USED WITH DAMAGE IDENTIFICATION ALGORITHMS

TABLE B-1

Undamaged Mode Shape Data from Simulated Refined-Sensor, Cross-Power Spectra

Location	Mode 1: 3.79 Hz	Mode 2: 3.87 Hz	Mode 3: 5.09 Hz
N-1	0.33	1.21	-11.13
N-2	12.86	47.10	103.14
N-3	28.82	107.82	139.85
N-4	42.13	160.02	94.54
N-5	47.34	182.16	-0.48
N-6	42.44	165.61	-95.68
N-7	29.29	116.47	-141.21
N-8	13.21	54.02	-104.12
N-9	0.32	1.22	12.12

TABLE B-2

Damaged Mode Shape Data from Simulated Refined-Sensor, Cross-Power Spectra
Damage Case A-1

Location	Mode 1: 3.79 Hz	Mode 2: 3.87 Hz	Mode 3: 5.09 Hz
N-1	0.33	1.22	-11.12
N-2	12.61	46.30	103.36
N-3	28.34	106.08	140.26
N-4	41.51	157.54	95.01
N-5	46.73	179.45	-0.08
N-6	41.96	163.25	-95.50
N-7	29.02	114.89	-141.25
N-8	13.14	53.35	-104.24
N-9	0.32	1.22	12.16

TABLE B-3

Damaged Mode Shape Data from Simulated Refined-Sensor, Cross-Power Spectra
Damage Case A-2

Location	Mode 1: 3.79 Hz	Mode 2: 3.87 Hz	Mode 3: 5.09 Hz
N-1	0.33	1.20	-11.11
N-2	12.30	45.32	103.42
N-3	27.76	103.96	140.38
N-4	40.77	154.55	95.16
N-5	46.00	176.19	0.04
N-6	41.39	160.36	-95.43
N-7	28.69	112.95	-141.25
N-8	13.03	52.51	-104.26
N-9	0.32	1.21	12.17

TABLE B-4

Damaged Mode Shape Data from Simulated Refined-Sensor, Cross-Power Spectra
Damage Case A-3

Location	Mode 1: 3.63 Hz	Mode 2: 3.84 Hz	Mode 3: 5.09 Hz
N-1	0.00	0.04	-10.74
N-2	0.13	2.59	106.29
N-3	0.24	5.26	146.45
N-4	0.31	7.34	103.45
N-5	0.32	8.27	8.58
N-6	0.23	6.65	-91.43
N-7	0.12	4.18	-141.45
N-8	0.03	1.72	-105.98
N-9	0.00	0.04	13.08

TABLE B-5

Damaged Mode Shape Data from Simulated Refined-Sensor, Cross-Power Spectra
Damage Case A-4

Location	Mode 1: 3.79 Hz	Mode 2: 3.87 Hz	Mode 3: 5.07 Hz
N-1	0.56	1.51	-12.65
N-2	27.54	59.45	132.86
N-3	56.82	130.20	216.26
N-4	71.69	183.52	112.74
N-5	72.93	201.91	-24.54
N-6	59.53	177.98	-140.11
N-7	36.44	120.68	-183.48
N-8	13.62	53.27	-127.74
N-9	0.47	1.37	11.07

TABLE B-6

Damaged Mode Shape Data from Simulated Refined-Sensor, Cross-Power Spectra
Damage Case A-5

Location	Mode 1: 3.63 Hz	Mode 2: 3.85 Hz	Mode 3: 5.07 Hz
N-1	0.30	0.26	-11.40
N-2	4.70	8.54	103.61
N-3	15.39	18.85	105.03
N-4	23.78	25.88	63.88
N-5	27.19	27.45	-2.19
N-6	24.69	23.23	-64.22
N-7	17.38	14.96	-92.35
N-8	8.10	6.12	-67.28
N-9	0.20	0.18	6.75

TABLE B-7

Damaged Mode Shape Data from Simulated Refined-Sensor, Cross-Power Spectra
Damage Case A-6

Location	Mode 1: 3.69 Hz	Mode 2: 3.85 Hz	Mode 3: 5.07 Hz
N-1	0.00	0.24	-11.95
N-2	0.15	11.76	158.46
N-3	0.35	24.67	265.69
N-4	0.56	33.25	153.83
N-5	0.67	36.12	-13.13
N-6	0.66	32.54	-179.16
N-7	0.44	20.43	-189.88
N-8	0.20	8.23	-121.91
N-9	0.00	0.22	9.74

TABLE B-8

Damaged Mode Shape Data from Simulated Refined-Sensor, Cross-Power Spectra
Damage Case A-7

Location	Mode 1: 3.79 Hz	Mode 2: 3.87 Hz	Mode 3: 5.09 Hz
N-1	0.33	1.22	-11.18
N-2	12.53	46.16	103.44
N-3	28.18	105.75	140.40
N-4	41.29	157.06	95.02
N-5	46.49	178.90	-0.22
N-6	41.76	162.75	-95.70
N-7	28.89	114.55	-141.45
N-8	13.08	53.19	-104.36
N-9	0.32	1.22	12.11

TABLE B-9

Damaged Mode Shape Data from Simulated Refined-Sensor, Cross-Power Spectra
Damage Case A-8

Location	Mode 1: 3.79 Hz	Mode 2: 3.87 Hz	Mode 3: 5.09 Hz
N-1	0.33	1.21	-11.07
N-2	12.76	46.79	103.68
N-3	28.63	107.16	140.53
N-4	41.89	159.09	95.07
N-5	47.11	181.16	-0.31
N-6	42.26	164.74	-95.89
N-7	29.19	115.89	-141.65
N-8	13.18	53.77	-104.49
N-9	0.32	1.23	12.13

TABLE B-10

Damaged Mode Shape Data from Simulated Refined-Sensor, Cross-Power Spectra
Alternate Undamaged Case A-9

Location	Mode 1: 3.79 Hz	Mode 2: 3.87 Hz	Mode 3: 5.09 Hz
N-1	0.26	1.29	-7.49
N-2	5.72	44.50	69.39
N-3	17.50	109.69	94.01
N-4	30.33	171.03	63.36
N-5	38.24	202.40	-0.77
N-6	37.89	191.23	-64.93
N-7	29.21	140.90	-95.54
N-8	15.09	69.43	-70.36
N-9	0.28	1.32	8.27

Emin Aktan
University of Cincinnati
Infrastructure Institute
ML71
Cincinnati, OH 45221-0071

Sreenivas Alampalli
New York Dept. of Transportation
1220 Washington Ave.
Albany, NY 12232

David Albright
Alliance for Transportation Research
1001 University Blvd., SE Suite 103
Albuquerque, NM 87106

J. Altes
Institute of Safety Research & Reactor Tech.
Research Center Juelich
5170 Juelich
Postbox 1913, Germany

Alejandro Asfura
EQE, Inc.
44 Montgomery St., Suite 3200
San Francisco, CA 94104

Bill Baker
Los Alamos National Laboratory
ESA-EA, MS P946
P.O. Box 1663
Los Alamos, NM 87545

William Barringer
Alliance for Transportation Research
1001 University Blvd., SE Suite 103
Albuquerque, NM 87106

Jim Beavers
Martin Marietta Energy Systems, Inc.
P.O. Box Y
Oak Ridge, TN 37831

Mrinmay Biswas
Duke University
Dept. of Civil Engineering
Durham, NC 27706

Larry Blair
Los Alamos National Laboratory
DDET, MS D453
P.O. Box 1663
Los Alamos, NM 87545

Bob Burick
Granite Construction Co.
Heavy Construction Division
Box 50024
Watsonville, CA 95077-5024

Richard Burick
Los Alamos National Laboratory
DDESA, MS P945
P.O. Box 1663
Los Alamos, NM 87545

Steve Chase
Federal Highway Administration
6300 Georgetown Pike
McLean, VA 22101-2296

Franklin Cheng
University of Missouri Rolla
Dept. of Civil Eng.
Rolla, MO 65401

Ken Chong
National Science Foundation
4201 Wilson Blvd., Rm. 545
Arlington, VA 22230

Lowell Cogburn
Assocation of American Railroads
P.O. Box 11130
Pueblo, CO 81001

Tim Darling
Los Alamos National Laboratory
MST-10, MS K764
P.O. Box 1663
Los Alamos, NM 87545

Barry Davidson
Compusoft Engineering Ltd.
PO Box 9493
Newmarket, Auckland
New Zealand

Thomas Duffey
P.O. Box 1239
Tijeras, NM 87059

Dave Ewins
Imperial College
Mechanical Engineering Dept.
Exhibition Road
London SW7 2BX, UK

Richard Fale
W. S. Atkins
160 Aztec West
Park Avenue
Almondsburg
Bristol U.K. BS124TG

M. Ferner
Anlauf Ingenicur - Consulting GMBH
Posttach 101259
D-69002 Heidelberg, Germany

Chris Gannon
Penguin Engineering Ltd
PO Box 33 093
Petone, New Zealand

F. Gantenbein
C.E.A.-CE/Saclay - DMT/SEMT/EMS
91191 - GIF - SUR - YVETTE Cedex
France

Ephrahim Garcia
Vanderbilt University
Dept. of Mechanical Engineering
Box 1592, Station B
Nashville, TN 37235

Michael Grygier
NASA Johnson Space Center
ES43
Houston, TX 77058

Nicholas Haritos
Dept. of Civil and Environment Eng.
University of Melbourne
Parkville, Victoria 3052
Australia

Phil Hashimoto
EQE Engineering, Inc.
Lakeshore Towers
18101 Von Karman Ave., Suite 400
Ivine, CA 92715

Francois Hemez
Ecole Centrale Paris
LMSSMAT - Grande Voie Des Vignes
92295 Chatenay-Malabry

George James
Sandia National Laboratories
MS 0557
Albuquerque, NM 87185

Jim Johnson
EQE, Inc.
44 Montgomery St., Suite 3200
San Francisco, CA 94104

Tom Kashanganki
University of Maryland
SMART Materials and Structures Res. Center
College Park, MD 20742

Robert Kennedy
18971 Villa Terrace
Yorba Linda, CA 92686

Klaus Kerkhoff
Staatliche Materialprufungsanstalt
Universitat Stuttgart
D-70569 Stuttgart (Vailhingen)
Germany

Magdi Khalifa
University of Nebraska Lincoln
Civil Engineering Department
W348 Nebraska Hall
Lincoln, NE 68588-0531

Hyoung-Man Kim
McDonnell Douglas Aerospace
M/S: MDC-2-3353
13100 Space Center Blvd
Houston, TX 77059

Anne Kiremidjian
Stanford University
Department of Engineering
Terman Engineering Center 238
Stanford, CA 94305-4020

Richard Kohoutek
University of Wollongong
Dept. of Civil and Mining Engineering
Northfields Avenue
Wollongong 2522 Australia

John Kosmatka
University of California
Department of AMES
San Diego, CA 92093-0085

Christian Kot
Argonne National Laboratory
9700 South Cass Ave. RE/331
Argonne, IL 60439-4817

Michael Kuhn
Institute of National Surveying and Engineering Geodesy
University of Technology
Guszhausstr .27-29 (E1272)
A-1040 Vienna, Austria

Brett Lewis
APTEK, Inc.
1257 Lake Plaza Dr.
Colorado Springs, CO 80906

Shih-Chi Liu
National Science Foundation
4201 Wilson Blvd.
Arlington, VA 22230

Dave Martinez
Sandia National Laboratories
P.O. Box 5800
Albuquerque, NM 87185

Sami Masri
University of Southern California
Department of Civil Engineering
MC 2531
Los Angeles, CA 90089-2531

Randy Mayes
Sandia National Laboratories
MS0557
PO Box 5800
Albuquerque, NM 87185

Al Migliori
Los Alamos National Laboratory
MST-10, MS K764
P.O. Box 1663
Los Alamos, NM 87545

Jack Moehle
University of California
Department of Civil Engineering
775 Davis Hall
Berkeley, CA 94720

Denby Morrison
Shell E&P Technology Company
Ocean R&D, Bellarie Technology Center
P.O. Box 481
Houston, TX 77001

Peter Moss
University of Canterbury
Department of Civil Engineering
Private Bag 4800
Christchurch, New Zealand

Robert Murray
Lawrence Livermore National Laboratory
P.O. Box 808, L-197
Livermore, CA 94550

Roberto Osegueda
The University of Texas at El Paso
Department of Civil Engineering
El Paso, TX 79912

Gerard Pardoen
University of California-Irvine
101 ICEF-Civil Eng.
Irvine, CA 92717

Lee Peterson
Center for Aerospace Structures
University of Colorado, Boulder
Campus Box 429
Boulder, CO 80309-0429

Ron Polivka
EQE, Inc.
44 Montgomery St., Suite 3200
San Francisco, CA 94104

Don Rabern
Los Alamos National Laboratory
ESA-EA, MS P946
P.O. Box 1663
Los Alamos, NM 87545

John Reed
Jack Benjamin & Associates
Mountain Bay Plaza
444 Castro St. Suite 501
Mountain View, CA 94041

Mark Richardson
Vibrant Technology, Inc.
18141 Main Street
Jamestown, CA 95327

Jim Ricles
Lehigh University
Department of Civil Engineering
117 ATLSS Drive, H Building
Bethlehem, PA 18015-4729

John Ruminer
Los Alamos National Laboratory
DDESA, MS P945
P.O. Box 1663
Los Alamos, NM 87545

M. Saiidi
College of Engineering
Department of Civil Eng./258
Reno, NV 89557-0152

Mike Salmon
EQE Engineering, Inc.
Lakeshore Towers
18101 Von Karman Ave., Suite 400
Ivine, CA 92715

Masoud Sanayei
Tufts University
Dept. of Civil and Env. Engineering
Lexington, MA 02173

Jim Sirkis
University of Maryland
SMART Materials and Structures Res. Center
College Park, MD 20742

Paul Smith
Los Alamos National Laboratory
ESA-MT, MS C931
P.O. Box 1663
Los Alamos, NM 87545

Christopher Smith
FAA Technical Center
Altantic City Int'l Airport, NJ 08405

Suzanne Smith
University of Kentucky
Department of Engineering Mechanics
467 Anderson Hall
Lexington, KY 40506-0046

Cecily Sobey
Earthquake Engineering Research
Center Library
Gift & Exchange Dept.
University of California/RFS 453
1306 Souh 46th Street
Richmond, CA 94804-4698

Mete Sozen
2113 Newmark Civil Engineering Lab.
208 North Romine Street
Urbana, IL 61801

John Stevenson
Stevenson & Associates
9217 Midwest Avenue
Cleveland, OH 44125

Norris Stubbs
Texas A&M University
Department of Civil Engineering
Mechanics & Materials Center
College Station, TX 77843-3136

Arisi Swamidas
Memorial University of Newfoundland
St. Johns
Facility of Engineering
Newfoundland, Canada, A1B 3X5

Geof. Tomlinson
The University of Sheffield
Department of Mechanical and Process
Engineering
PO Box 600
Mappin St
Sheffield S1 4DU

Ward Turner
Exxon Production Research Company
P.O. Box 2189
Houston, TX 77252

Ming Wang
University of New Mexico
Department of Civil Engineering
209 Tapy Hall
Albuquerque, NM 87131

Lloyd Welker, Jr.
Ohio Department of Transportation
25 South Front Street
Columbus, OH 43216-0899

Robert West, Jr.
Virginia Polytechnic Institute of State Univ.
Structural Imaging and Modal Analysis Lab.
Mechanical Engineering Department
Blacksburg, VA 24061-0238

Ed White
McDonnell Douglas Aerospace
Mailcode 1021310
P.O. Box 516
St. Louis, MO 63166

Ken White
Dept. of Civil, Agricultural, and Geological Eng.
Box 30001/Dept. 3CE
Las Cruces, NM 88003-0001

P. Winney
P&P Engineering
Consultant Engineers
P.O.Box 36
Billingshurst, West Sussex RH14 OYG

Bill Young
W. P. Young Construction, Inc.
426 Lincoln Centre Drive
Foster City, CA 94404-1127

Dave Zimmerman
University of Houston
Department of Mechanical Engineering
Houston, TX 77204-4792

This report has been reproduced directly from the
best available copy.

It is available to DOE and DOE contractors from
the Office of Scientific and Technical Information,
P.O. Box 62,
Oak Ridge, TN 37831.
Prices are available from
(615) 576-8401.

It is available to the public from the
National Technical Information Service,
US Department of Commerce,
5285 Port Royal Rd.
Springfield, VA 22616.

LOS ALAMOS
NATIONAL LABORATORY

APR 19 1996

LIBRARIES
PROPERTY

Los Alamos
NATIONAL LABORATORY
Los Alamos, New Mexico 87545